Carranza-Torres, C., D. Fosnacht, and G. J. Hudak (2016). Analytical and numerical study of the stability of shallow underground openings for mining and compressed air energy storage applications. In P. G. Ranjith and J. Zhao (Eds.), *Keynote Lecture. Proceedings of the IC3G International Conference on Geomechanics, Geoenergy and Georesources. September 28-29, 2016*. Monash University. Melbourne. Australia. Available for downloading at www.d.umn.edu/∼carranza/IC3G.

Analytical and numerical study of the stability of shallow underground openings for mining and compressed air energy storage applications

C. Carranza-Torres[a*], D. Fosnacht[b], and G.J. Hudak[b]

[a]*Department of Civil Engineering, University of Minnesota Duluth, Minnesota, USA*
[b]*Natural Resources Research Institute, University of Minnesota Duluth, Minnesota, USA*

[*]*carranza@d.umn.edu (corresponding author's E-mail)*

Abstract

This paper presents a study of mechanical stability of shallow circular cavities carried out as part of a multidisciplinary project that investigated the possibility of using existing underground mining works (drifts and shafts) from iron mining works dating back from the first half of the 20th century in northern Minnesota (USA), for Compressed Air Energy Storage (or CAES) applications. CAES systems compress air into an underground cavity when there is an excess of energy production (e.g., in the electrical grid or in an electrical plant) and generate electrical energy using a turbine when the electricity demand exceeds the production. This paper addresses the fundamental problem of establishing the stability conditions of shallow cylindrical or spherical openings excavated in cohesive ground, and subjected to either decreasing or increasing internal pressure, associated with the process of contraction or expansion of the cavities during operation of a CAES system. A statically admissible analytical model for a shallow circular opening in cohesive ground derived from the limit analysis lower bound theorem is presented, and key dimensionless groups of variables controlling the stability of the cavity, defined in terms of a scalar factor of safety, are identified. The analytical model allows several observations of practical interest to be made with regard to the stability of shallow cavities. Numerical finite-difference (FLAC) models are used to validate the various observations and to quantify the underestimation of factors of safety obtained with the proposed lower bound solution. The paper also presents a critical evaluation of limit equilibrium (Terzaghi's type) models that are traditionally used to design cavities for gas and air storage. Comparisons of results obtained with existing limit equilibrium models, with the proposed analytical model and with numerical models, show that limit equilibrium models can lead to both over conservative (i.e., too safe or uneconomical) and to nonconservative (i.e., unsafe) cavity designs depending on ranges considered for the dimensionless groups of variables governing the problem. The effect of other loading and ground conditions, such as frictional strength for the ground, distribution of internal pressure in the cavity, and different ratios of horizontal-to-vertical *in-situ* stresses, on stability of the cavities are also discussed.

Keywords: *CAES, shallow cavities, stability, factor of safety, limit analysis, limit equilibrium*

1. Introduction

A Compressed Air Energy Storage (CAES) plant compresses air when there is an excess of electrical energy production in the grid and generates electrical energy using a turbine when the demand exceeds the production. The storage of compressed air to produce energy in this way is typically done in underground cavities created for this specific purpose (e.g., in salt formations, new cavities can be relatively easily created by dissolution methods), or in reconditioned existing cavities (e.g., mining rooms, drifts and shafts).

Figure 1 (after Succar & Williams 2008) shows a schematic configuration of a *compensated* or constant pressure storage CAES system. The main components of the system are the underground storage cavity, the compressors and turbines (located in the CAES plant) and the surface water reservoir that in combination with a shaft allows maintenance of a constant storage pressure both during compression or decompression of the air in the underground cavity. Another possible configuration for a CAES system is that of a *non-compensated* or variable pressure storage option, in which no reservoir (nor water shaft) exists and the pressure inside the cavern decreases as air is extracted to produce energy. The compensated CAES system is more efficient (i.e., it produces more energy for the same initial storage pressure and volume) but it is less flexible than the non-compensated one, since it requires availability of a water reservoir, construction of a water shaft, and location of the storage cavern at enough depth to achieve the design storage pressure (Succar & Williams 2008).

The storage volume and pressure of the air in the underground chamber depends mainly on the target energy to be generated by turbines (i.e., the power to be sustained for a design number of hours), the type of scheme (whether compensated or non-compensated) and the efficiency and characteristics of the turbines (Zaugg 1975; Cavallo 2007). Figure 2, adapted from Succar & Williams (2008), presents a diagram showing the theoretical relationship between the mentioned variables. The horizontal axis represents the storage pressure of the air in a compensated system or the initial pressure of the air in a non-compensated system. The vertical axis represents

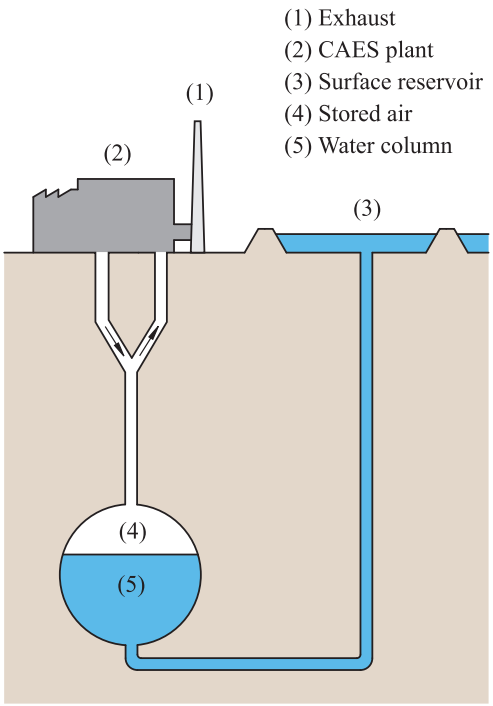

Figure 1. Constant pressure CAES storage with surface reservoir and compensating water column (after Succar & Williams 2008).

the ratio of the energy to be generated and the volume of the storage chamber. The different curves correspond to various configurations of CAES systems: the uppermost curve corresponds to a compensated (constant pressure) CAES system, while the different curves below correspond to non-compensated (variable pressure) CAES systems, for different ratios of initial to final storage pressure, and two cases of turbine operations. The diagram shows that a constant pressure system is more efficient than any variable pressure one, since it yields the largest amount of energy for any given value of air storage pressure. A case example illustrating use of the diagram to determine the storage volume of air for a non-compensated system has been added in the lower part of Figure 2.

Considering the costs of developing a CAES system which include construction of underground caverns, drifts and shafts, Cavallo (2007) and Denholm & Sioshansi (2009) mention powers in the range of 100 to 200 MW to be sustained for at least 10 hours, and (initial) storage pressures within the range of 80 bar (8 MPa) as convenient targets to consider. Succar & Williams (2008) describe the characteristics of two existing (functional) CAES plants, the McIntosh power plant in McIntosh, Alabama (USA) and the Huntorf power plant, near Bremen, Germany. As a reference, the McIntosh power plant in McIntosh, Alabama, has been operating since 1991 and is reported to produce 110 MW of electricity. The plant is capable of sustaining that power for 26 hours by storing air in a single chamber of 560,000 m^3 (the chamber was excavated in a salt formation by the dissolution method, and it does not have lining). The working pressure of the air stored in the chamber varies from 74 to 45 bar (or 7.4 to 4.5 MPa, respectively).

In addition to the 'large-scale' CAES systems mentioned above, 'small-scale' CAES systems can be considered convenient alternatives for a storage of energy associated with small wind farms, particularly when shallow underground cavities (e.g., from old mining activities) exist already at the site. In such cases energy powers below 10 MW sustained for 3 hours or less, with (initial) storage pressures below 70 bar (7 MPa) could be convenient targets to consider (Fosnacht et al. 2015).

For more than one hundred years, the state of Minnesota in the northern USA has been a leading producer of iron in the country. In the northern part of Minnesota there exists various iron formations of Precambrian age, including the Paleoproterozoic Gunflint, Mesabi and Cuyuna Iron Ranges, and the Neoarchean Vermilion Iron Range (Marsden 1968; Peterson et al. 2001; Addison et al. 2005; Lodge et al. 2013).

Although at present time only surface mining in the form of shallow taconite open pits takes place, there exists extensive traces of old underground mining works in the form of relatively shallow shafts and drifts that date back to the first half of the 20th century (Peele 1945; Lamppa 2004; MNDNR-LAM 2011).

Various studies have been conducted to evaluate taking advantage of existing surface and underground mining

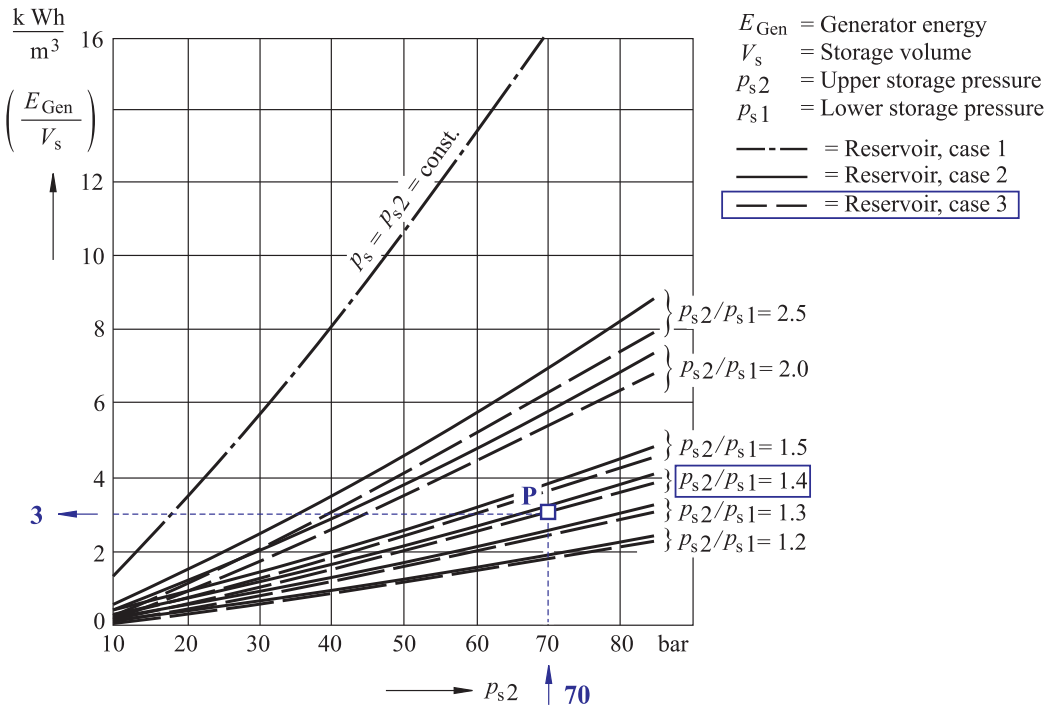

Example:
A proposed CAES plant will generate 100 MW operating for 5 hours (i.e., produced energy will be E_{Gen} = 500,000 kWh). Constant turbine inlet pressure will be used (Case 3); maximum pressure p_s2 will be 70 bar (7 MPa); minimum pressure p_s1 will be 50 bar (5 MPa), i.e., p_s2/p_s1= 1.4. From the diagram, E_{Gen}/V_s= 3 (see Point P). Therefore the required storage volume results to be $V_s = E_{Gen}$ / 3 = 166,667 m³.

Figure 2. Relationship between generated energy, storage volume, upper and lower storage pressure and operation cases —adapted from Succar & Williams (2008). The framed inset below shows an example of computation of air storage volume required to produce a given amount of energy for a given air storage pressure in a variable pressure storage CAES system.

excavations in northern Minnesota for energy generation (see, for example, Leoni 1985; Fosnacht & PHES Study Team 2011; Bauer et al. 2012; Fosnacht et al. 2015). In particular, Fosnacht et al. (2015) studied the economical and technical aspects of constructing CAES plants using existing underground mine workings and above ground features at various locations in Minnesota, for both large scale and small scale CAES systems. Figure 3a shows the three locations for potential CAES plants considered in this study. Figure 3b shows isometric views of existing shallow underground shafts and drifts at one of the locations, which were considered for air storage for a small scale CAES development associated with wind turbines.

The engineering design of underground cavities for air and gas storage has been treated by numerous authors (see, for example, Kovári 1993; Damjanac et al. 2002; Blindheim et al. 2004). Major engineering considerations associated with the design of underground caverns for air and gas storage include ensuring tightness through installation of an impermeable liner or installation of water curtains, and ensuring the stability of the cavern at different stages of the operations, for example, when no air or gas is present, and when the air or gas is stored at the maximum design pressure (Goodall et al. 1988; Kovári 1993; Shidahara et al. 1993; Liang & Lindblom 1994).

This paper presents a study of fundamental aspects of the stability conditions of shallow openings of simple shape (cylindrical tunnels or spherical cavities) done as part of the multidisciplinary study by Fosnacht et al. (2015) that looked into the possibility of using underground mine workings for development of a CAES plant in Minnesota. The focus of the study reported in this paper is on assessing the mechanical stability of relatively shallow openings such as those represented in Figure 3b when the tightness of the air has been guaranteed by application of a thin impermeable liner that has no structural support effect. The study considers both, the stability conditions of a 'contracting' (cylindrical or spherical) cavity when emptying of air takes place and *caving-type* collapse of the ground above the cavity is to be prevented; and the stability conditions of an

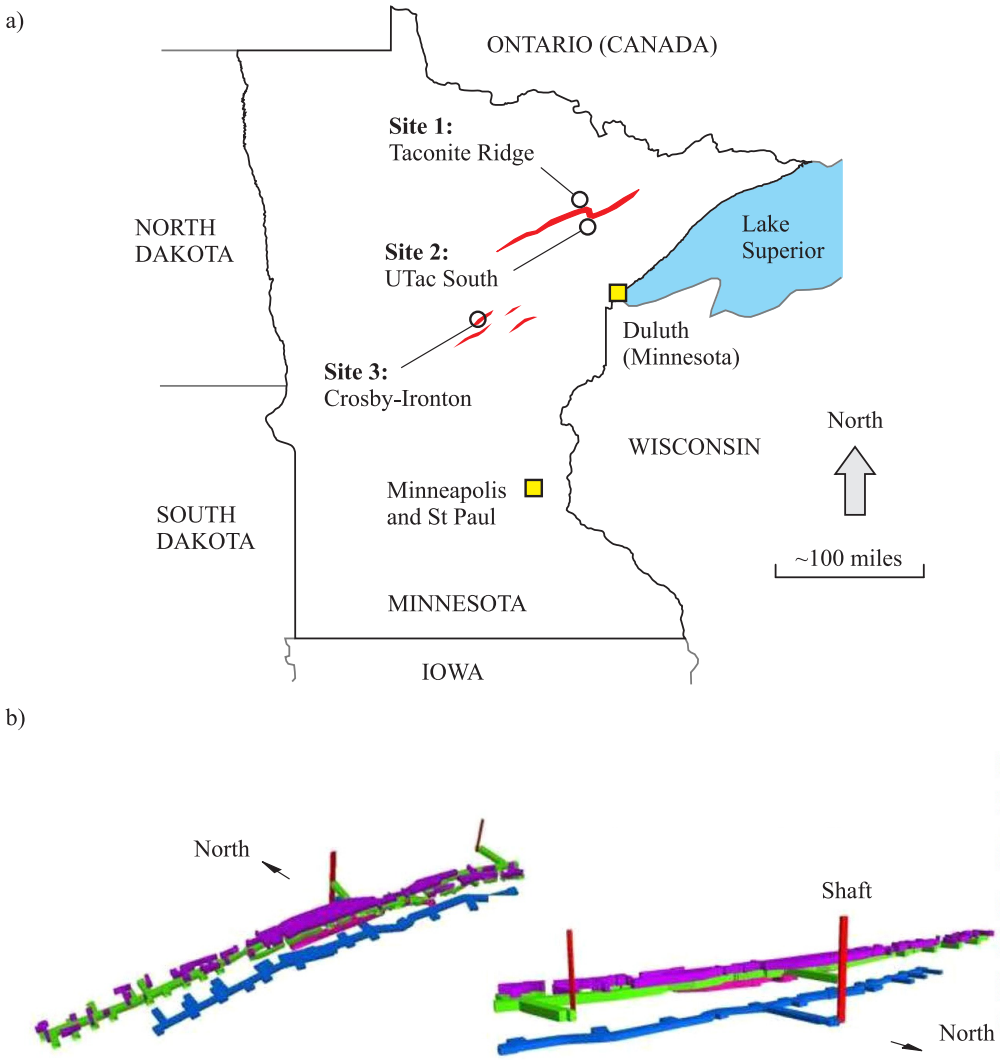

Figure 3. a) Map of the state of Minnesota (USA) showing three potential locations selected for emplacement of CAES systems. b) Isometric views of old underground mining works at Site 3: Crosby-Ironton. Existing shafts and drifts at the location considered for potential air storage —after Fosnacht et al. (2015).

'expanding' (cylindrical or spherical) cavity when pumping of air takes place and *uplift-type* of failure of the ground above the cavity is to be prevented.

It must be emphasized that the problem of assessing the stability conditions of *contracting* cavities is not relevant to design of CAES systems in particular, but it is also quite relevant in the assessment of stability conditions of shallow tunnels for civil engineering applications, such as the case of shallow tunnels for transportation projects. For example, Figure 4a shows a bus that fell into a sinkhole formed by the collapse of a tunnel front during construction of the Munich Metro in 1994 (Construction Today 1994a; 1994b). Figure 4b shows another collapse that occurred due to failure of tunnel support below Hollywood Boulevard in Los Angeles, during construction of the metro in 1995 (Civil Engineer International 1995; Oliver 1995). Figure 4c shows another collapse that occurred during construction of the underground Mass Rapid System in Singapore in 2005 (Government of Singapore 2005). Mechanical stability models of the type to be addressed in this paper could serve the purpose of addressing collapse problems such as those shown in Figure 4.

The following section presents a brief literature review on existing methods for analysis of underground shallow cavities.

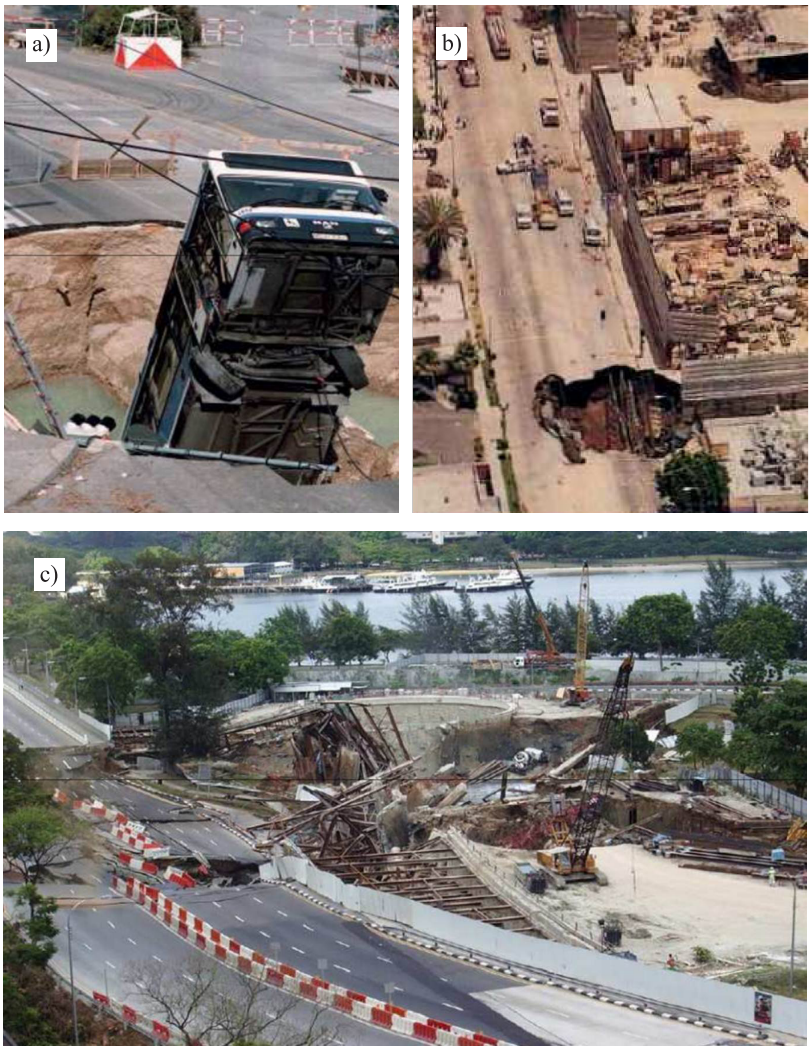

Figure 4. a) Collapse during construction of the Munich Metro (after Construction Today 1994a; 1994b). b) Collapse during construction of the LA Metro (after Civil Engineer International 1995; Oliver 1995). c) Collapse during construction of the Singapore underground Mass Rapid Transit (MRT) system (after Government of Singapore 2005).

2. Methods of analysis of stability of underground openings

Table 1, after Potts & Zdravkovic (1999), lists different methods used in the analysis of geotechnical problems involving soil and rock, such as assessment of stability conditions of slopes and tunnels. The different rows in the table correspond to the different methods, sorted in ascending order of *flexibility* while the different columns describe the governing conditions (equilibrium, compatibility of deformations, material constitutive model, and boundary condition equations) that the various methods satisfy (or do not satisfy).

Four of the methods listed in Table 1 are relevant to this study and are briefly described below.

These are: i) limit equilibrium solutions; ii) stress field solutions; iii) limit analysis solutions (including lower bound and upper bound solutions); and iv) full numerical solutions. For a more detailed treatment of these methods, particularly as applied to design of tunnels, the reader is referred to Kolymbas (2005).

Limit equilibrium solutions (second row in Table 1) consider equilibrium of a mass of soil (or rock) that, as the name of the method indicates, is in a limit state of equilibrium and therefore tends to detach and produce the collapse of the structure. A classical limit equilibrium model for shallow tunnels is that presented by Terzaghi (Terzaghi 1943; Proctor & White 1977) and is represented in Figure 5. The model in Figure 5, developed in the context of studying arching effects in soils, allows determination of the support pressure on the roof of a shallow rectangular tunnel (of width and height, B_o and H, respectively; and depth D) that is required to maintain stability of the overlying rectangular mass of soil of assumed dimensions (width and height, $2B_1$ and D, respectively). In limit equilibrium models such as the one represented in Figure 5, the shear strength of the ground is assumed to be fully mobilized on the lateral boundaries of the block (in this case the left and right boundaries of length D) that tends to detach. Limit equilibrium models based on Terzaghi's model have also been proposed for assessing the stability of tunnel fronts —i.e., the vertical plane that remains unsupported as a tunnel is advanced and support is installed behind it. Figure 6a shows such a limit equilibrium model for the front of an unsupported tunnel as proposed by Horn (1961). Figure 6b shows another model due to Tamez et al. (1997), as reported by Cornejo (1989) (see also Tanzini 2001), which accounted for tunnel support behind the face. Terzaghi's type limit equilibrium models have been also proposed to analyze the stability of shallow caverns for gas storage. For example, Figure 7 (after Sofregaz U.S. Inc. 1999) shows a similar limit equilibrium model for determining the maximum stored gas pressure, P, of a section of horse-shoe shaped cavern (of width and height, D and H, respectively) located at a shallow depth (Z). Note that the limit equilibrium of a wedge of soil or rock with inclined walls (at angles, α, with respect to the vertical) is considered in this model. Both models represented in Figures 5 and 7, for the case of *contracting* and *expanding* openings, respectively, are discussed further in Section 5 and are shown to overestimate or underestimate the stability conditions of shallow openings depending on the values considered for the input variables.

Stress field solutions (third row in Table 1) for shallow cavities are obtained by integrating equilibrium equations in a region of specified shape surrounding the cavities, assuming that the stresses are compatible with a plastic state (i.e., in a stress field model the ground in a region surrounding the cavity satisfies equilibrium and is assumed to be in plastic state). A stress field solution disregards the state of the material (whether in elastic or plastic state) in the region outside the integration region. Caquot's solution (after Caquot 1934) is a stress field solution that allows determination of the support pressure required to maintain equilibrium of a shallow circular opening (a section of long cylindrical tunnel or a spherical cavity) located at a shallow depth with respect to the ground (see Figure 8a). Caquot's type models for determining stability of shallow tunnels have been investigated extensively by French researchers (Mandel et al. 1974; d'Escatha & Mandel 1971; d'Escatha & Mandel 1974) (see Figure 8b). Caquot's model is taken as a basis for developing the analytical model in this study, presented later on in Section 3.

Limit analysis solutions (fourth and fifth rows in Table 1), are based on two theorems of the theory of plasticity, namely the lower bound and upper bound theorems (see, for example, Davis & Selvadurai 2002; Pietruszczak 2010).

The lower bound theorem states that a lower bound (or statically admissible) solution that satisfies static equilibrium everywhere in the material and nowhere violates the yield condition of the material leads to a safe estimate of the stability conditions for the problem. In the context of analyzing the required internal support pressure to maintain equilibrium of a shallow circular opening, as considered by Caquot (1934), the statically admissible (or lower bound) solution predicts a support pressure that is higher than the true support pressure required for equilibrium (i.e., it leads to a conservative or *safe* design).

The upper bound theorem states that an upper bound (or kinematically admissible) solution for which discrete movement of material is already taking place, leads to an unsafe estimate of the stability conditions for the

Table 1. Methods to analyze stability of structures such as slopes and tunnels in soils and rocks —after Potts & Zdravkovic (1999).

METHOD OF ANALYSIS		SOLUTION REQUIREMENTS				
		Equilibrium	Compatibility	Constitutive behaviour	Boundary conditions	
					Force	Disp
Closed form		S	S	Linear elastic	S	S
Limit equilibrium		S	NS	Rigid with a failure criterion	S	NS
Stress field		S	NS	Rigid with a failure criterion	S	NS
Limit analysis	Lower bound	S	NS	Ideal plasticity with associated flow rule	S	NS
	Upper bound	NS	S		NS	S
Beam-Spring approaches		S	S	Soil modelled by springs or elastic interaction factors	S	S
Full Numerical analysis		S	S	Any	S	S

S - Satisfied; NS - Not Satisfied

problem. In the context of analyzing the required internal support pressure to maintain equilibrium of a shallow circular opening mentioned above, the kinematical admissible (or upper bound) solution predicts a support pressure that is lower than the true support pressure required for equilibrium (i.e., it leads to a non-conservative or *unsafe* design).

Various authors have developed limit analysis solutions to assess the stability of circular sections of shallow tunnels or the unsupported span of a circular tunnel in the vicinity of the tunnel front. For example, Davis et al. (1980) presented both statically and kinematically admissible solutions for circular shallow tunnels in cohesive soils (see Figure 9a). Atkinson & Potts (1977) presented a similar analysis for cohesionless and frictional soil. Mühlhaus (1985) presented lower bound solutions for circular shallow tunnels in cohesive and frictional ground (see Figure 9b).

In the context of analyzing stability of *contracting* and *expanding* cavities for CAES applications, statically admissible (or lower bound) solutions are attractive because of the *safe* nature of predicted stability conditions. As mentioned earlier on, Section 3 presents an extended form of the stress field Caquot's model, that among others, introduces a scalar factor of safety, as typically done in solutions for stability analysis of slopes. In Section 3 it is shown that the extended (Caquot's) stress field model is actually a statically admissible model when the ratio of *in-situ* (or far-field) horizontal and vertical stresses is equal to one. Therefore, the analytical model developed in this study is shown to lead to safe estimates of the stability conditions for shallow cavities of circular shape.

Full numerical methods (last row in Table 1) are by far the most versatile available methods for solution of geotechnical problems. Finite element, finite difference, discrete element and other numerical methods fall into this category (see, for example, Brady & Brown 2004). These numerical methods require discretization (i.e., partition with elements) of the domain of the problem. These methods yield only approximate solutions of the unknown variables (for example, stress and displacement fields) and the quality of the approximation depends mainly on the resolution of the mesh used to discretize the domain.

With regard to determining the stability conditions of geotechnical problems, such as determining the required support pressure of shallow tunnels using numerical methods, two approaches have been used.

The first approach involves programming the equations of the lower bound and upper bound theorems of plas-

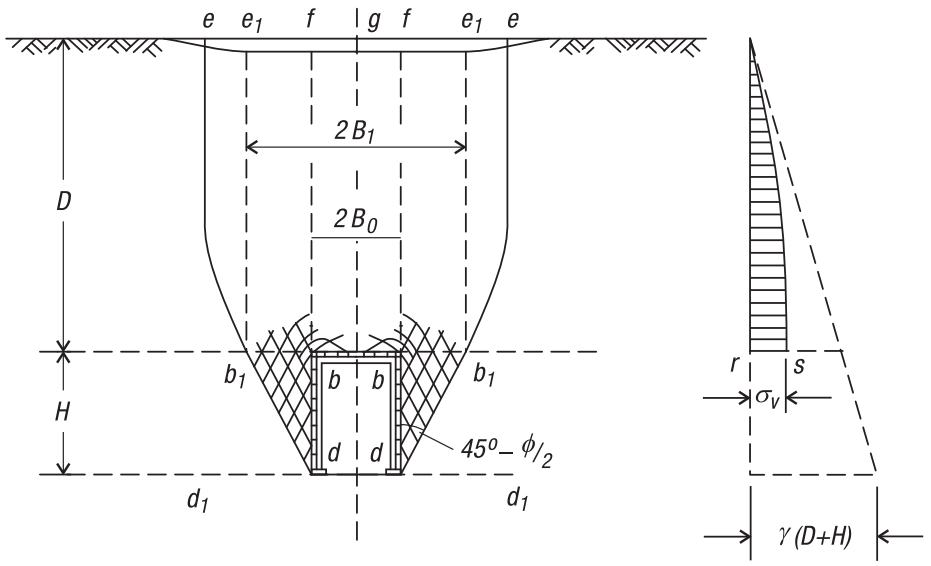

Figure 5. Limit equilibrium model by Terzaghi (1943) to determine the required support pressure at the roof of a shallow tunnel.

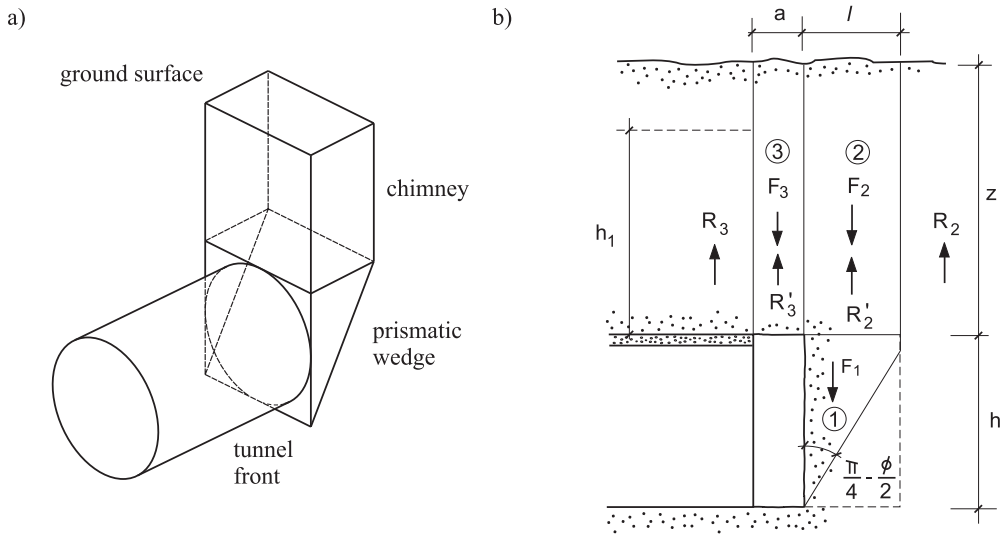

Figure 6. Limit equilibrium models for analyzing the stability of tunnel fronts for a) unsupported tunnel (after Horn 1961); and b) supported tunnel (as reported in Cornejo 1989 —see also Tanzini 2001).

ticity described above and seeking statical or kinematical admissible solutions for the problems in question (Lyamin & Sloan 2002a and Lyamin & Sloan 2002b have presented an approach of this type).

The second approach involves intensive computing and consists in solving the problem repeatedly (for example, in the case of a shallow cavity, for decreasing values of support pressure) until the instability occurs (i.e., until the numerical solution does not converge because it is not possible to find the state of equilibrium for which the material constitutive law is satisfied in all elements of the domain).

Figures 10a and 10b, after Fairhurst & Carranza-Torres (2002), illustrate the second approach. Figure 10a shows the mesh of elements in the numerical model of a (plane strain) section of a shallow circular tunnel solved with the software FLAC (Itasca 2008); the vertical axis in the diagram in Figure 10b, represents the decreasing values of internal pressure considered in the model of Figure 10a (the *inverted* triangle symbols represent the models that resulted stable; while the *regular* triangle symbols represent the models that resulted unstable). Figure 11 shows views of the sequence of FLAC models corresponding to the four lowermost triangle symbols in Figure 10b. Fairhurst & Carranza-Torres (2002) compared results obtained with the finite-difference code FLAC with those obtained with Terzaghi's type limit equilibrium and Caquot's type solutions and quantified

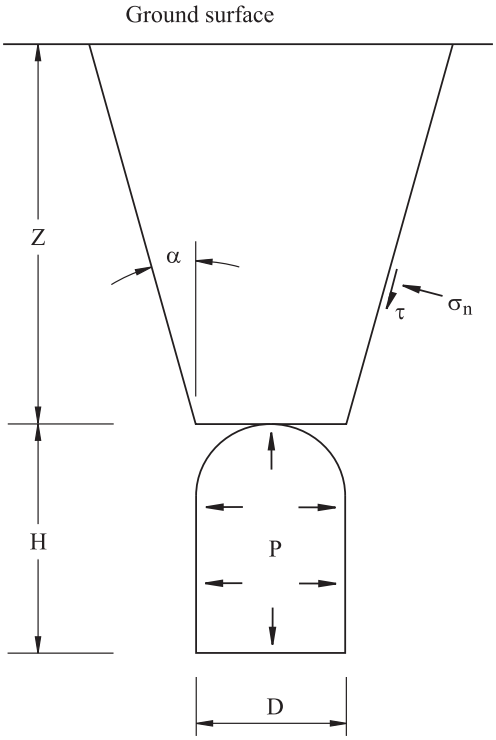

Figure 7. Limit equilibrium (Terzaghi's type) model to determine the maximum gas pressure in an underground gas storage cavern —after Sofregaz U.S. Inc. (1999).

the overestimation of required support pressure predicted by the analytical methods. The authors found that Terzaghi's results were significantly over conservative (see Figure 12).

In the last decade or so, the increase of computer power allowed developers of commercial finite element and finite difference software to implement what it is referred to as the *strength reduction technique* to determine *factors of safety* of shallow excavations in soil and rock, typically slopes (Itasca 2008; Plaxis b.v. 2012; Rocscience 2014). The *strength reduction technique* for analysis of slopes involves solving the problem repeatedly (i.e., applying the second of the two methods discussed above) for decreasing values (if the problem is stable for the given ground properties) of shear strength properties of the material, until the instability occurs (i.e., until the numerical solution does not converge anymore). Then the factor of safety is determined as the ratio of given shear strength parameters and the reduced shear strength parameters for which the model does not converge (see Figure 13). Although the *strength reduction technique* is nowadays a common method for solving slope problems (Dawnson et al. 1999; Hammah et al. 2007a; Hammah et al. 2007b), the technique is not necessarily restricted to slopes and can also be applied to assess the stability of shallow underground cavities. Indeed, the documentation of the software RS2 (Rocscience 2014) presents a comparison of factors of safety for a shallow circular tunnel obtained with the software and with the Davis et al. (1980) lower and upper bound solutions mentioned above. In Section 4, the *strength reduction technique* implemented in the software FLAC (Itasca 2008) is used to obtain results of factors of safety for shallow circular tunnels and to compare and quantify differences of these results with those obtained with the statically admissible solution developed in this study.
The following sections present the analytical model used to establish stability conditions of shallow circular *contracting* or *expanding* openings (sections of long cylindrical tunnels or spherical cavities) located at a shallow depth with respect to the ground. The model, which as mentioned earlier on is based on Caquot's stress field model, is an extension of a model originally developed for estimation of stability conditions of shallow tunnels with particular reference to mechanized tunnelling in soils (Carranza-Torres 2004; Guglielmetti et al. 2008). In order to simplify the formulation and to be able to reveal the fundamental relationships among variables that control the problem, Section 3 considers first the case of cavities in purely cohesive ground, as in the study by Davis et al. (1980). Thereafter, Section 6 considers the case of cavities in cohesive-frictional ground.

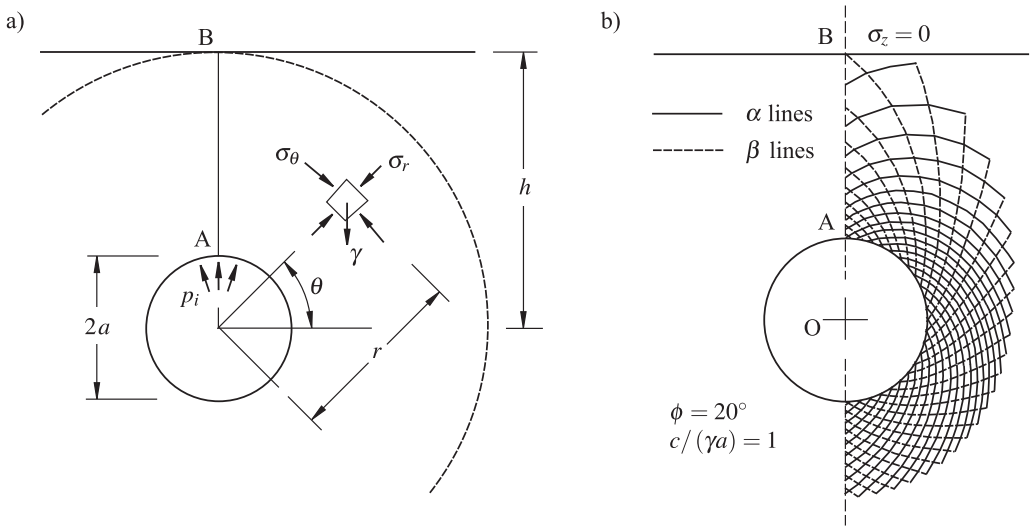

Figure 8. Stress field solutions proposed by a) Caquot (1934) and b) d'Escatha & Mandel (1971).

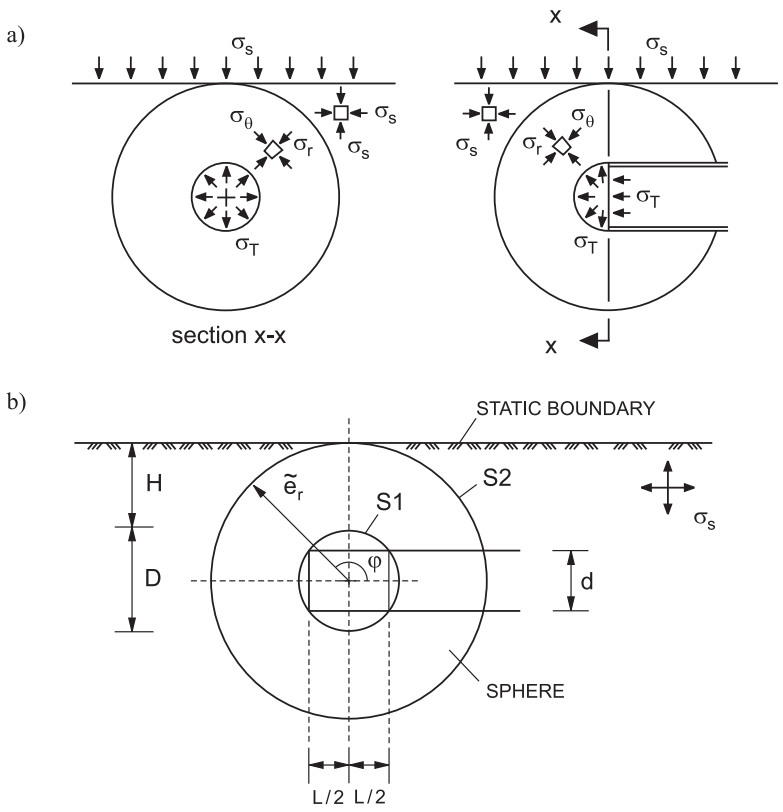

Figure 9. Statically admissible solutions for spherical cavities by a) Davis et al. (1980) and b) Mühlhaus (1985) used to analyze stability of the tunnel front and the unsupported region behind the tunnel front, respectively.

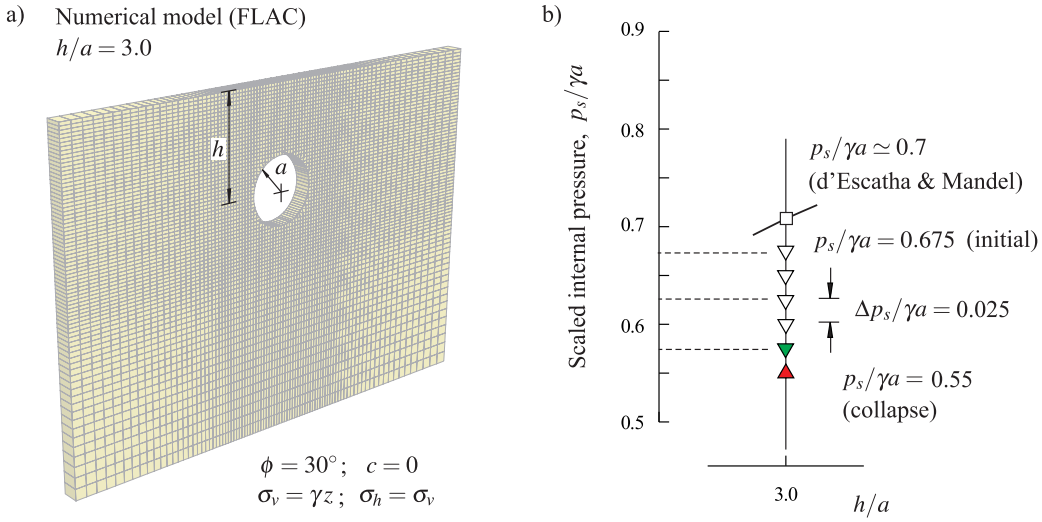

Figure 10. Computation of minimum internal pressure required for stability of a shallow tunnel using FLAC –after Fairhurst & Carranza-Torres (2002).

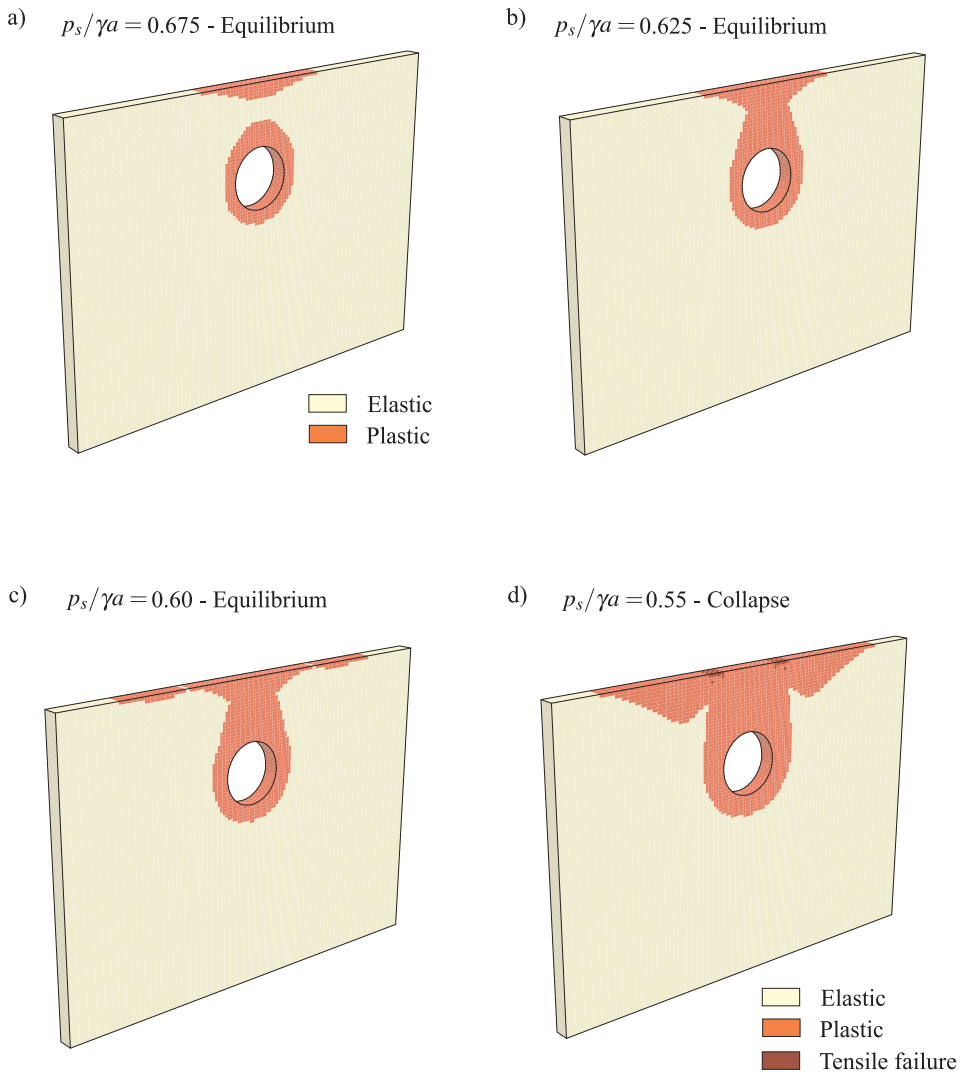

Figure 11. Sequence of internal pressure reduction in the FLAC model in Figure 10 –after Fairhurst & Carranza-Torres (2002).

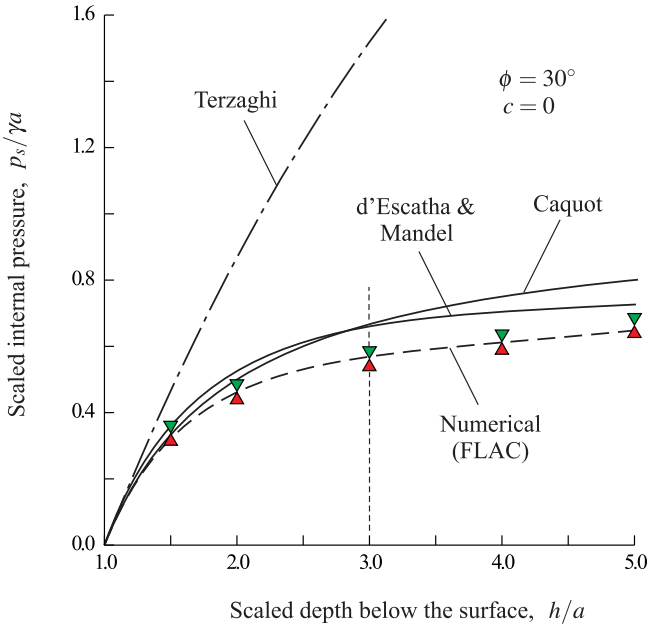

Figure 12. Comparison of required support pressure for shallow tunnels according to Terzaghi's solution, Caquot and d'Escatha & Mandel's solutions and the numerical FLAC solution –after Fairhurst & Carranza-Torres (2002).

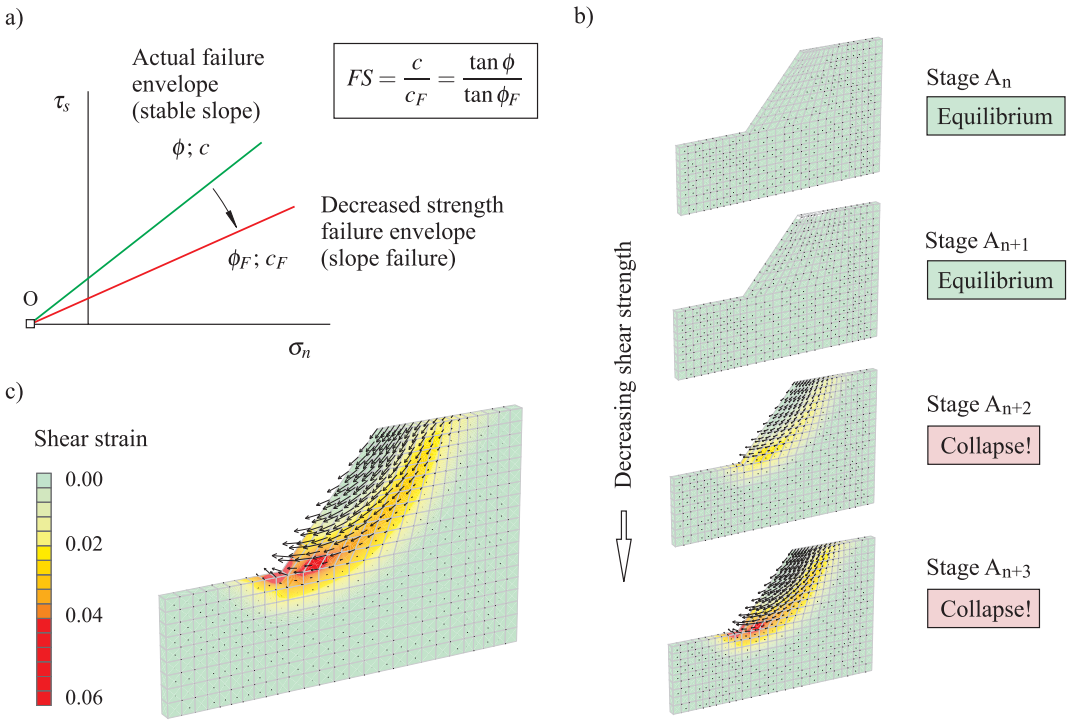

Figure 13. *Strength reduction technique* applied to the determination of factor of safety for a slope in Mohr-Coulomb material. a) Reduction of given cohesion and internal friction angle to obtain the critical cohesion and critical internal friction angle defining the factor of safety. b) Sequence of models with decreasing shear strength properties, showing the transition from stable to unstable conditions. c) Closeup of slope model showing collapse by development of a shear failure surface.

3. Analytical model for stability of contracting *and* expanding *shallow cavities*

3.1. Problem statement

The problem considered in this study is represented in Figure 14. A cylindrical or spherical cavity of radius, a, is excavated below the ground surface at shallow depth. A cartesian coordinate system, (x,y), is considered to have the origin at the center of the cavity (point O in Figure 14). The distance between the ground surface and the center of the cavity (i.e., the depth of the cavity) is denoted as h. A surcharge load, q_s, is considered to act on the ground surface.

In Figure 14, the points A, C and D are located at the *crown*, *spring line* and *invert* levels on the cavity periphery, respectively. Point B is the projection of point A on the ground surface. At the *crown* of the cavity (point A), the internal pressure is denoted as p_s^A (or simply as p_s); the distribution and values of internal pressure at points other than point A are discussed later on.

In Figure 14, the circle labelled as 'Integration circle' has its center at the center of the cavity (point O) and has a radius h. Associated to this circle, a polar (or spherical) coordinate system, (r,θ), with its origin at point O, is considered.

Inside the integration circle, the stresses are assumed to be redistributed due to excavation as indicated for the arbitrary point P of polar coordinates, (r,θ). Note that after excavation, radial stresses, σ_r, and tangential (or hoop) stresses, σ_θ, become principal stresses.

Outside the integration circle, vertical and horizontal stresses are assumed to be principal stresses, as indicated for the arbitrary point S of ordinate, y, in Figure 14. The initial (or *in-situ*) vertical stress, σ_y^o, is considered to be *lithostatic*, i.e.,

$$\sigma_y^o = q_s + \gamma(h-y) \tag{1}$$

and the initial (or *in-situ*) horizontal stress, σ_x^o, is obtained by multiplying the coefficient of earth pressure at rest, K_o, and the vertical stress, i.e.,

$$\sigma_x^o = K_o\,\sigma_y^o \tag{2}$$

In the analytical solution of the problem presented here, the normal stresses are assumed to be positive when in compression; consequently, all stress quantities represented in Figure 14 are positive and represent compression.

In the model in Figure 14, the ground is assumed to be dry and to have a unit weight, γ. As mentioned earlier on, with the purpose of simplifying the analysis and to be able to reveal fundamental aspects of stability of shallow cavities, the ground is assumed to be purely cohesive and to obey a Tresca shear failure criterion, which in terms of principal stresses, σ_1 and σ_3, is written as (see, for example, Jaeger et al. 2007)

$$\sigma_1 = \sigma_3 + \sigma_c \tag{3}$$

In equation (3), σ_c is the uniaxial compressive strength of the ground, which is related to the cohesion, c, of the ground as follows

$$\sigma_c = 2\,c \tag{4}$$

With the objective of providing *compact* equations for the solution of the problem introduced before, the different variables in the model are normalized (or scaled) as follows.

The radial distance, r, divided by the radius of the cavity, a, defines the scaled radial distance, ρ, i.e.,

$$\rho = \frac{r}{a} \tag{5}$$

where $\rho = 1$ represents that radius of the cavity.

The depth of the cavity, h, divided by the radius of the cavity, a, defines the scaled depth of the cavity, ξ, i.e.,

$$\xi = \frac{h}{a} \tag{6}$$

The cohesion, c, of the ground divided by the unit weight of the ground, γ, and the cavity radius, a, defines the scaled cohesion, $\tilde{c}$, i.e.,

$$\tilde{c} = \frac{c}{\gamma a} \tag{7}$$

Similarly, the scaled internal pressure at the *crown*, $\tilde{p}_s$, and the scaled ground surcharge load, $\tilde{q}_s$, are defined,

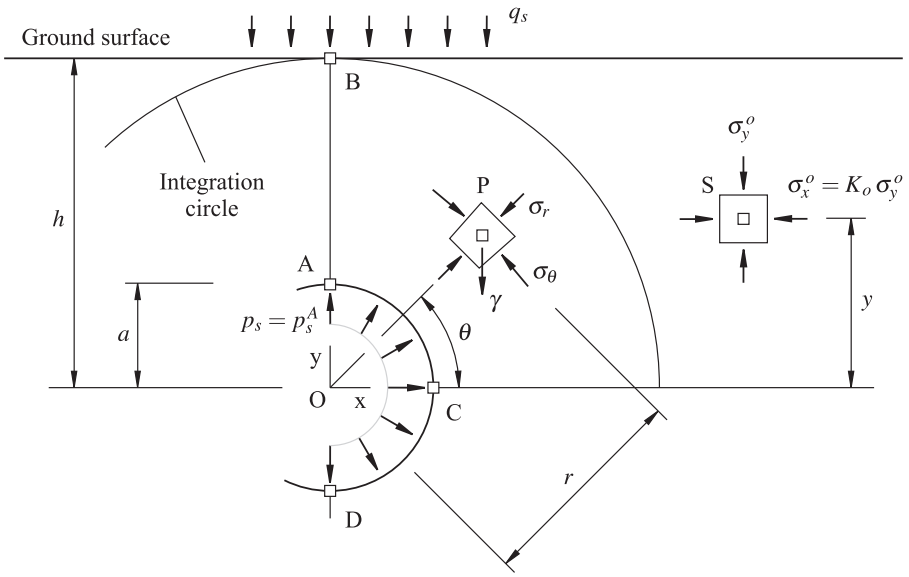

Figure 14. Problem of assessing the stability of a cylindrical or spherical (*contracting* or *expanding*) shallow cavity in dry ground.

respectively, as follows

$$\tilde{p}_s = \frac{p_s}{\gamma a}; \qquad \tilde{q}_s = \frac{q_s}{\gamma a} \tag{8}$$

The scaling rules introduced by equations (7) and (8) can be applied to the *in-situ* vertical and horizontal stresses given by equations (1) and (2), respectively, to define the scaled *in-situ* vertical and horizontal stresses, $\tilde{\sigma}_y^o$ and $\tilde{\sigma}_x^o$, respectively, as follows

$$\tilde{\sigma}_y^o = \tilde{q}_s + \xi - \frac{y}{a}; \qquad \tilde{\sigma}_x^o = K_o\,\tilde{\sigma}_y^o \tag{9}$$

In later sections, to investigate the effect of the (scaled) internal pressure, $\tilde{p}_s$, on the stability of the cavity in Figure 14, the *in-situ* vertical stress at the *crown* level (point *A*) *prior* to excavation is considered to be a *reference* vertical stress or internal pressure. This (scaled) reference internal pressure is denoted as $\tilde{p}_s^o$ and is obtained by considering $y/a = 1$ in the (left-side) equation (9), i.e.,

$$\tilde{p}_s^o = \tilde{q}_s + \xi - 1 \tag{10}$$

With the scaled reference internal pressure defined by equation (10), any scaled internal pressure at the *crown* of the cavity, $\tilde{p}_s$, can be expressed as a factor, $f_{\tilde{p}s}$, of the scaled reference internal pressure, i.e.,

$$\tilde{p}_s = f_{\tilde{p}s}\,\tilde{p}_s^o \tag{11}$$

Note that when the factor $f_{\tilde{p}s}$ in equation (11) is smaller than one, the case corresponds to that of a *contracting* cavity, i.e., the case in which the cavity is excavated and a (*crown*) internal pressure smaller than the original *in-situ* vertical stress (at the *crown*) is applied. Also, when the factor $f_{\tilde{p}s}$ in equation (11) is larger than one, then the case corresponds to that of an *expanding* cavity, i.e., the case in which the cavity is excavated and a (*crown*) internal pressure larger than the original *in-situ* vertical stress (at the *crown*) is applied.

3.2. Solution of stress fields

Figure 15 represents the stress fields inside and outside the integration circle in Figure 14, for the case of a *contracting* cylindrical opening at a scaled depth, $\xi = h/a = 3.5$, obtained with the analytical solution developed in this study. The cavity is assumed to be at the verge of collapse (i.e., at a limit state of equilibrium) with values of (critical) cohesion, $\tilde{c}_{cr} = 1.25$, scaled ground surcharge load, $\tilde{q}_s = 0.632$, and scaled *crown* internal pressure, $\tilde{p}_s = 0.243$. In Figure 15 the crosses represent the directions and magnitudes of the scaled radial and tangential (or hoop) stresses, $\tilde{\sigma}_r$ and $\tilde{\sigma}_\theta$, respectively, inside the integration circle, obtained with the analytical solution to be presented below. Outside the integration circle, the crosses represent the directions and magnitudes of the scaled *in-situ* vertical and horizontal stresses, $\tilde{\sigma}_x^o$ and $\tilde{\sigma}_y^o$, respectively, as defined by equation (9) with a

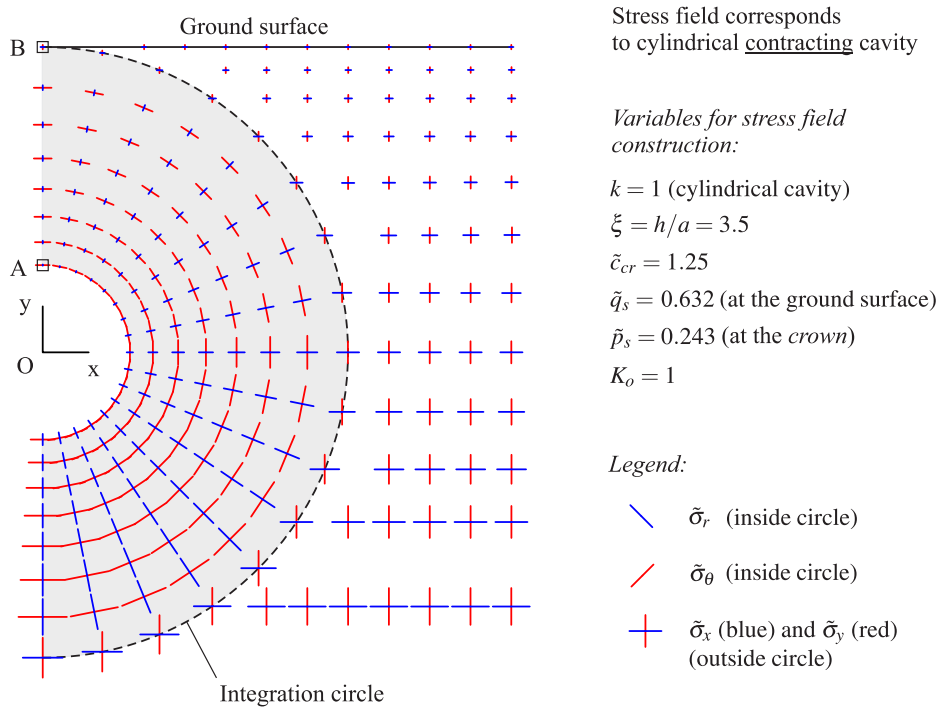

Figure 15. Stress fields inside and outside the integration circle in Figure 14 obtained with the proposed analytical solution for a *contracting* cylindrical opening.

coefficient of earth pressure at rest, $K_o = 1$.

Appendix A presents a detailed derivation of the equations conforming the solution represented in Figure 15 (the reader is also referred to that appendix for a discussion of several other features of the analytical solution). Below, only the main equations are transcribed from the appendix.

For the problem represented in Figure 15, the scaled radial stress, $\tilde{\sigma}_r(\rho,\theta)$, inside the integration circle is computed with the following equation

$$\tilde{\sigma}_r(\rho,\theta) = \tilde{\sigma}_r^{AB}(\rho) + \rho\,(1-\sin\theta) \tag{12}$$

while the scaled hoop stress, $\tilde{\sigma}_\theta(\rho,\theta)$, is computed with the equation

$$\tilde{\sigma}_\theta(\rho,\theta) = \tilde{\sigma}_\theta^{AB}(\rho) + \rho\,(1-\sin\theta) \tag{13}$$

In equations (12) and (13), $\tilde{\sigma}_r^{AB}(\rho)$ and $\tilde{\sigma}_\theta^{AB}(\rho)$ refer to the solution for the scaled radial and hoop stresses, respectively, along the segment AB in Figure 14. For *contracting* cavities, the scaled radial stress, $\tilde{\sigma}_r^{AB}(\rho)$, is computed with the equation

$$\tilde{\sigma}_r^{AB}(\rho) = \tilde{q}_s + \xi - \rho + 2k\tilde{c}_{cr}\ln\frac{\rho}{\xi} \tag{14}$$

while the scaled hoop stress, $\tilde{\sigma}_\theta^{AB}(\rho)$, is computed with the equation

$$\tilde{\sigma}_\theta^{AB}(\rho) = \tilde{\sigma}_r^{AB}(\rho) + 2\tilde{c}_{cr} \tag{15}$$

In equation (14), the parameter k is such that $k = 1$ implies that the cavity is cylindrical, while $k = 2$ implies that the cavity is spherical. Also, in equations (14) and (15), the scaled cohesion of the ground is referred to as $\tilde{c}_{cr}$, to enforce the idea that the cavity is at a critical state of equilibrium for the given values of scaled *crown* internal pressure, $\tilde{p}_s$, and ground surcharge load, $\tilde{q}_s$ (the fact that the cavity in Figure 14 is at a limiting stage of equilibrium is a fundamental assumption made to derive the solution in Appendix A).

The scaled internal pressure at the *crown* of the cavity, $\tilde{p}_s = \tilde{p}_s^A$ (see Figure 14), compatible with the limit state of equilibrium is obtained by making $\rho = 1$ and $\theta = \pi/2$ in equation (12) —together with equation (14). This gives

$$\tilde{p}_s = \tilde{q}_s + \xi - 1 - 2k\tilde{c}_{cr}\ln\xi \tag{16}$$

It is emphasized that the stress field inside the integration circle represented in Figure 14 is compatible with a plastic state (i.e., the ground inside the integration circle is failing plastically) while the stress field outside the integration circle, defined by the *in-situ* stresses, is compatible with an elastic state (the ground outside the integration circle remains in the elastic state). A proof of these statements is also provided in Appendix A.

Figure 16, which is equivalent to Figure 15 (for *contracting* cavities), represents the stress fields inside and outside the integration circle in Figure 14 for the case of a cylindrical *expanding* cavity, for the values of scaled variables indicated on the right-side of the figure (i.e., $\xi = 3.5$, $\tilde{q}_s = 0.632$, $\tilde{p}_s = 6.264$, $\tilde{p}_s^o = 3.132$ and $K_o = 1$). In Figure 16 the applied *crown* internal pressure is $\tilde{p}_s = 2\,\tilde{p}_s^o$ —i.e., the factor $f_{\tilde{p}s}$ in equation (11) is considered to be equal to two.

As for the case of *contracting* cavities, Appendix A presents the detailed derivation of the equations conforming the solution represented in Figure 16, together with a discussion of other features of the solution that also apply to *expanding* cavities. Below, only the main equations are transcribed from that appendix.

For the problem represented in Figure 16, the scaled radial and hoop stresses, $\tilde{\sigma}_r(\rho,\theta)$ and $\tilde{\sigma}_\theta(\rho,\theta)$, respectively, are computed using the same equations (12) and (13), respectively. In these equations, the scaled radial stress along the segment AB, $\tilde{\sigma}_r^{AB}(\rho)$, is computed with the equation

$$\tilde{\sigma}_r^{AB}(\rho) = \tilde{q}_s + \xi - \rho - 2k\tilde{c}_{cr}\ln\frac{\rho}{\xi} \tag{17}$$

while the scaled hoop stress, $\tilde{\sigma}_\theta^{AB}(\rho)$, is computed with the equation

$$\tilde{\sigma}_\theta^{AB}(\rho) = \tilde{\sigma}_r^{AB}(\rho) - 2\tilde{c}_{cr} \tag{18}$$

As for the case of *contracting* cavities discussed earlier on, the parameter k in equation (17) controls whether the cavity is cylindrical or spherical ($k = 1$ or 2, respectively) and the scaled cohesion of the ground is referred to as $\tilde{c}_{cr}$ to enforce the idea that the cavity is at a critical state of equilibrium. Also, it is emphasized that the stress field inside the integration circle represented in Figure 16 is compatible with a plastic state (i.e., the ground inside the integration circle is failing plastically) while the stress field outside the integration circle, defined by the *in-situ* stresses, is compatible with an elastic state (the ground remains elastic).

The scaled *crown* internal pressure, $\tilde{p}_s = \tilde{p}_s^A$ (see Figure 14), compatible with the limit state of equilibrium is again obtained by making $\rho = 1$ and $\theta = \pi/2$ in equation (12) —this time together with equation (17). This gives

$$\tilde{p}_s = \tilde{q}_s + \xi - 1 + 2k\tilde{c}_{cr}\ln\xi \tag{19}$$

The following sections discuss various observations of theoretical-practical interest that can be made from the solution conformed by the equations introduced above.

3.3. Stability of contracting cavities

To characterize the stability of the openings in terms of a single scalar parameter, a factor of safety is introduced in the formulation. The widely accepted definition of factor of safety used in slope stability analyses states that the factor of safety, *FS*, is the ratio of the shear strength of the material (e.g., the shear strength along a potential shear failure surface) and the shear stress (along the same failure surface) required for equilibrium (see, for example, Abramson, L.W. et al. 2002; Coduto et al. 2011). Therefore, if the cavity in Figure 14 is excavated in a ground with cohesion, c, then the *critical* scaled cohesion, $\tilde{c}_{cr}$, that makes the cavity to be at a critical state of equilibrium can be determined from the factor of safety, *FS*, as follows

$$\tilde{c}_{cr} = \frac{\tilde{c}}{FS} \tag{20}$$

Replacing equation (20) into equation (16) and solving for *FS*, the factor of safety for the *contracting* cavity in Figure 14 results

$$FS = \frac{2k\tilde{c}\ln\xi}{\tilde{q}_s - \tilde{p}_s + \xi - 1} \tag{21}$$

Some relevant observations can be made from equation (21).

A first observation is that the factor k that dictates whether the opening is cylindrical or spherical (when $k = 1$ or 2, respectively) acts as a multiplier in the numerator of equation (21). Therefore, with all other variables being

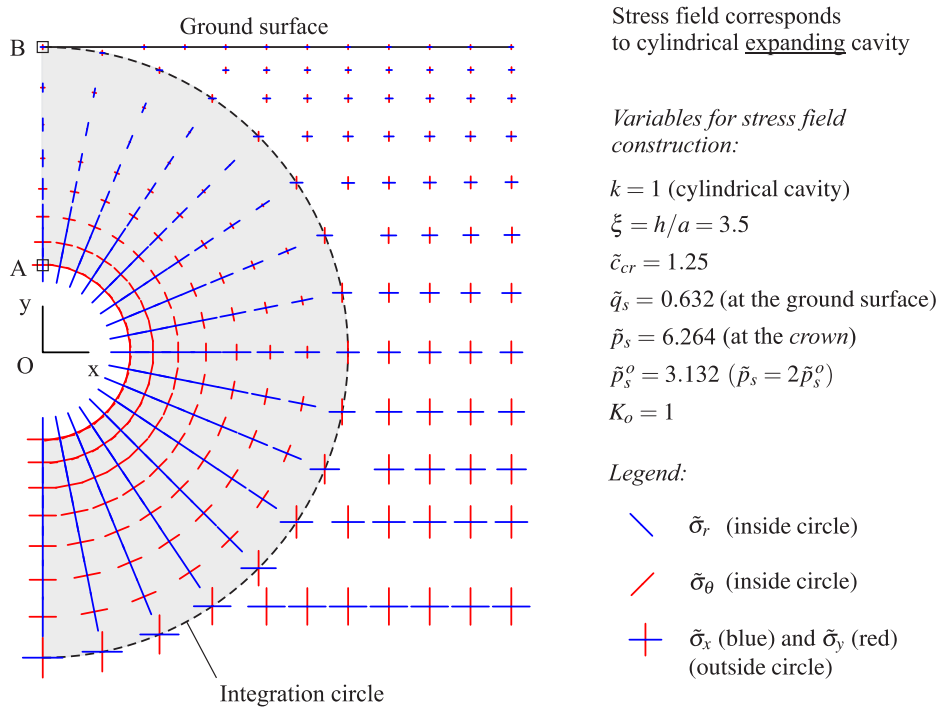

Figure 16. Stress fields inside and outside the integration circle in Figure 14 obtained with the proposed analytical solution for an *expanding* cylindrical opening.

the same (i.e., cavity radius and depth, ground strength, *crown* internal pressure and ground surcharge load) a spherical cavity has a factor of safety that is twice the factor of safety of a cylindrical cavity (this prediction is confirmed using numerical models, as discussed in a later section).

A second observation is with regard to the effect of the scaled depth, ξ, on the stability of the cavity. Figure 17 represents the relationship between the factor of safety, FS, and the scaled cohesion, $\tilde{c}$, obtained with equation (21), for a cylindrical *contracting* opening at different scaled depths, ξ, for particular cases of null *crown* internal pressure ($\tilde{p}_s = 0$) and null ground surcharge load ($\tilde{q}_s = 0$). The horizontal line of ordinate $FS = 1$ represents the critical stability condition (i.e., cases of cavities above the line $FS = 1$ are stable, while cases of cavities below the line $FS = 1$ are unstable). The representation in Figure 17 indicates the expected result that for cavities of the same radius and same depth (i.e., cavities with the same value of ξ) the factor of safety increases as the strength of the ground increases. The representation in Figure 17 also indicates the somehow counter intuitive result that as the cavity depth increases in a ground with constant shear strength, the factor of safety of the cavity decreases. This observation, to be confirmed in later sections with numerical models, can be explained by the fact that as the cavity depth increases (for the same ground shear strength), the magnitudes of *in-situ* stresses that produce the redistribution of stresses around the cavity also increase. This increase in magnitude of stresses facilitates the development of a redistributed plastic region around the cavity that eventually reaches the ground surface to produce a limit state of equilibrium.

A third observation is with regard to the influence of the *crown* internal pressure on the stability of the cavity. The influence of the scaled *crown* internal pressure, $\tilde{p}_s$, on the factor of safety can be conveniently analyzed using the internal pressure factor, $f_{\tilde{p}s}$, introduced in the previous section (see equation 11). Considering the reference internal pressure, $\tilde{p}_s^o$ (equation 10), representing the vertical *in-situ* stress prior to excavation at the cavity *crown* level, the internal pressure factor, $f_{\tilde{p}s}$, results

$$f_{\tilde{p}s} = \frac{\tilde{p}_s}{\tilde{p}_s^o} \tag{22}$$

The factor $f_{\tilde{p}s}$ defined by equation (22) is such that $f_{\tilde{p}s} = 0$ implies that the applied *crown* internal pressure is zero, while $f_{\tilde{p}s} = 1$ implies that the *crown* internal pressure is equal to the *in-situ* vertical stress (prior to excavation) at the *crown* level (i.e., $f_{\tilde{p}s} = 1$ corresponds to the case in which the cavity is excavated but the *in-situ* stresses are restored, as if no excavation has taken place).

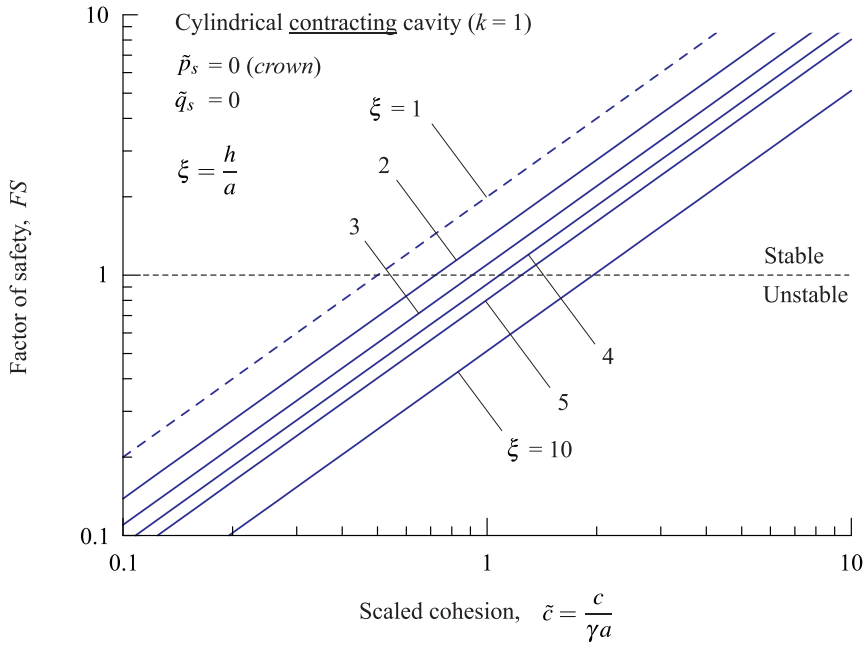

Figure 17. Graphical representation of the relationship between factor of safety and scaled ground cohesion for *contracting* unsupported cylindrical cavities as a function of the scaled depth.

Replacing equation (10) into equation (11) and the resulting equation into equation (21), the factor of safety, *FS*, can now be expressed in terms of the internal pressure factor, $f_{\tilde{p}s}$, given by equation (22); i.e.,

$$FS = \frac{2k\tilde{c}\ln\xi}{(1-f_{\tilde{p}s})(\tilde{q}_s+\xi-1)} \tag{23}$$

Figure 18 represents the relationship between the factor of safety, *FS*, and the scaled cohesion, $\tilde{c}$, obtained with equation (23), for a cylindrical *contracting* opening and for different scaled (*crown*) internal pressures, defined by the factor $f_{\tilde{p}s}$. The representation in Figure 18 corresponds to a cavity at a scaled depth, $\xi = 2$, with zero ground surcharge load. Note that the line corresponding to $f_{\tilde{p}s} = 0$ in Figure 18 is the same line corresponding to $\xi = 2$ in Figure 17. Also, as expected, when the internal pressure factor, $f_{\tilde{p}s}$, increases from the minimum value of zero, the factor of safety also increases. For the limiting case of *contracting* cavity in which $f_{\tilde{p}s} = 1$, as expected, the factor of safety becomes infinite (consider the case $f_{\tilde{p}s} = 1$ in equation 23).
To quantify the increase of factor of safety with the increase of internal pressure factor, $f_{\tilde{p}s}$, the ratio of factors of safety of cavities with arbitrary *crown* internal pressure, $FS(f_{\tilde{p}s})$, and the particular case of zero *crown* internal pressure, $FS(0)$, to be called the factor of safety ratio, $f_{FS}^{\tilde{p}s}$, is defined as follows

$$f_{FS}^{\tilde{p}s} = \frac{FS(f_{\tilde{p}s})}{FS(0)} \tag{24}$$

Replacing the numerator and denominator of equation (24), with equation (23) for the cases of arbitrary value of internal pressure factor, $f_{\tilde{p}s}$, and zero internal pressure factor ($f_{\tilde{p}s} = 0$), equation (24) becomes

$$f_{FS}^{\tilde{p}s} = \frac{1}{1-f_{\tilde{p}s}} \tag{25}$$

Figure 19 represents the relationship between the factor of safety ratio, $f_{FS}^{\tilde{p}s}$, and the internal pressure factor, $f_{\tilde{p}s}$, defined by equations (25) and (22), respectively. Note that the factor $f_{FS}^{\tilde{p}s}$ in equation (25), depends only on the factor $f_{\tilde{p}s}$; therefore, in contrast with the representations in Figures 17 and 18, the representation in Figure 19 is valid for both cylindrical and spherical cavities for any depth and for any ground surcharge load. The representation in Figure 19 shows, as expected, that when $f_{\tilde{p}s} = 0$ (case of zero *crown* internal pressure), $f_{FS}^{\tilde{p}s} = 1$, and when $f_{\tilde{p}s} = 1$ (case of no excavation), the factor $f_{FS}^{\tilde{p}s}$ tends to infinity. The representation also shows that for the case in which the internal pressure is half the value of the *in-situ* reference internal pressure

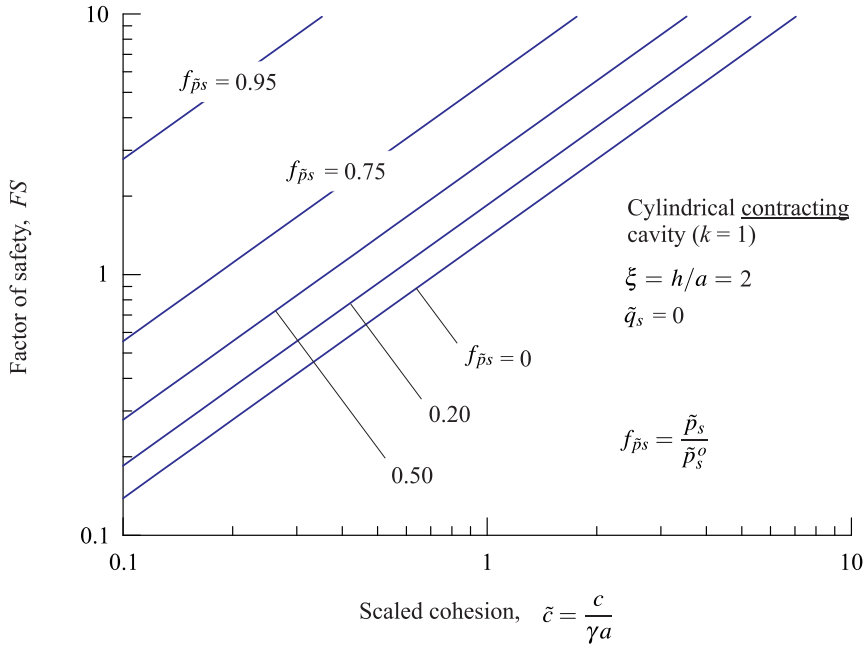

Figure 18. Graphical representation of the relationship between factor of safety and scaled ground cohesion for *contracting* cylindrical cavities at the scaled depth, $\xi = 2$, for increasing values of scaled *crown* internal pressure defined by the factor, $f_{\tilde{p}s}$.

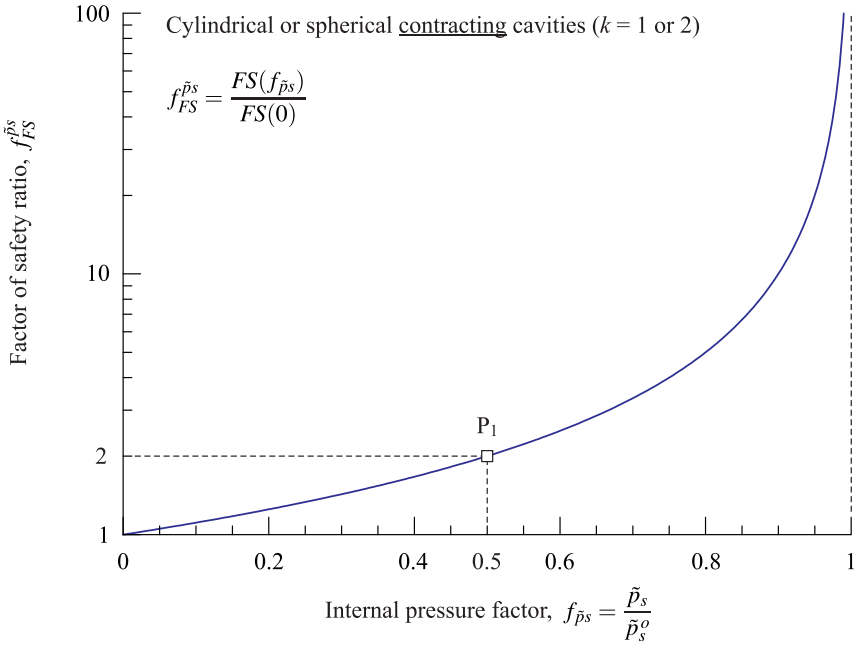

Figure 19. Graphical representation of the relationship between the factor of safety ratio, $f_{FS}^{\tilde{p}s}$, and internal pressure factor, $f_{\tilde{p}s}$, valid for both cylindrical and spherical *contracting* cavities.

(i.e., $f_{\tilde{p}s} = 0.5$) the factor of safety of the *contracting* cavity is twice the value of the factor of safety for the cavity with zero *crown* internal pressure (i.e., $f_{FS}^{\tilde{p}s} = 2$).

As mentioned in Section 3.2, Appendix A discusses several other features of the analytical solution for *contracting* cavities presented above.

One consideration discussed in Appendix A is about the distribution of internal pressure that the solution considers for the cavity. The solution assumes that the internal pressure increases with depth inside the cavity in a *lithostatic* manner, as if the internal pressure is provided by an imaginary pressurized gas which has the same unit weight as the ground surrounding the cavity. This means that if the internal pressure at the *crown* of the cavity (point *A* in Figure 14) is $p_s = p_s^A$, then the internal pressure at the *spring line* of the cavity (point *C* in Figure 14) is $p_s^C = p_s^A + \gamma a$ (see left-side equation A-18 in Appendix A). It is because of this *lithostatic* increase of internal pressure that equation (21) predicts a finite value of factor of safety for the hypothetical case of a shallowest possible cavity, $\xi = 1$, when $\tilde{p}_s = 0$ and $\tilde{q}_s = 0$ (see line labelled as $\xi = 1$ in Figure 17). In such case, and referring now to equation (21), the limit of the term $\ln(\xi)/(\xi - 1)$ when ξ tends to one becomes equal to one in that equation, and the factor of safety for the shallowest possible cavity, $\xi = 1$, (with $\tilde{p}_s = \tilde{q}_s = 0$) becomes equal to $2k\tilde{c}$. If $\tilde{q}_s - \tilde{p}_s \neq 0$ (i.e., if the applied ground surcharge load or internal pressure do not equilibrate each other) then the limit of the term $\ln(\xi)/(\xi - 1)$ when ξ tends to one becomes equal to zero, in equation (21), and the factor of safety for the shallowest possible cavity, $\xi = 1$, becomes zero (no equilibrium is possible).

The effect of considering internal pressure distributions other than *lithostatic* on the factor of safety is addressed in Appendix B. There, it is shown that numerical (finite-difference) models of *contracting* cavities with *uniform* distributions of internal pressure equal to p_s (where p_s is the *crown* internal pressure in the analytical solution presented above), yield factors of safety that are conservative (i.e., smaller than) those corresponding to cavities with the *lithostatic* internal pressure considered by the analytical solution presented above.

Another consideration discussed in Appendix A is with regard to the coefficient of earth pressure at rest, K_o. For the analytical solution presented above to be a statically admissible solution (and therefore to be a safe estimate of the stability condition of the cavity) the coefficient K_o must be equal to one. The effect of considering coefficients K_o other than one on the factor of safety is also discussed in Appendix B. The appendix shows that numerical finite-difference models of *contracting* cavities with *in-situ* stresses characterized by coefficients of earth pressure at rest, K_o, different from one yield factors of safety that are similar to those obtained for cavities with *in-situ* stresses characterized by coefficients K_o equal to one.

3.4. Stability of expanding cavities

Introducing the same definition of factor of safety as in Section 3.3 (see equation 20), the factor of safety for the *expanding* cavity in Figure 14 is obtained from equation (19) and results to be

$$FS = -\frac{2k\tilde{c}\ln\xi}{\tilde{q}_s - \tilde{p}_s + \xi - 1} \tag{26}$$

Note that the main difference between equation (26) above (that applies to *expanding* cavities) and equation (21) (that applies to *contracting* cavities) is the negative sign in equation (26) and the fact that the scaled *crown* internal pressure, $\tilde{p}_s$, is now larger than the reference *crown* internal pressure, $\tilde{p}_s^o$, given by equation (10). Therefore, most of the observations made for *contracting* cavities in Section 3.3 also apply to *expanding* cavities, including the fact that a spherical cavity has a factor of safety that is twice the factor of safety for a cylindrical cavity (when all other input variables such as depth, strength and loading are the same).

Another observation is with regard to the influence of the scaled cavity depth, ξ, on the stability of the cavity. Figures 20 and 21 show similar representations as in Figure 17 (for *contracting* cavities), this time obtained with equation (26), when the applied *crown* internal pressure is $\tilde{p}_s = 1.5\,\tilde{p}_s^o$ and $\tilde{p}_s = 2\,\tilde{p}_s^o$, respectively, with $\tilde{p}_s^o$ given by equation (10). The interpretation Figures 20 and 21 is the same to that for Figure 17, discussed in the previous section. Comparison of Figures 20 and 21 indicates that as the *crown* internal pressure increases ($\tilde{p}_s$ increases from $1.5\,\tilde{p}_s^o$ to $2\,\tilde{p}_s^o$), the lines corresponding to different scaled depths, ξ, shift downward, indicating that the factor of safety decreases. This is the expected result since as the internal pressure increases (with all other parameters being the same), the factor of safety must decrease. Considering now the different curves corresponding to different depths in either Figure 20 or Figure 21, it is observed that as the cavity depth increases in a ground with constant shear strength (and with an applied internal pressure that is a constant ratio of the *in-situ* vertical stress at that level), then the factor of safety decreases. Certainly, if the *crown* internal

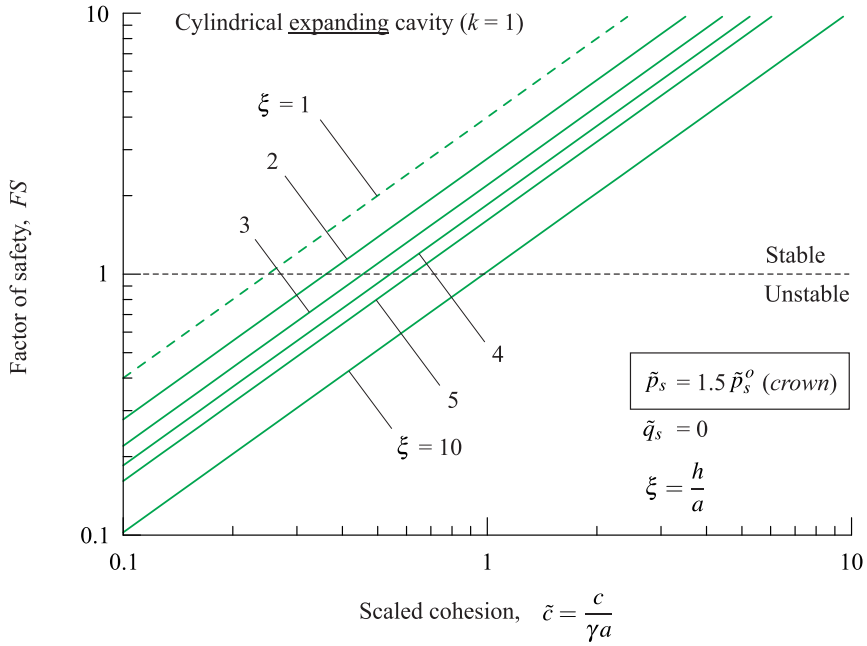

Figure 20. Graphical representation of the relationship between factor of safety and scaled ground cohesion for *expanding* cylindrical cavities as a function of the scaled depth. The representation corresponds to a scaled *crown* internal pressure $\tilde{p}_s = 1.5\,\tilde{p}_s^o$.

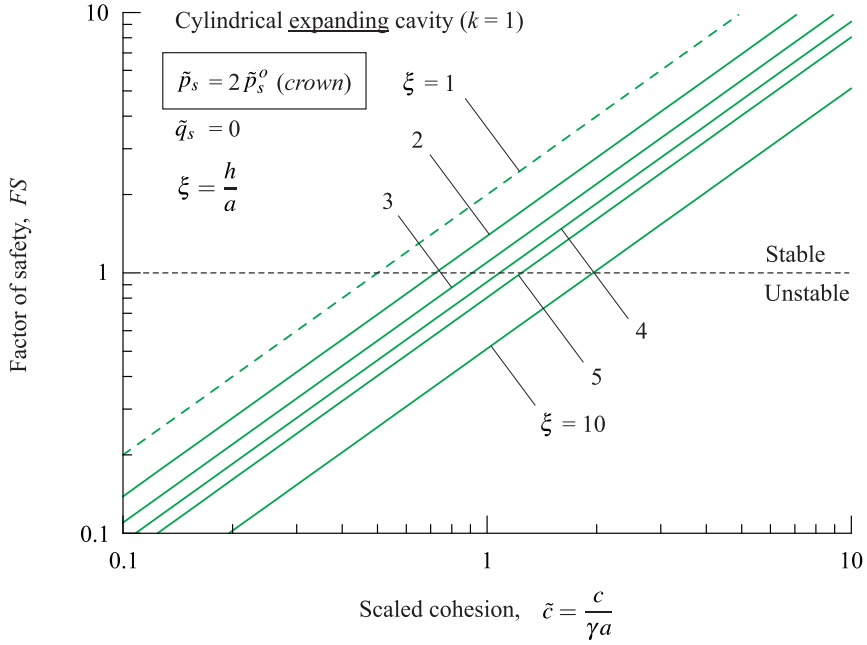

Figure 21. Graphical representation of the relationship between factor of safety and scaled ground cohesion for *expanding* cylindrical cavities as a function of the scaled depth. The representation corresponds to a scaled *crown* internal pressure $\tilde{p}_s = 2\,\tilde{p}_s^o$.

pressure in equation (26) is considered to be constant (or a constant ratio of the shear strength) and the depth is increased, the factor of safety can be expected to increase. This is shown in Figure 22 that includes a similar diagram as in Figure 20 (or Figure 21), but this time considering that the *crown* internal pressure is equal to 5 times the value of considered scaled cohesion. The different curves in Figure 22 correspond to different scaled depths, and as expected, the larger the scaled depth considered, the larger the resulting factor of safety.

Comparison of Figures 17 and 21 shows that the position of the lines corresponding to the different scaled depths, ξ, are identical, and therefore that the same relationship between factor of safety, *FS*, and scaled cohesion, $\tilde{c}$, with scaled depth, ξ, is the same for *contracting* cavities with zero *crown* internal pressure (as in Figure 17) and for *expanding* cavities with a *crown* internal pressure that is two times the *in-situ* vertical stress at the *crown* level (as in Figure 21). This is a relevant observation that has implications for the design of shallow underground cavities that are subjected to changes in pressure, as in CAES systems: if the unlined underground cavity is designed to have a certain factor of safety when there is no air pressure (other than atmospheric), then a convenient maximum value of air pressure to be considered for the cavity is two times the *lithostatic* vertical stress value at the *crown*level (i.e., two times the vertical stress that existed at the *crown* level prior to excavation). This guarantees the same factor of safety for the cavity in the limiting states of working pressure, when the internal air pressure is zero (or atmospheric) and when the internal air pressure is the maximum working pressure. Any other intermediate pressure within these two limits will result in a factor of safety for the cavity that is higher than the design factor of safety (for zero internal pressure or an internal pressure equal to two times the *lithostatic* vertical stress at the *crown* level).

To illustrate this observation of equivalence of factors of safety for cavities with zero *crown* internal pressure and with *crown* internal pressure equal to twice the *in-situ* vertical stress value, an analysis similar to that in the previous section is presented below.

Replacing equation (11) into equation (10) and the resulting equation into equation (26), the factor of safety, *FS*, can now be expressed in terms of the internal pressure factor, $f_{\tilde{p}s}$, given by equation (22); i.e.,

$$FS = \frac{2\,k\,\tilde{c}\,\ln\xi}{(f_{\tilde{p}s}-1)\,(\tilde{q}_s+\xi-1)} \tag{27}$$

Also, the factor of safety ratio, $f_{FS}^{\tilde{p}s}$ (see equation 24), can be computed using equation (27). This gives

$$f_{FS}^{\tilde{p}s} = \frac{1}{f_{\tilde{p}s}-1} \tag{28}$$

Figures 23 and 24 show a similar representation as in Figures 18 and 19, respectively, this time obtained with equations (27) and (28), respectively. For *expanding* cavities, the representation in Figure 24 shows, as expected, that when $f_{\tilde{p}s}=1$ (case of no excavation), then $f_{FS}^{\tilde{p}s}$ tends to infinity, and when $f_{\tilde{p}s}=2$ (*crown* internal pressure is equal to twice the *in-situ* vertical stress), then $f_{FS}^{\tilde{p}s}=1$.

Similar considerations as for the analytical solution for *contracting* cavities discussed in Section 3.3 apply to the analytical solution for *expanding* cavities presented above. The reader is referred to Appendix B for a discussion on the assumptions made with regard to the *lithostatic* distribution of internal pressure in the cavity and the coefficient of earth pressure at rest, K_o, for the case of *expanding* cavities.

There is a particular consideration for *expanding* cavities that is not applicable to *contracting* cavities. This is with regard to the occurrence of tensile stresses inside the integration circle in Figure 14, for certain combinations of input variables, particularly, when the ground surcharge load is null. To derive the analytical solution for *expanding* cavities, the assumption is made that the radial stresses in the integration circle are major principal stresses and that the hoop stresses are minor principal stresses (see equation A-4 in Appendix A). This assumption is put in evidence in the representation of principal stresses in the form of crosses in Figure 16. For the case in which the scaled ground surcharge load, $\tilde{q}_s$, is null, equation (17) predicts a scaled radial stress, $\tilde{\sigma}_r^{AB}=0$, at point *B* on the ground surface (see Figure 14), and equation (18) predicts a scaled hoop stress $\tilde{\sigma}_\theta^{AB}=-2\,\tilde{c}_{cr}$ at the same point *B*. This means that the hoop stress becomes negative (or tensile) at the ground surface, and up to a certain depth below the ground surface. Since geomaterials, in general, do have limited strength in tension compared with the strength in compression, the prediction of tensile stresses in the analytical solution poses a problem, that in principle limits the applicability of the solution to predict values of factors of safety for *expanding* cavities. It is shown in Section 4 of this paper that numerical models that account for null tensile strength of the ground, display indeed the development of tensile failure near the ground surface, but the

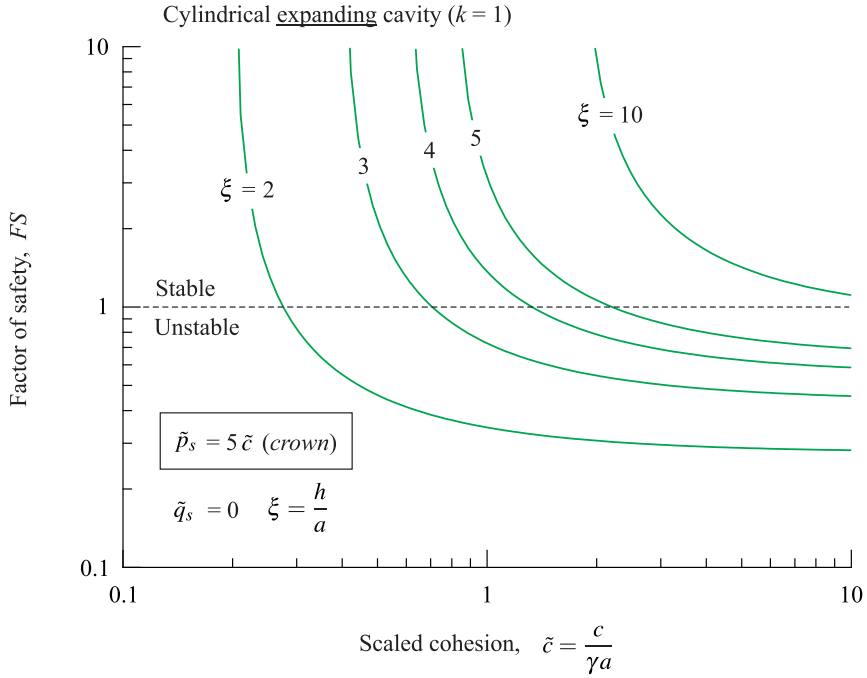

Figure 22. Graphical representation of the relationship between factor of safety and scaled ground cohesion for *expanding* cylindrical cavities as a function of the scaled depth. The representation corresponds to a scaled *crown* internal pressure $\tilde{p}_s = 5\,\tilde{c}$.

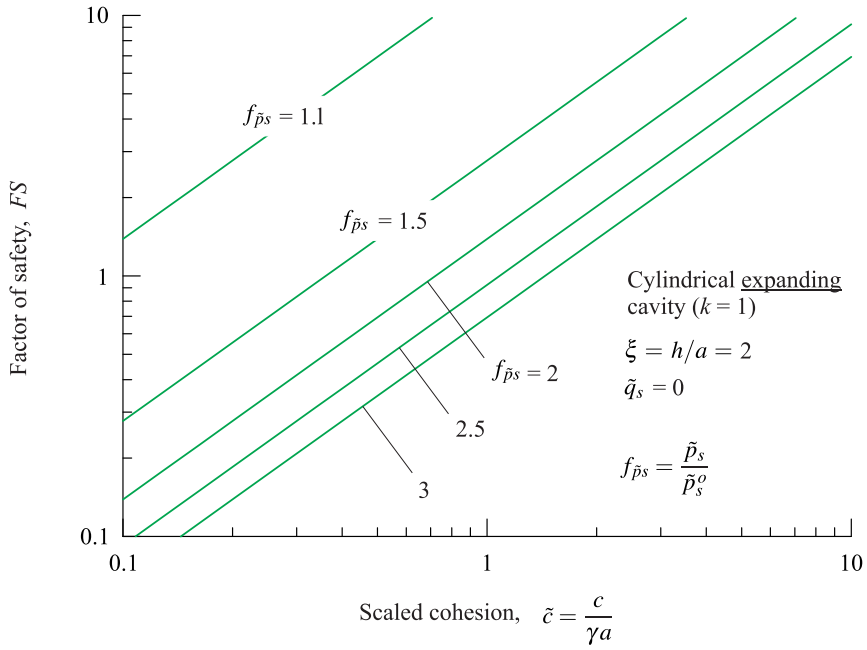

Figure 23. Graphical representation of the relationship between factor of safety and scaled ground cohesion for *expanding* cylindrical cavities at the scaled depth, $\xi = 2$, for increasing values of scaled *crown* internal pressure defined by the factor, $f_{\tilde{p}s}$.

factors of safety obtained from the numerical models are comparable to the ones obtained with the analytical solution presented above. Indeed, the values of factor of safety obtained with the analytical solution are lower than the ones obtained with the numerical models, as is expected to be the case from a statically admissible solution, in view of the lower bound theorem discussed earlier on in Section 2.

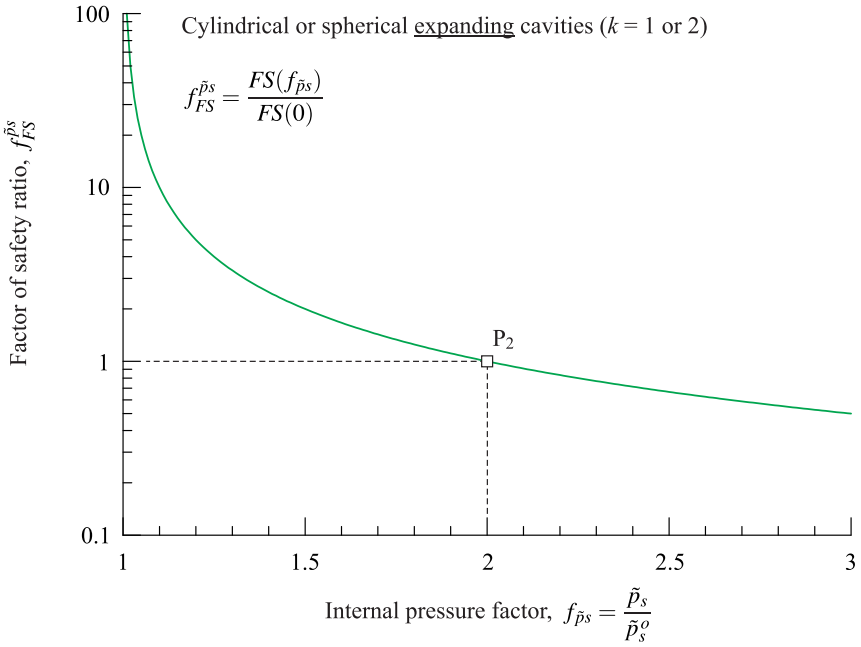

Figure 24. Graphical representation of the relationship between factor of safety ratio, $f_{FS}^{\tilde{p}s}$, and internal pressure factor, $f_{\tilde{p}s}$, valid for both cylindrical and spherical *expanding* cavities.

4. Comparison of factors of safety obtained from analytical and numerical finite-difference models

To confirm the observations made for *contracting* and *expanding* cavities in Sections 3.3 and 3.4, this section presents a comparison of results obtained with the proposed analytical model and with numerical models computed with the commercial finite-difference software FLAC (Itasca 2008), which implements the *strength reduction technique* discussed in Section 2.

For a shallow cavity in a Tresca material with scaled cohesion, $\tilde{c}$, if the cavity is stable for the given shear strength, the *strength reduction technique* consists in solving the problem repeatedly for *decreasing* values of shear strength, until the cavity is no longer stable. If in each solution step the given cohesion is divided by the factor r_{FS} (with $r_{FS} > 1$), and if the first unstable case (for a specified tolerance of the increment of the factor r_{FS}) corresponds to the critical scaled cohesion, $\tilde{c}_{cr}$, obtained with the critical factor, r_{FS}^{cr}, then the factor of safety, FS, is computed as follows

$$FS = r_{FS}^{cr} \quad \text{where} \quad \tilde{c}_{cr} = \frac{\tilde{c}}{r_{FS}^{cr}} \tag{29}$$

Alternatively, if the cavity is not stable for the given value of shear strength, the *strength reduction technique* consists in solving the problem repeatedly for *increasing* values of shear strength, until the cavity becomes stable again. If in each solution step the given cohesion is multiplied by the factor r_{FS} (with $r_{FS} > 1$), and if the first stable case corresponds to the critical scaled cohesion, $\tilde{c}_{cr}$, obtained with the critical factor, r_{FS}^{cr}, then the factor of safety, FS, is computed as follows

$$FS = \frac{1}{r_{FS}^{cr}} \quad \text{where} \quad \tilde{c}_{cr} = r_{FS}^{cr}\,\tilde{c} \tag{30}$$

To illustrate the implementation of the *strength reduction technique*, Figure 25 shows a sequence of computations of numerical models for a shallow cylindrical *contracting* cavity of scaled depth, $\xi = 4$, that is *unstable* for the given value of cohesion, $\tilde{c} = 1$ (as it will be discussed later on, the factor of safety for the cavity represented in Figure 25 is 0.968; i.e., it is less than one). The models consider values of scaled ground surcharge

load, $\tilde{q}_s = 0$, and scaled *crown* internal pressure, $\tilde{p}_s = 0$, with the *lithostatic* distribution of internal pressure discussed in Section 3.3. Furthermore, the models consider an initial horizontal-to-vertical stress ratio, $K_o = 1$; a value of Young's Modulus equal to 1,000 times the value of the scaled cohesion, $\tilde{c}$; a Poisson's ratio equal to 0.25 and a tensile strength equal to zero; also the models consider a mesh of square elements near the cavity of side length equal to 0.1 times the radius of the cavity.

The different plots in the Figure 25 correspond to models solved for the decreasing values of the factor, r_{FS}, indicated in each plot (note that the plots indicate factors $r_{FS} > 1$; this implies that the model is unstable for the given value of shear strength —see equation 30). The models represented in Figures 25a through 25e correspond to stable cavities, while the one in Figure 25f corresponds to the fist unstable case (for a value of tolerance of the sought factor of safety, $1/r_{FS} = 0.001$ —see equation 30). The two colors in the plots in Figure 25 represent the elements in the mesh that undergo plastic failure, whether in shear or tensile failure. Note that as the cohesion is decreased, the plastic failure grows around the cavity and *migrates* towards the ground surface until caving of the mass above the cavity takes place in the fist unstable case. It should be noted that although the computation of the mechanical models in Figure 25 is done in *small strain* mode, the plots in Figure 25 consider the deformed mesh of elements based on computed displacements with a specified large value of exaggeration, so as to reveal the outline of the deformation that takes place, particularly on the ground surface. To illustrate further the deformations, Figure 26 shows the same models represented in Figure 25, this time representing contours of magnitude of displacements for the decreasing values of cohesion (the caved zone is clearly seen in the first unstable model in Figure 26f).

Considering the input parameters listed above, the resulting factor of safety for the sequence of models in Figure 25 and Figure 26 result to be $FS = 0.968$; this value is the result of doing the operation $1/1.0334$ (see equation 30), where 1.0334 is the critical factor, r_{FS}^{cr}, found with the *strength reduction technique* (note that the model corresponding to this critical factor is not shown in the plots in Figure 25, and lies in between the models represented in Figures 25e and 25f).

As part of this study, a large number of numerical models were set up and computed for various conditions of input parameters. Figure 27 shows the first unstable case obtained for models with similar input parameters as in the models in Figures 25 and 26, but for values of scaled depths, ξ, equal to 1.5, 2, 3 and 4, respectively. Although evaluation of stability conditions for deeper cavities was also of interest, the scaled depth considered in the models was limited to 4 due to the need to extend the boundaries of the models and increase the number of elements required for computation —all this having a marked effect in the time required to compute the models.

Figure 28, which is similar to Figure 17, represents factors of safety as a function of scaled cohesion for *contracting* cavities at different scaled depths (the reader is referred to Section 3.3 for a discussion of Figure 17), this time including symbols that represent the values of factors of safety computed with the numerical models for different scaled depths (values of ξ equal to 1.5, 2, 3 and 4). The values of scaled parameters, $\tilde{p}_s = 0$ and $\tilde{q}_s = 0$, considered in the models are indicated in the figure. Table 2 lists the values of input parameters and resulting factors of safety for the 20 models represented in Figure 28 (in particular, the sequence of strength increase computations discussed already in Figures 25 and 26, corresponds to Case 4c in Table 2). The columns labelled as FS_A and FS_N in Table 2 correspond to the factors of safety obtained with the analytical model (equation 21) and with the numerical models, respectively. The column labelled as $f_{FS}^{A\text{-}N}$ represents the ratio of factors of safety obtained with the analytical solution and with the numerical solution, i.e.,

$$f_{FS}^{A\text{-}N} = \frac{FS \text{ [Proposed Analytical Model]}}{FS \text{ [Numerical (FLAC) Model]}} \tag{31}$$

When the mesh of the elements in the finite-difference (FLAC) models is fine enough (as with the case of the models discussed in this paper, based on a parametric evaluation of the effect of element mesh size on results —not included in this paper for space reasons) the factors of safety obtained with the *strength reduction technique* can be expected to be reasonably similar to the true factors of safety for the cavities. From Figure 28 it is seen that the symbols representing the numerical results are always located above the lines representing the analytical results. This means that the factors of safety obtained with the statically admissible solution are conservative and therefore safe estimates of the characteristic factor of safety for the cavities, this being the expected result given that the proposed analytical solution is a lower bound solution (see Section 2). The right-most column in Table 2 (see equation 31) indicates that the underestimation of stability conditions by the proposed analytical solution is within 10% of the assumed true solution.

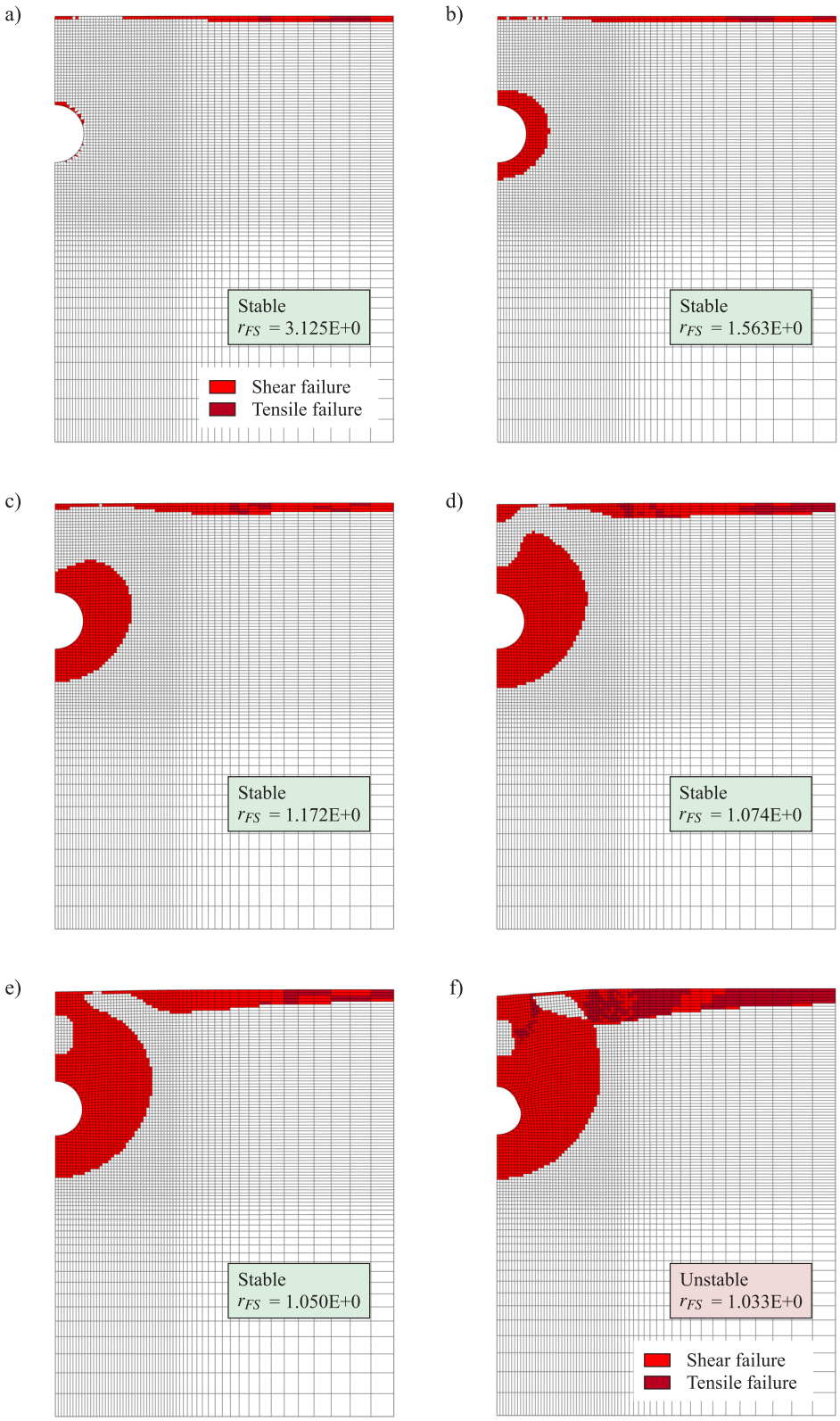

Figure 25. Sample sequence of computation of factor of safety for a cylindrical *contracting* cavity using the *strength reduction technique* in numerical (FLAC) models. The colored areas around the cavity and on the ground surface represent elements in the mesh that undergo plastic failure, in tension or compression. Plots a) through e) correspond to stable cavities, while plot f) corresponds to the first unstable situation (the sequence represented in the figure corresponds to Case 4c in Table 2).

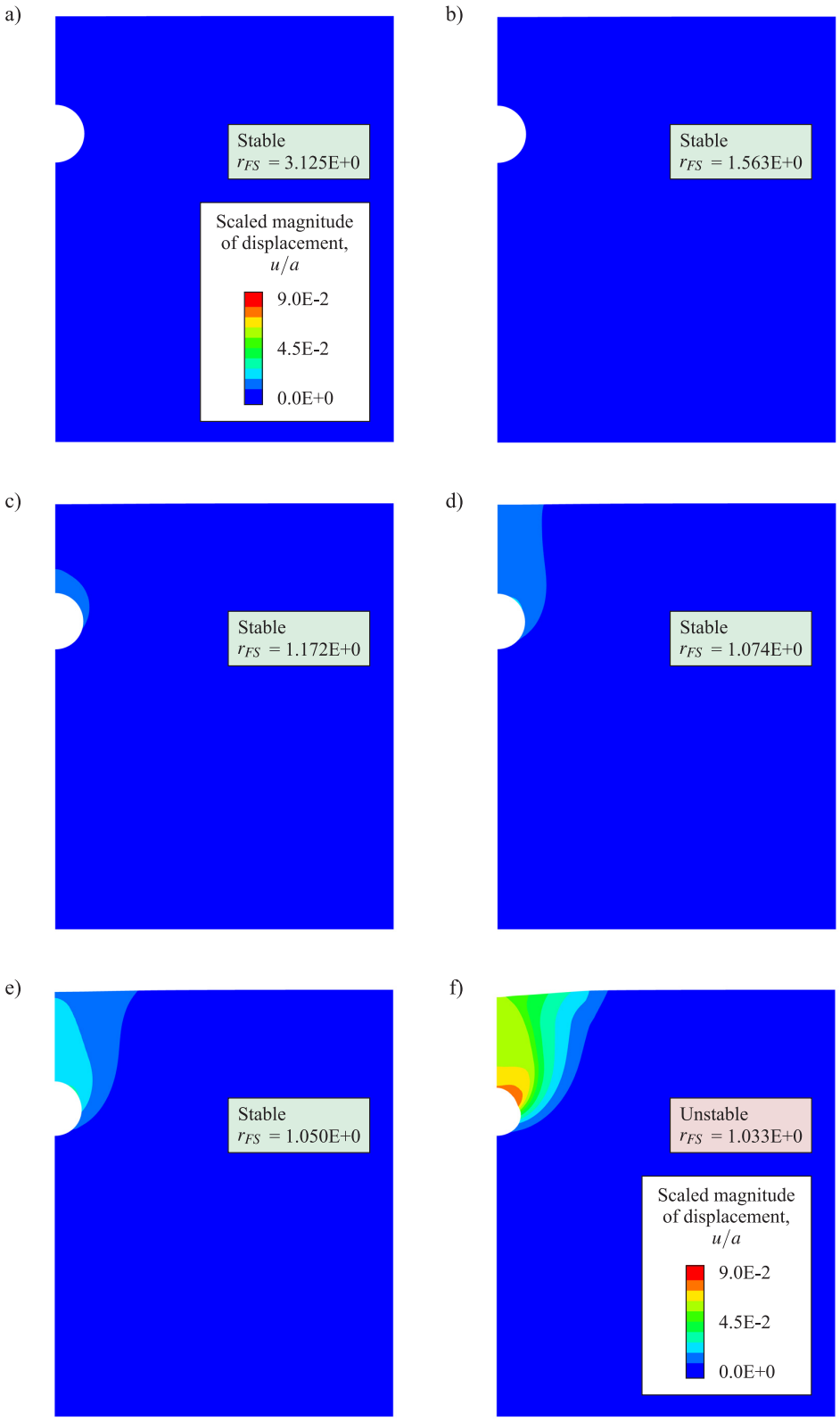

Figure 26. Representation of contours of magnitude of displacements for the same sequence of numerical models shown in Figure 25.

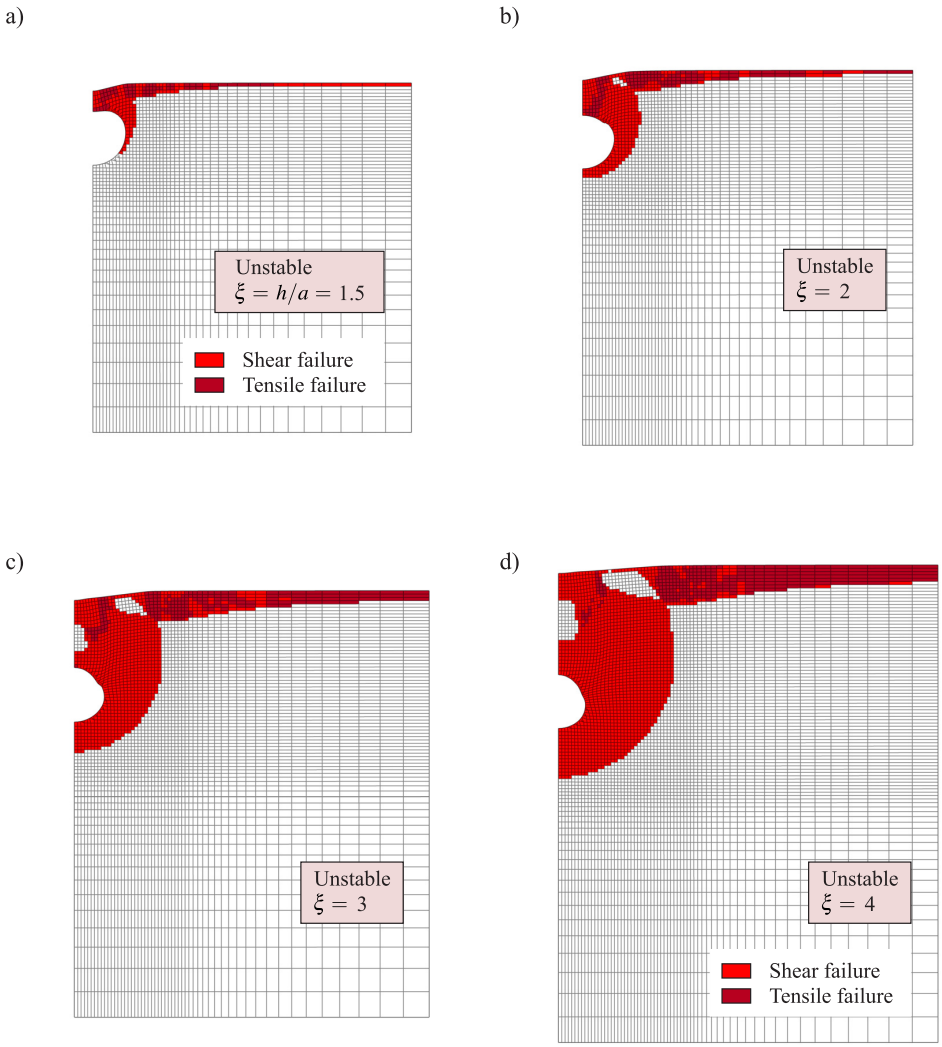

Figure 27. First unstable situation in the computation of factor of safety with numerical models for cylindrical *contracting* cavities at various scaled depths, ξ, corresponding values a) 1.5; b) 2; c) 3; and d) 4.

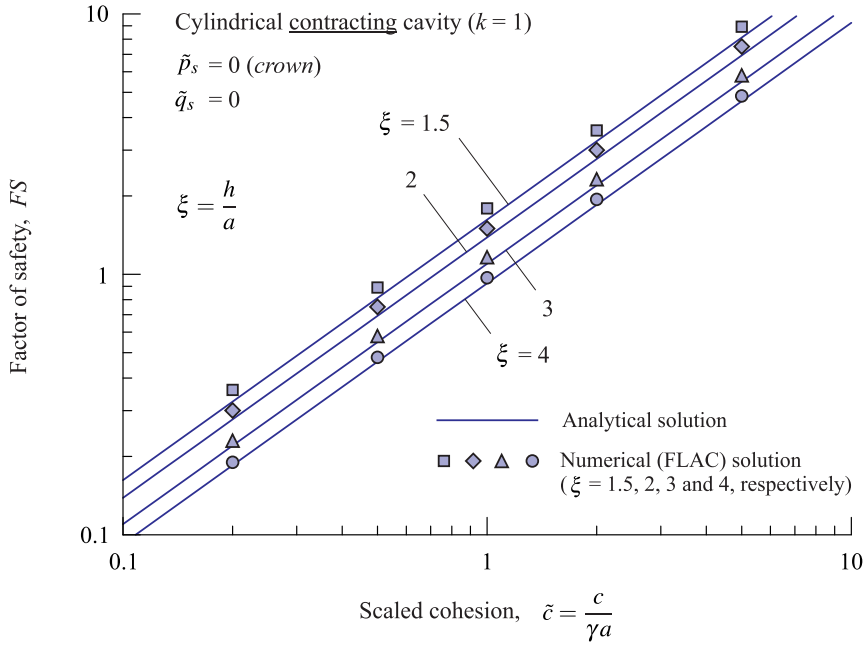

Figure 28. Graphical representation similar to that in Figure 17 showing the relationship between factor of safety and scaled ground cohesion for *contracting* cylindrical cavities at different scaled depths. The symbols in the diagram represent the factors of safety obtained with the numerical models.

Table 2. Summary of input data and results for different cases of cylindrical *contracting* cavities in cohesive ground solved with the numerical models (see Figure 28).

Case	ξ [-]	$\tilde{c}$ [-]	a [m]	h [m]	γ [kN/m^3]	c [kPa]	p_s [kPa]	FS_A [-]	FS_N [-]	$f_{FS}^{A\text{-}N}$ [-]
1a	1.5	0.2	4.4	6.6	17.4	15.312	0.00	0.324	0.36	0.90
1b	1.5	0.5	3.6	5.4	15.7	28.260	0.00	0.811	0.89	0.91
1c	1.5	1.0	4.4	6.6	24.0	105.600	0.00	1.622	1.79	0.91
1d	1.5	2.0	1.4	2.1	21.2	59.360	0.00	3.244	3.57	0.91
1e	1.5	5.0	2.3	3.5	17.0	195.500	0.00	8.109	8.93	0.91
2a	2.0	0.2	4.6	9.2	21.2	19.504	0.00	0.277	0.30	0.92
2b	2.0	0.5	1.9	3.8	24.3	23.085	0.00	0.693	0.75	0.92
2c	2.0	1.0	2.6	5.2	21.5	55.900	0.00	1.386	1.50	0.92
2d	2.0	2.0	3.5	7.0	20.8	145.600	0.00	2.773	3.00	0.92
2e	2.0	5.0	2.8	5.6	16.2	226.800	0.00	6.931	7.50	0.92
3a	3.0	0.2	3.9	11.7	24.2	18.876	0.00	0.220	0.23	0.96
3b	3.0	0.5	3.7	11.1	15.9	29.415	0.00	0.549	0.58	0.95
3c	3.0	1.0	2.3	6.9	15.0	34.500	0.00	1.099	1.16	0.95
3d	3.0	2.0	2.2	6.6	21.7	95.480	0.00	2.197	2.32	0.95
3e	3.0	5.0	1.4	4.2	20.5	143.500	0.00	5.493	5.81	0.95
4a	4.0	0.2	1.3	5.2	22.0	5.720	0.00	0.185	0.19	0.97
4b	4.0	0.5	3.6	14.4	19.9	35.820	0.00	0.462	0.48	0.96
4c	4.0	1.0	1.4	5.6	20.0	28.000	0.00	0.924	0.97	0.95
4d	4.0	2.0	1.9	7.6	20.1	76.380	0.00	1.848	1.94	0.95
4e	4.0	5.0	4.7	18.8	22.3	524.050	0.00	4.621	4.84	0.95

Results summarized in this table consider a scaled internal pressure at the *crown*, $\tilde{p}_s = p_s/(\gamma a) = 0$ and a scaled ground surcharge load, $\tilde{q}_s = 0$. The columns labelled as FS_A and FS_N correspond to the numerator and denominator of equation (31), respectively.

A similar comparison of analytical and numerical results as discussed above for cylindrical *contracting* cavities was carried out for cylindrical *expanding* cavities.

Figures 29, 30 and 31 are equivalent to Figures 25, 26 and 27, respectively, this time for *expanding* cavities and for a value of *crown* internal pressure equal to two times the value of *in-situ* vertical stress at the level of the *crown* (i.e., $\tilde{p}_s = 2\,\tilde{p}_s^o$), with all other parameters being the same as for the case of the *contracting* cavities discussed earlier on.

Figure 32 and Table 3 are equivalent to Figure 28 and Table 2, respectively, and allow the same observations as for the case of *contracting* cavities to be made with regard to small differences between analytical and numerical results. Figure 32 and Table 3, in particular, confirm the observation made in Section 3.4, that the factor of safety of a *contracting* cavity with zero *crown* internal pressure is equal to the factor of safety of an *expanding* cavity with *crown* internal pressure equal to two times the value of *in-situ* vertical stress at the level of the *crown* (with all other input parameters being the same).

It should be noted that the comparison of factors of safety obtained with the proposed statically admissible solution and with the numerical models presented in this section correspond, as indicated, to cylindrical cavities. Similar comparison was carried out for spherical cavities, using the same mesh of elements shown in Figures 27 and 31 and taking advantage of the axi-symmetrical capabilities in the software FLAC. The results obtained for spherical cavities confirmed the observations made in Sections 3.3 and 3.4, that when other input parameters are the same, spherical cavities do have factors of safety that are approximately twice the factors of safety for cylindrical cavities. Numerical models were also set up and solved for values of *crown* internal pressure different from zero (for *contracting* cavities) and different from two times the initial vertical stress at the *crown* level (for *expanding* cavities) and numerical results compared well with the predictions made with the proposed analytical models, according to the relationships in Figures 18 and 19 discussed in Section 3.3, and the relationships in Figures 23 and 24 discussed in in Section 3.4.

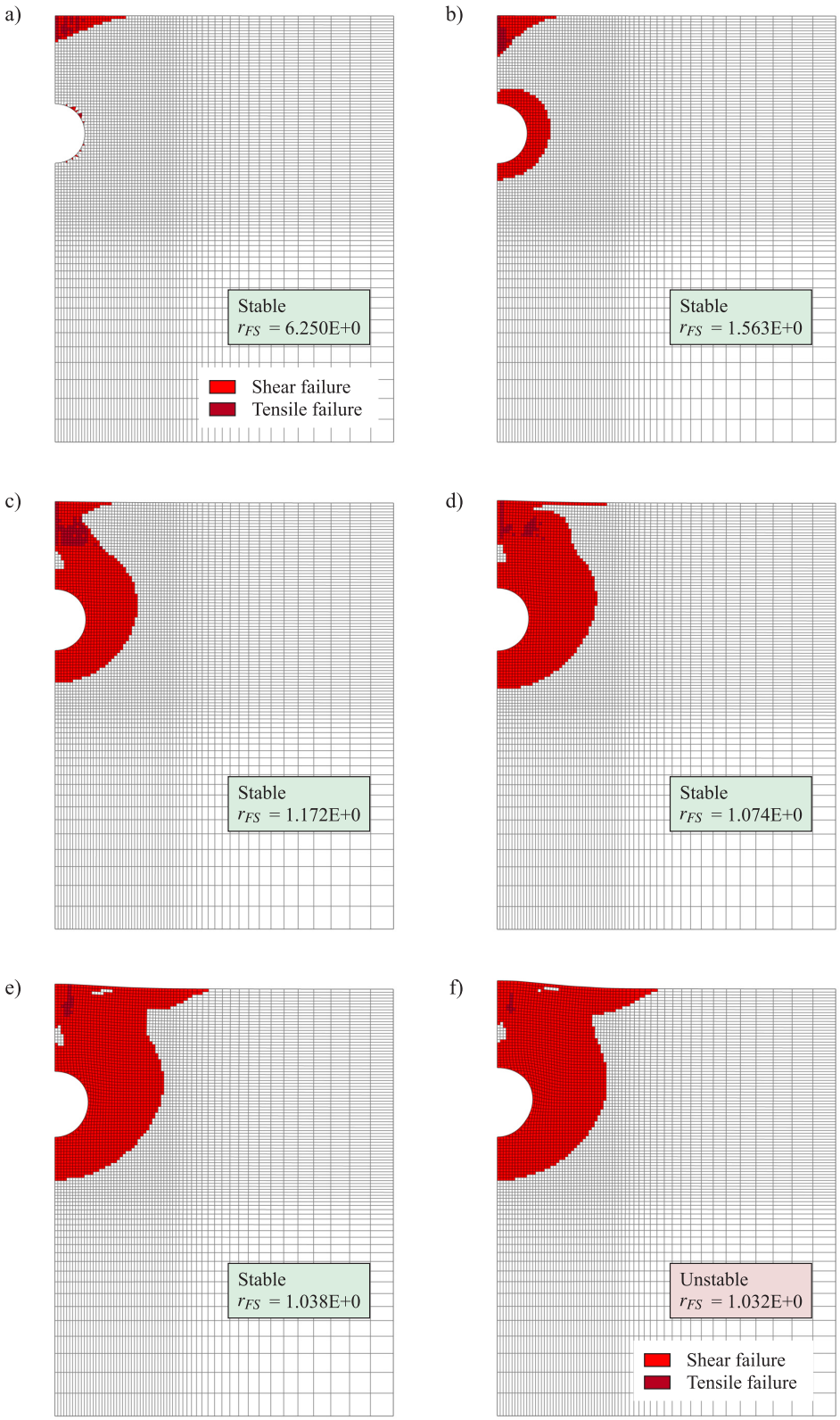

Figure 29. Representation similar to that in Figure 25 for cylindrical *expanding* cavity (the sequence represented in the figure corresponds to Case 4c in Table 3).

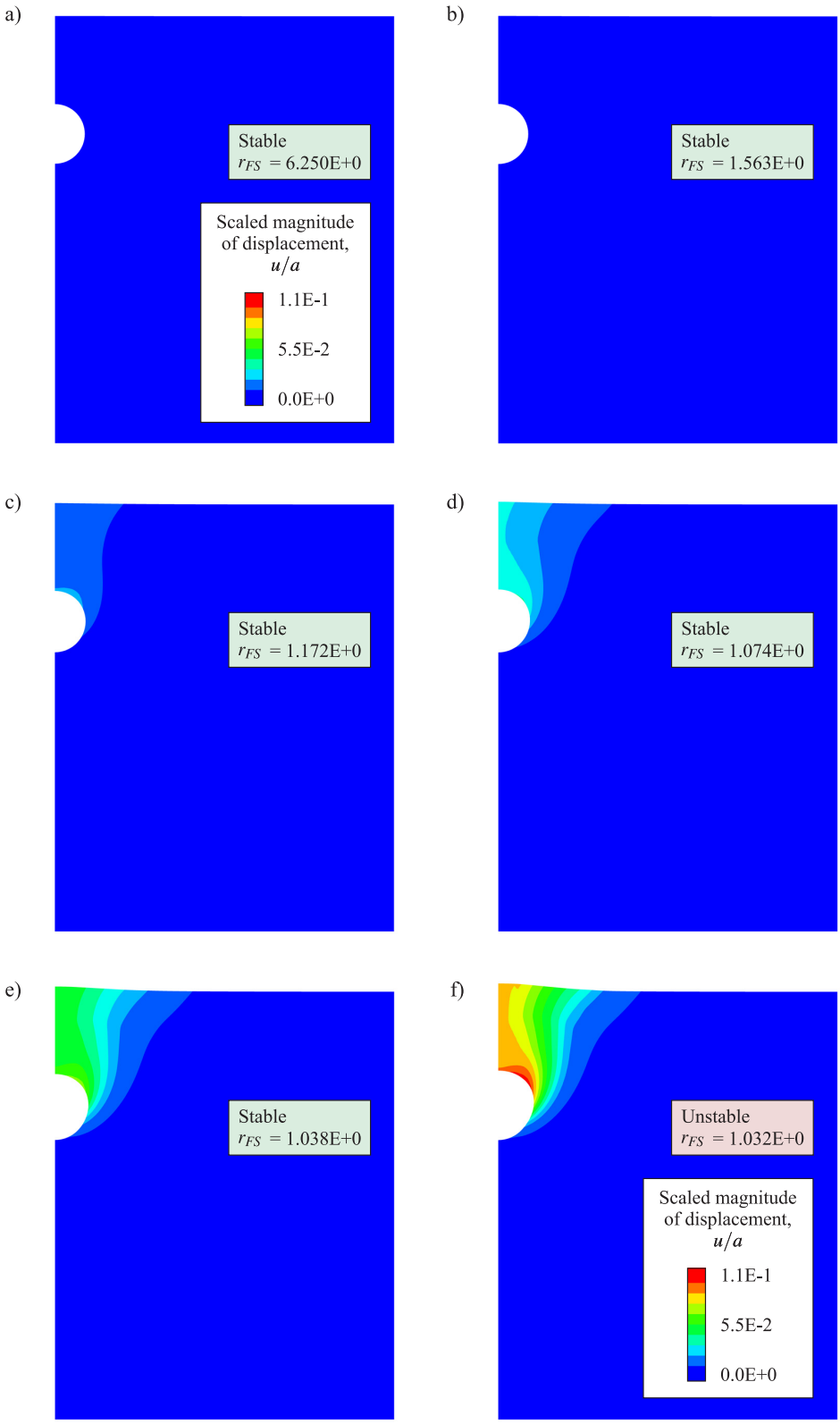

Figure 30. Representation of contours of magnitude of displacements for the same sequence of numerical models shown in Figure 29.

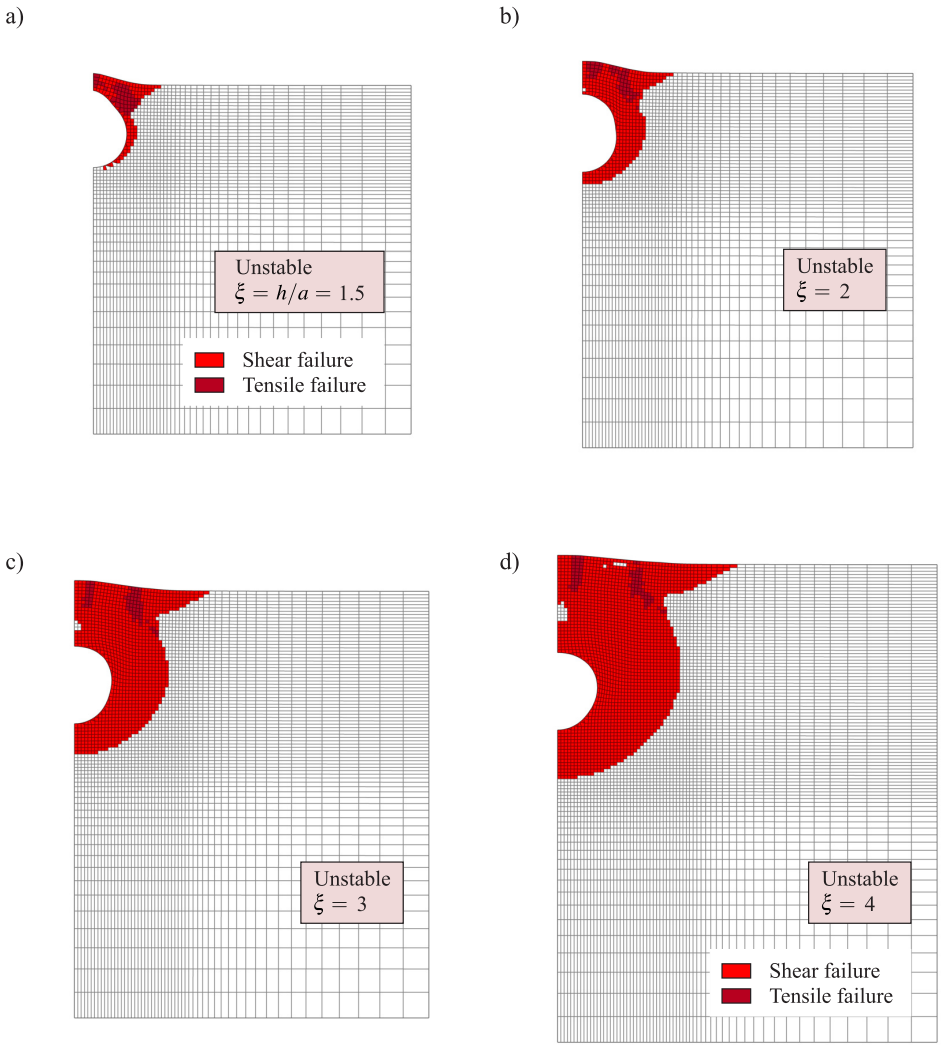

Figure 31. First unstable situation in the computation of factor of safety with numerical models for cylindrical *expanding* cavities at various scaled depths, ξ, corresponding values a) 1.5; b) 2; c) 3; and d) 4.

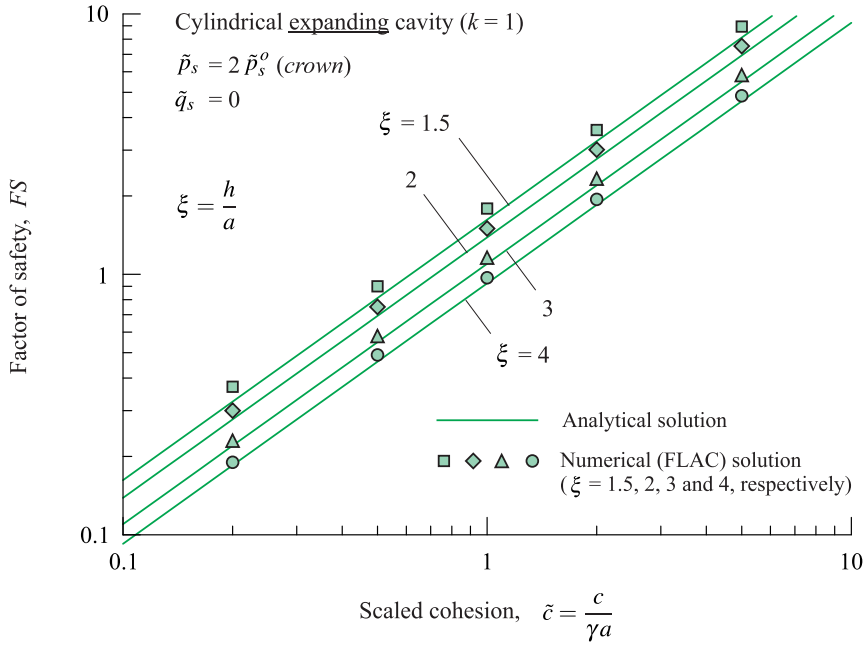

Figure 32. Graphical representation similar to that in Figure 21 showing the relationship between factor of safety and scaled ground cohesion for *expanding* cylindrical cavities at different scaled depths. The symbols in the diagram represent the factors of safety obtained with the numerical models.

Table 3. Summary of input data and results for different cases of cylindrical *expanding* cavities in cohesive ground solved with the numerical models (see Figure 32).

Case	ξ [-]	$\tilde{c}$ [-]	a [m]	h [m]	γ [kN/m^3]	c [kPa]	p_s [kPa]	FS_A [-]	FS_N [-]	$f_{FS}^{A\text{-}N}$ [-]
1a	1.5	0.2	4.4	6.6	17.4	15.312	76.56	0.324	0.37	0.88
1b	1.5	0.5	3.6	5.4	15.7	28.260	56.52	0.811	0.90	0.90
1c	1.5	1.0	4.4	6.6	24.0	105.600	105.60	1.622	1.79	0.90
1d	1.5	2.0	1.4	2.1	21.2	59.360	29.68	3.244	3.58	0.91
1e	1.5	5.0	2.3	3.5	17.0	195.500	39.10	8.109	8.95	0.91
2a	2.0	0.2	4.6	9.2	21.2	19.504	195.04	0.277	0.30	0.92
2b	2.0	0.5	1.9	3.8	24.3	23.085	92.34	0.693	0.75	0.92
2c	2.0	1.0	2.6	5.2	21.5	55.900	111.80	1.386	1.50	0.92
2d	2.0	2.0	3.5	7.0	20.8	145.600	145.60	2.773	3.01	0.92
2e	2.0	5.0	2.8	5.6	16.2	226.800	90.72	6.931	7.52	0.92
3a	3.0	0.2	3.9	11.7	24.2	18.876	377.52	0.220	0.23	0.96
3b	3.0	0.5	3.7	11.1	15.9	29.415	235.32	0.549	0.58	0.95
3c	3.0	1.0	2.3	6.9	15.0	34.500	138.00	1.099	1.16	0.95
3d	3.0	2.0	2.2	6.6	21.7	95.480	190.96	2.197	2.33	0.94
3e	3.0	5.0	1.4	4.2	20.5	143.500	114.80	5.493	5.82	0.94
4a	4.0	0.2	1.3	5.2	22.0	5.720	171.60	0.185	0.19	0.97
4b	4.0	0.5	3.6	14.4	19.9	35.820	429.84	0.462	0.49	0.94
4c	4.0	1.0	1.4	5.6	20.0	28.000	168.00	0.924	0.97	0.95
4d	4.0	2.0	1.9	7.6	20.1	76.380	229.14	1.848	1.94	0.95
4e	4.0	5.0	4.7	18.8	22.3	524.050	628.86	4.621	4.85	0.95

Results summarized in this table consider a scaled internal pressure at the *crown*, $\tilde{p}_s = p_s/(\gamma a) = 2\,\tilde{p}_s^o$ and a scaled ground surcharge load, $\tilde{q}_s = 0$. The columns labelled as FS_A and FS_N correspond to the numerator and denominator of equation (31), respectively.

5. Comparison of results obtained from limit equilibrium (Terzaghi's) type models

As discussed in Section 2, limit equilibrium methods are still popular methods for analysis of stability of cavities in the practice of geotechnical engineering, including cases of *expanding* cavities for gas storage and CAES applications (see, for example, Figure 7). This section presents a comparison of results obtained with the statically admissible model discussed in Section 3, and with Terzaghi's limit equilibrium models.

Appendix C presents a demonstration of the equations needed to compute the required internal pressure at the *crown* of the (assumed flat) roof of *contracting* and *expanding* cavities to which a cavity of circular shape is circumscribed. Below, only the main equations are transcribed from the appendix.

The case of *contracting* cavities is considered first.

Figure 33 represents the same model proposed by Terzaghi (see Figure 5), when the material is frictionless (i.e., the ground is purely cohesive as in the model presented in Section 3) and when the same notation for variables as in the model in Figure 3 is used. For a *contracting* cavity at a limit state of equilibrium in a ground with scaled critical cohesion, $\tilde{c}_{cr}$, considering that the variables are scaled according to the same rules introduced by equations (6) through (8), the scaled pressure acting on the *crown* of a circular cavity circumscribed to a flat roof (as in Figure 33) becomes (see Appendix C for details)

$$\tilde{p}_s = \tilde{q}_s + (\xi - 1)\left(1 - \frac{k}{3}\tilde{c}_{cr}\right) \tag{32}$$

In equation (32), similarly as in the equations presented in Sections 3.2 and 3.3, the parameter k distinguishes the cases of cylindrical and spherical cavities, for values equal to 1 and 2, respectively.

Introducing the same definition of factor of safety as in equation (20), the factor of safety for the circular *contracting* cavity based on the Terzaghi's limit equilibrium model becomes

$$FS = \frac{1}{3}\frac{k\tilde{c}(\xi - 1)}{\tilde{q}_s - \tilde{p}_s + \xi - 1} \tag{33}$$

When the internal pressure is expressed as a factor of the *in-situ* vertical stress at the *crown* level according to equation (22) (see also equations 10 and 11), equation (33) is written as follows

$$FS = \frac{1}{3}\frac{k\tilde{c}(\xi - 1)}{(1 - f_{\tilde{p}s})(\tilde{q}_s + \xi - 1)} \tag{34}$$

The ratio of factors of safety for the proposed analytical model and the limit equilibrium model, $f_{FS}^{A\text{-}T}$, is introduced as follows

$$f_{FS}^{A\text{-}T} = \frac{FS\ [\text{Proposed Analytical Model}]}{FS\ [\text{Limit Equilibrium Model}]} \tag{35}$$

Replacing equations (23) and (34) into equation (35), the ratio $f_{FS}^{A\text{-}T}$ becomes

$$f_{FS}^{A\text{-}T} = \frac{6\ln\xi}{\xi - 1} \tag{36}$$

Note that in equation (36), all parameters other than the scaled depth, ξ, have cancelled out (including the parameter k), so the relationship given by equation (36) is valid for both cylindrical and spherical *contracting* cavities.

Figure 34 represents the relationship between the ratio of factors of safety, $f_{FS}^{A\text{-}T}$, and the scaled depth, ξ, for *contracting* cylindrical or spherical cavities according to equation (36). The horizontal line corresponding to the ordinate one, marks the limit between conservative predictions by the limit equilibrium model (ratios $f_{FS}^{A\text{-}T}$ larger than one) and non-conservative predictions by the limit equilibrium model (ratios $f_{FS}^{A\text{-}T}$ smaller than one). The curve in Figure 34 is shown to intersect the horizontal line of ordinate one at the abscissa $\sim$18.5. Therefore, Terzaghi's limit equilibrium model (Figure 33) predicts over conservative (too safe) values of factors of safety for shallow cavities when $\xi < \sim 18.5$ and non-conservative (unsafe) values of factors of safety for deeper cavities, when $\xi > \sim 18.5$.

Table 4 lists the resulting values of factors of safety and the ratios of factors of safety obtained with the proposed analytical model, the numerical (FLAC) model and with Terzaghi's model for the same cases of *contracting* cylindrical cavities listed in Table 2. The ratio $f_{FS}^{T\text{-}N}$ (right-most column in Table 4) corresponds to the ratio of

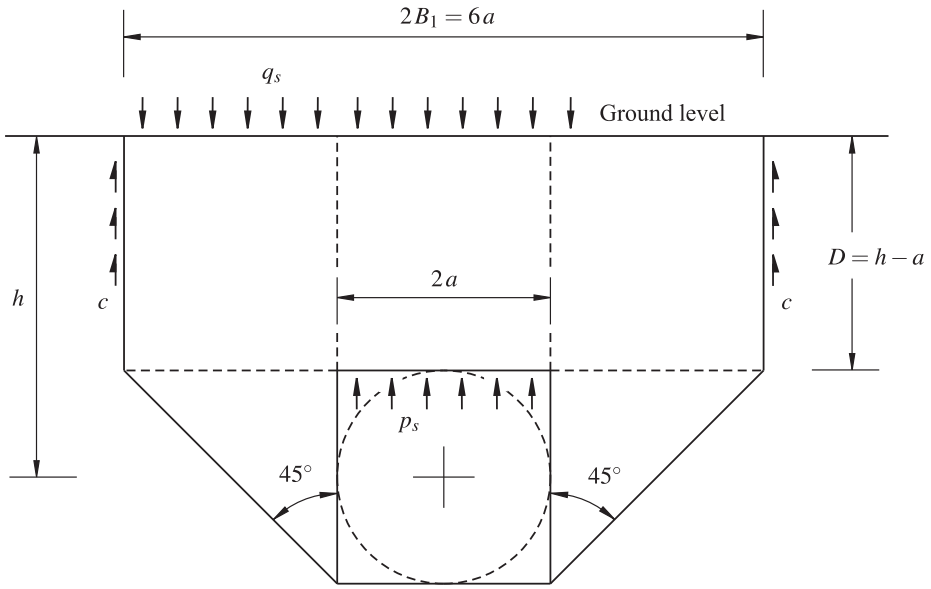

Figure 33. Limit equilibrium model by Terzaghi (1943) for a *contracting* opening in purely cohesive ground (See Figure 5).

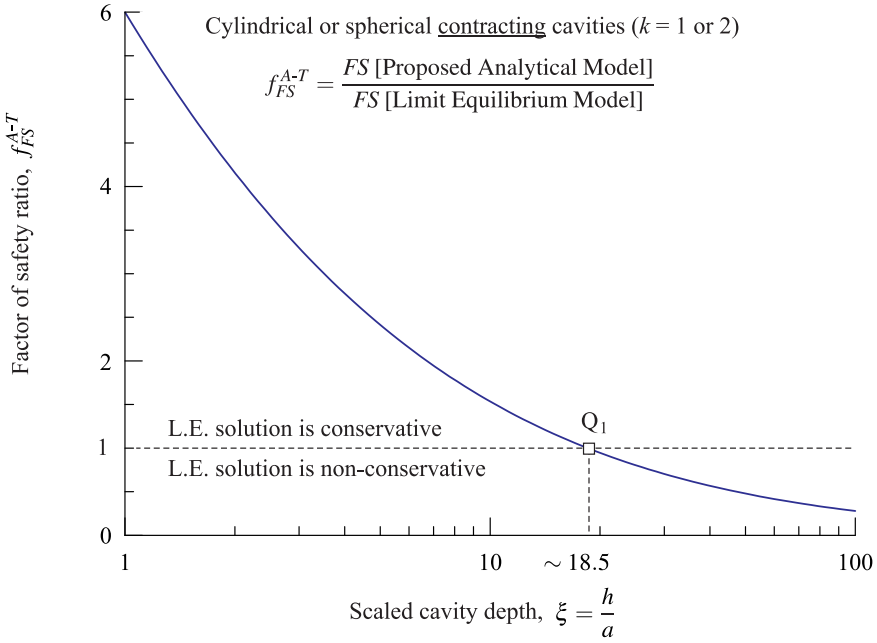

Figure 34. Relationship between the ratio of factors of safety obtained with the proposed analytical model and with Terzaghi's (limit equilibrium, L.E.) model, and the scaled depth of cylindrical or spherical *contracting* openings.

Table 4. Comparison of analytical (with proposed solution), numerical and limit equilibrium (Terzaghi's based) results for the same cases of *contracting* openings listed in Table 2.

Case	ξ [-]	$\tilde{c}$ [-]	FS_A [-]	FS_N [-]	FS_T [-]	$f_{FS}^{A\text{-}N}$ [-]	$f_{FS}^{T\text{-}N}$ [-]
1a	1.5	0.2	0.324	0.36	0.067	0.90	0.19
1b	1.5	0.5	0.811	0.89	0.167	0.91	0.19
1c	1.5	1.0	1.622	1.79	0.333	0.91	0.19
1d	1.5	2.0	3.244	3.57	0.667	0.91	0.19
1e	1.5	5.0	8.109	8.93	1.667	0.91	0.19
2a	2.0	0.2	0.277	0.30	0.067	0.92	0.22
2b	2.0	0.5	0.693	0.75	0.167	0.92	0.22
2c	2.0	1.0	1.386	1.50	0.333	0.92	0.22
2d	2.0	2.0	2.773	3.00	0.667	0.92	0.22
2e	2.0	5.0	6.931	7.50	1.667	0.92	0.22
3a	3.0	0.2	0.220	0.23	0.067	0.96	0.29
3b	3.0	0.5	0.549	0.58	0.167	0.95	0.29
3c	3.0	1.0	1.099	1.16	0.333	0.95	0.29
3d	3.0	2.0	2.197	2.32	0.667	0.95	0.29
3e	3.0	5.0	5.493	5.81	1.667	0.95	0.29
4a	4.0	0.2	0.185	0.19	0.067	0.97	0.35
4b	4.0	0.5	0.462	0.48	0.167	0.96	0.35
4c	4.0	1.0	0.924	0.97	0.333	0.95	0.34
4d	4.0	2.0	1.848	1.94	0.667	0.95	0.34
4e	4.0	5.0	4.621	4.84	1.667	0.95	0.34

The columns labelled as FS_A and FS_N correspond to the numerator and denominator of equation (31), respectively. The column labelled as FS_T corresponds to the denominator of equation (35) and the numerator of equation (37).

factors of safety obtained with the Terzaghi's model and with the numerical (FLAC) models, i.e.,

$$f_{FS}^{T\text{-}N} = \frac{FS\,[\text{Limit Equilibrium Model}]}{FS\,[\text{Numerical (FLAC) Model}]} \tag{37}$$

The ratios $f_{FS}^{T\text{-}N}$ listed in Table 4 indicate that factors of safety obtained with Terzaghi's model are in between 19% and 34% of the factors of safety obtained with the numerical solution (which as discussed in Section 4 can be considered to be close to the true factors of safety), for cavities with scaled depths varying between 1.5 and 4, respectively.

A similar analysis as above can be done for *expanding* cavities.

Figure 35 shows a similar limit equilibrium model as in Figure 7 but considering that the lateral boundaries of the wedge above the cavity are vertical (i.e., the angle α in Figure 7 is assumed to be zero). It can be shown that for a cavity at a limit state of equilibrium, the pressure needed to reach the limit state becomes minimum when the walls are assumed vertical (see, for example, Kim et al. 2012).

For an *expanding* cavity at a limit state of equilibrium in a ground with scaled critical cohesion, $\tilde{c}_{cr}$, considering that the variables are scaled according to the same rules introduced by equations (6) through (8), the scaled pressure acting on the *crown* of a circular cavity circumscribed to a flat roof becomes (see Appendix C for details)

$$\tilde{p}_s = \tilde{q}_s + (\xi - 1)\,(1 + k\,\tilde{c}_{cr}) \tag{38}$$

With the same definition of factor of safety as in equation (20), the factor of safety for the circular *expanding* cavity based on the Terzaghi's limit equilibrium model becomes

$$FS = -\frac{k\,\tilde{c}\,(\xi - 1)}{\tilde{q}_s - \tilde{p}_s + \xi - 1} \tag{39}$$

When the *crown* internal pressure is expressed as a factor of the *in-situ* vertical stress at the *crown* level accord-

ing to equations (10), (11) and (22), equation (39) is written as follows

$$FS = \frac{k\,\tilde{c}\,(\xi - 1)}{(f_{\tilde{p}s} - 1)\,(\tilde{q}_s + \xi - 1)} \tag{40}$$

Replacing equations (27) and (40) into equation (35), the ratio of factors of safety for the proposed analytical model and the limit equilibrium model, $f_{FS}^{A\text{-}T}$, becomes

$$f_{FS}^{A\text{-}T} = \frac{2\ln\xi}{\xi - 1} \tag{41}$$

Again, and as for the case of *contracting* cavities, equation (41) is valid for both cylindrical and spherical *expanding* cavities.

Figure 36 shows a similar representation as in Figure 34, this time for *expanding* cavities computed with equation (41). The horizontal line at ordinate one distinguishes again the cases of conservative and non-conservative predictions by the limit equilibrium model. Figure 36 shows that the Terzaghi's type limit equilibrium model predicts again over conservative (too safe) values of factors of safety for shallow cavities when $\xi < \sim 3.51$ and non-conservative (unsafe) values of factors of safety for deeper cavities when $\xi > \sim 3.51$ (note that for the case of *expanding* cavities, the limit between conservative and non-conservative predictions has decreased from ~ 18.5 to ~ 3.51). Table 5 lists similar information as Table 4, and shows that the ratio $f_{FS}^{T\text{-}N}$ varies between 54% and 103% for cavities with scaled depths varying between 1.5 and 4, respectively.

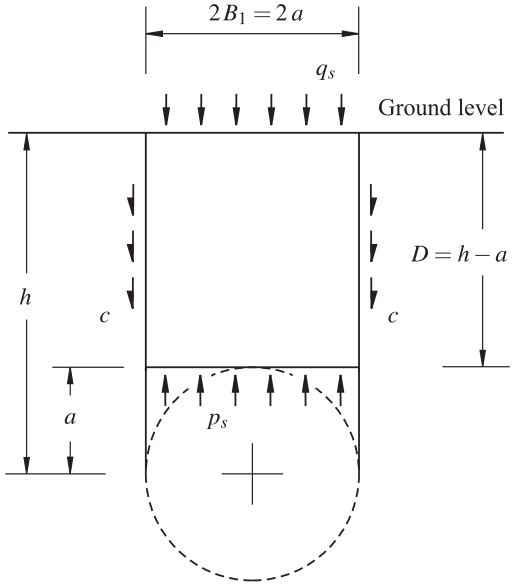

Figure 35. Limit equilibrium model for an *expanding* opening in purely cohesive ground derived from Figure 7. Note that the angle α in Figure 7 is considered to be zero; this leads to the most conservative condition of shear strength mobilized along the lateral boundaries of the detaching block.

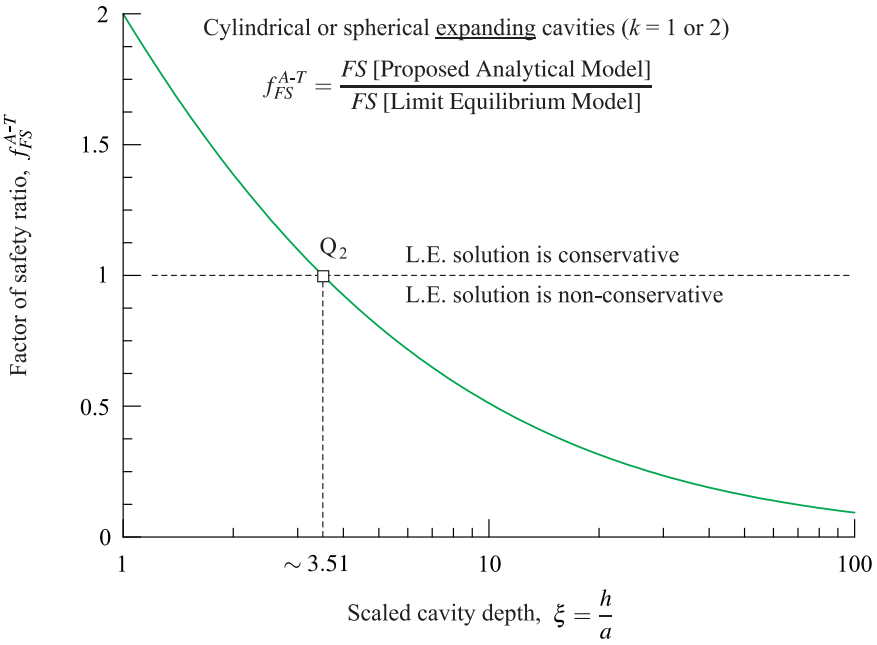

Figure 36. Relationship between the ratio of factors of safety obtained with the proposed analytical model and with Terzaghi's based limit equilibrium (L.E.) model and the scaled depth of cylindrical or spherical *expanding* openings.

Table 5. Comparison of analytical (with proposed solution), numerical and limit equilibrium (Terzaghi's based) results for the same cases of *expanding* openings listed in Table 3.

Case	ξ [-]	$\tilde{c}$ [-]	FS_A [-]	FS_N [-]	FS_T [-]	$f_{FS}^{A\text{-}N}$ [-]	$f_{FS}^{T\text{-}N}$ [-]
1a	1.5	0.2	0.324	0.37	0.200	0.88	0.54
1b	1.5	0.5	0.811	0.90	0.500	0.90	0.56
1c	1.5	1.0	1.622	1.79	1.000	0.90	0.56
1d	1.5	2.0	3.244	3.58	2.000	0.91	0.56
1e	1.5	5.0	8.109	8.95	5.000	0.91	0.56
2a	2.0	0.2	0.277	0.30	0.200	0.92	0.67
2b	2.0	0.5	0.693	0.75	0.500	0.92	0.67
2c	2.0	1.0	1.386	1.50	1.000	0.92	0.67
2d	2.0	2.0	2.773	3.01	2.000	0.92	0.66
2e	2.0	5.0	6.931	7.52	5.000	0.92	0.66
3a	3.0	0.2	0.220	0.23	0.200	0.96	0.87
3b	3.0	0.5	0.549	0.58	0.500	0.95	0.86
3c	3.0	1.0	1.099	1.16	1.000	0.95	0.86
3d	3.0	2.0	2.197	2.33	2.000	0.94	0.86
3e	3.0	5.0	5.493	5.82	5.000	0.94	0.86
4a	4.0	0.2	0.185	0.19	0.200	0.97	1.05
4b	4.0	0.5	0.462	0.49	0.500	0.94	1.02
4c	4.0	1.0	0.924	0.97	1.000	0.95	1.03
4d	4.0	2.0	1.848	1.94	2.000	0.95	1.03
4e	4.0	5.0	4.621	4.85	5.000	0.95	1.03

The columns labelled as FS_A and FS_N correspond to the numerator and denominator of equation (31), respectively. The column labelled as FS_T corresponds to the denominator of equation (35) and the numerator of equation (37).

6. Stability conditions for shallow cavities in cohesive-frictional ground

The stability analyses of shallow *contracting* and *expanding* openings presented in previous sections assumed the ground to be purely cohesive. This was done with the purpose of simplifying the analysis and to be able to reveal fundamental relationships governing the stability of shallow cavities.

This section presents the extension of the analytical solution presented earlier on for the case of Mohr-Coulomb cohesive-frictional ground, and a comparison of results obtained with the analytical solution and with the numerical (FLAC) solution.

Appendix D presents a detailed derivation of the equations conforming the analytical solution of *contracting* and *expanding* cavities in a ground that obeys the Mohr-Coulomb failure criterion. Below, only the main equations are transcribed from Appendix D.

The problem considered in this section is the same problem introduced in Section 3.1 (see Figure 14). It involves a *contracting* or *expanding* cylindrical or spherical cavity with scaled depth, ξ, for which the scaled internal pressure at the *crown* is $\tilde{p}_s^A$ (again, to be denoted simply as $\tilde{p}_s$) and the scaled ground surcharge load is $\tilde{q}_s$. The ground is assumed to obey the Mohr-Coulomb failure criterion, and to have a cohesion, c, (and a scaled cohesion, $\tilde{c}$, according to equation 7) and an internal friction angle, ϕ. The objective is to compute the factor of safety, *FS*, for the cavity for the given values of shear strength and loading.

For a material that obeys the Mohr-Coulomb failure criterion, the relationship between principal stresses, σ_1 and σ_3, at failure is written as follows (see, for example, Jaeger et al. 2007)

$$\sigma_1 = N_\phi \sigma_3 + \sigma_c \tag{42}$$

In equation (42), N_ϕ is the passive reaction coefficient, computed from the internal friction angle, ϕ, as

$$N_\phi = \frac{1+\sin\phi}{1-\sin\phi} \tag{43}$$

while σ_c is the uniaxial compressive strength, computed from the cohesion, c, and the passive reaction coefficient, N_ϕ, as

$$\sigma_c = 2\,c\sqrt{N_\phi} \tag{44}$$

With regard to equation (43), it should be noted that the tangent of the internal friction angle, ϕ, can be expressed in terms of the passive reaction coefficient, N_ϕ, as follows to

$$\tan\phi = \frac{N_\phi - 1}{2\sqrt{N_\phi}} \tag{45}$$

According to the *strength reduction technique* discussed in previous sections (see, for example, Figure 13), for the case of a cohesive-frictional material, the scaled critical cohesion and the tangent of the critical internal friction angle associated with the limit state of equilibrium are computed from the given values of cohesion and tangent of internal friction angle, and the factor of safety, *FS*, using the following equations, respectively

$$\tilde{c}_{cr} = \frac{\tilde{c}}{FS}; \qquad \tan\phi_{cr} = \frac{\tan\phi}{FS} \tag{46}$$

Note that in view of equation (46), the following equality holds between the ratio of given scaled cohesion and tangent of internal friction angle, and between the ratio of critical scaled cohesion and tangent of critical internal friction angle,

$$\frac{\tilde{c}}{\tan\phi} = \frac{\tilde{c}_{cr}}{\tan\phi_{cr}} \tag{47}$$

Also, in view of equation (45) and the (right-side) equation (46), the ratio of factor of safety and tangent of given internal friction angle can be written in terms of the critical passive reaction coefficient, N_ϕ^{cr}, as follows

$$\frac{FS}{\tan\phi} = \frac{2\sqrt{N_\phi^{cr}}}{N_\phi^{cr}-1} \tag{48}$$

For the case of *contracting* cavities, the coefficient N_ϕ^{cr} can be computed from the solution of the following

transcendental equation (see Appendix D for details)

$$\left(\tilde{q}_s + \frac{\tilde{c}}{\tan\phi}\right)\xi^{-k(N_\phi^{cr}-1)} + \frac{1}{1-k(N_\phi^{cr}-1)}\left[\xi^{1-k(N_\phi^{cr}-1)}-1\right] - \left(\tilde{p}_s + \frac{\tilde{c}}{\tan\phi}\right) = 0 \qquad (49)$$

Similarly, for the case of *expanding* cavities, the coefficient N_ϕ^{cr} can be computed from the solution of the following transcendental equation (again, see Appendix D for details)

$$\left(\tilde{q}_s + \frac{\tilde{c}}{\tan\phi}\right)\xi^{k(N_\phi^{cr}-1)/N_\phi^{cr}} + \frac{1}{1+k(N_\phi^{cr}-1)/N_\phi^{cr}}\left[\xi^{1+k(N_\phi^{cr}-1)/N_\phi^{cr}}-1\right] - \left(\tilde{p}_s + \frac{\tilde{c}}{\tan\phi}\right) = 0 \qquad (50)$$

As with the case of equations introduced in Section 3, in equations (49) and (50) the parameter k is such that $k = 1$ implies that the cavity is cylindrical, while $k = 2$ implies that the cavity is spherical.

Once the critical passive reaction coefficient, N_ϕ^{cr}, is computed with either equations (49) and (50), the normalized factor of safety, $FS/\tan\phi$, can be computed with equation (48). In view of equations (48), (49) and (50), dimensionless representations of normalized factor of safety, $FS/\tan\phi$, for the vertical axis, and scaled cohesion, $\tilde{c}/\tan\phi$, for the horizontal axis, can be produced for chosen values of scaled internal (*crown*) pressure, $\tilde{p}_s$; scaled ground surcharge load, $\tilde{q}_s$; and scaled cavity depth, ξ.

It should be noted that similar dimensionless representations of factor of safety have been proposed by other authors in the past for the case of slopes, from results obtained with limit equilibrium or lower and upper bound models (see, for example, Bell 1966; Hoek & Bray 1981; Michalowski 2002; Wyllie & Mah 2004). For the case of slopes, the dimensionless representations involve considering for the vertical axis the same normalized factor of safety, $FS/\tan\phi$, and for the horizontal axis the height of the slope multiplied by the unit weight of the ground and the tangent of internal friction angle divided by the cohesion; in the published dimensionless representations for slopes, different curves correspond to different inclination angles considered for the slope.

Figure 37 shows such dimensionless representation of stability for the case of *contracting* cylindrical cavities for the case $\tilde{p}_s = 0$ and $\tilde{q}_s = 0$. The different curves in the diagram represent different scaled depths, ξ. These curves have been computed using equations (49) and (50), together with equation (48). Comparison of Figures 37 and 17 (the latter corresponding to cohesionless ground) indicates that the same observations regarding increase of factor of safety with increase of shear strength, and decrease of factor of safety with increase of depth can be made. Also, for the case of cohesive-frictional ground, Figure 37 indicates that the relationship between predicted normalized factor of safety, $FS/\tan\phi$, and scaled shear strength is non-linear (when represented in logarithmic scale, done in Figures 37 and 17).

To evaluate the predictions of factor of safety with the proposed analytical solution for *contracting* cavities, a series of numerical finite-difference (FLAC) models were set up and computed using the *strength reduction technique*. The computation of factor of safety for the FLAC models was done using a similar procedure as explained in Section 4, this time decreasing (or increasing) not only the cohesion of the material but also the tangent of internal friction angle (see Figure 13a). The symbols in Figure 37 represent the results of normalized factor of safety obtained with the numerical models for scaled depths, $\xi = 2$ and 4, respectively. The relative position of the curves representing the analytical solution for *contracting* cavities with respect to the symbols, suggest that the analytical solution is more conservative for the case of cohesive-frictional ground, compared with the case of purely cohesive ground discussed in Section 4 (see Figure 17).

Table 6 lists the input data and results for 48 cases of cylindrical *contracting* openings solved with the software FLAC, and represented by the symbols in Figure 37. As mentioned above, the cases consider values of scaled depth, $\xi = 2$ and 4, and the values of scaled cohesion, $\tilde{c}/\tan\phi$, listed in the third column in Table 6, covering the range of values on the horizontal axis in Figure 37. For each of the values of scaled cohesion, cases of internal friction angle, $\phi = 15^\circ$, 30° and 45° are computed (see fourth column in Table 6). Table 6 shows that although the unscaled factor of safety is different for each of the 3 cases of internal friction angle (see column labelled as FS_N in Table 6), the factor of safety divided by the tangent of the internal friction angle results the same for each of the three cases of internal friction angle (see column labelled as $FS_N/\tan\phi$ in Table 6). This confirms the observation made above for the analytical solution with regard to the dependence of the ratio $FS/\tan\phi$ and the dimensionless variables $\tilde{c}/\tan\phi$, ξ, $\tilde{p}_s$ and $\tilde{q}_s$ (see equations 48, 49 and 50). The column labelled as $FS_A/\tan\phi$ in Table 6 represents the results obtained with equation (49) (together with equation 48). The column labelled as $f_{FS}^{A\text{-}N}$ in Table 6 represents the ratio of analytical and numerical results (see equation 31) and indicates that the underestimation of stability conditions by the proposed analytical solution ranges between 60 and 80%, a

quite large value compared with the 10% underestimation for the case of purely cohesive ground described in Section 4 (see last column in Table 2).

The significant underestimation of factor of safety for the case of cohesive ground is suspected to be associated with the way in which the failure zone around and above the cavity propagates towards the ground surface to lead to the collapse mechanism. Figure 38 is similar to Figure 25 and shows a sequence of evolution of plastic failure for Case 2f-30 in Table 6. Also, Figure 39 is similar to Figure 26 and shows contours of magnitude of displacements corresponding to the models shown in Figure 38. Comparing Figures 38 and 25 (and Figures 39 and 26), for purely cohesive ground and cohesive-frictional ground, respectively, it is seen that for cohesive-frictional ground (Figures 38 and 39), the failure zone tends to propagate mostly upwards towards the ground surface, and does not seem to extend significantly towards the lateral and lower regions of the opening. The proposed analytical solution for cohesive-frictional ground, nevertheless, assumes a circular area of integration around the cavity, in which re-distributed hoop and radial stresses are principal stresses (see Appendix D); in view of the way in which the failed region propagates, this assumption possibly does not reflect the condition of redistributed stresses around the opening and this leads to the significant underestimation of stability conditions —i.e., although the proposed analytical solution is a lower bound solution, it does not reflect well the mechanics of collapse.

A similar comparison of analytical and numerical results as discussed above for cylindrical *contracting* cavities is also carried out for cylindrical *expanding* cavities. Figures 40, 41 and 42 and Table 7 are equivalent to Figures 37, 38, 39 and Table 6, respectively, this time for *expanding* cavities and for a value of *crown* internal pressure equal to one and-a-half times the value of *in-situ* vertical stress at the level of the *crown* (i.e., $\tilde{p}_s = 1.5\,\tilde{p}_s^o$), with all other parameters being the same as for the case of *contracting* cavities discussed earlier on.

For the case of *expanding* cavities, the underestimation of stability conditions by the analytical solution given by equation (50) together with equation 48) results even more significant. The reason is suspected to be associated with the prediction of tensile hoop stresses inside the integration circle, in the vicinity of the ground surface, by the analytical solution, which deviates from the prediction by the numerical finite-difference (FLAC) models, which consider null tensile strength for the material (this particular consideration, which was discussed in Section 3.4 for the case of *expanding* cavities in cohesive materials, also applies to the analytical solution for the case of *expanding* cavities in cohesive-frictional materials discussed in this section).

Although the analytical solution for cohesive-frictional ground presented in this section does seem to lead to good predictions of stability conditions, it provides the framework to show how the factor of factor of safety can be conveniently scaled and expressed in terms of other dimensionless variables, to allow to produce similar dimensionless representations of (normalized) factor of safety, as published before by other authors for the case of slopes.

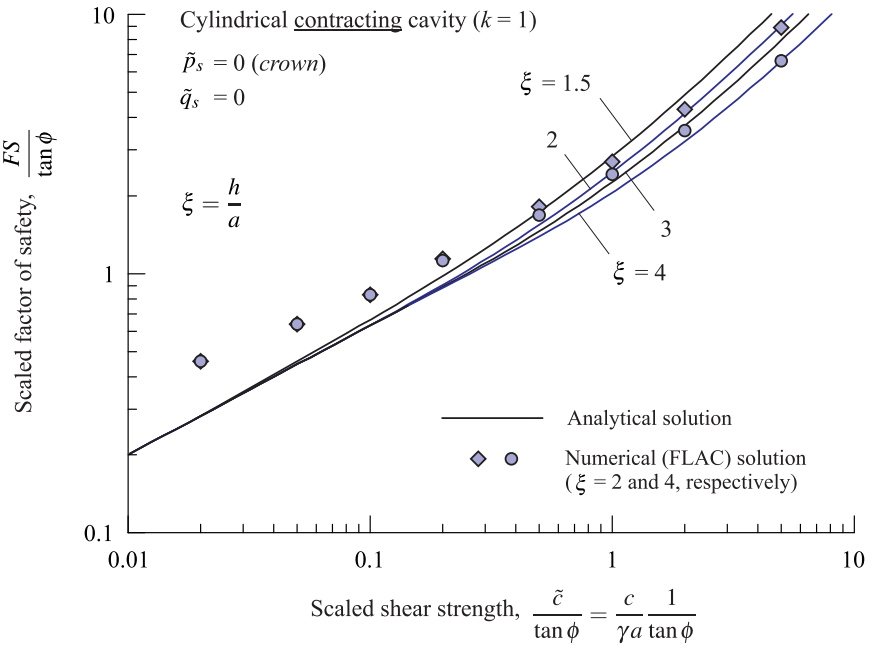

Figure 37. Graphical representation of the relationship between scaled factor of safety and scaled ground cohesion for *contracting* cylindrical cavities at different scaled depths in cohesive-frictional ground. The symbols in the diagram represent the factors of safety obtained with the numerical (FLAC) models.

Table 6. Summary of input data and results for different cases of cylindrical *contracting* cavities in cohesive-frictional ground solved with numerical (FLAC) models, represented in Figure 37.

Case	ξ [-]	$\tilde{c}/\tan\phi$ [-]	ϕ [°]	a [m]	h [m]	γ [kN/m^3]	c [kPa]	p_s [kPa]	FS_N [-]	$FS_A/\tan\phi$ [-]	$FS_N/\tan\phi$ [-]	$f_{FS}^{A\text{-}N}$ [-]
1a-15	2.0	0.02	15	1.0	2.0	15.1	0.081	0.00	0.123	0.283	0.46	0.62
1a-30	2.0	0.02	30	2.8	5.6	24.3	0.786	0.00	0.266	0.283	0.46	0.62
1a-45	2.0	0.02	45	1.0	2.0	21.2	0.424	0.00	0.460	0.283	0.46	0.62
1b-15	2.0	0.05	15	1.8	3.6	15.8	0.381	0.00	0.171	0.447	0.64	0.70
1b-30	2.0	0.05	30	1.2	2.4	23.4	0.811	0.00	0.370	0.447	0.64	0.70
1b-45	2.0	0.05	45	2.1	4.2	22.8	2.394	0.00	0.640	0.447	0.64	0.70
1c-15	2.0	0.10	15	3.3	6.6	25.9	2.290	0.00	0.222	0.630	0.83	0.76
1c-30	2.0	0.10	30	4.1	8.2	26.0	6.155	0.00	0.479	0.630	0.83	0.76
1c-45	2.0	0.10	45	3.4	6.8	20.9	7.106	0.00	0.830	0.630	0.83	0.76
1d-15	2.0	0.20	15	2.4	4.8	15.4	1.981	0.00	0.305	0.889	1.14	0.78
1d-30	2.0	0.20	30	3.1	6.2	21.3	7.624	0.00	0.658	0.889	1.14	0.78
1d-45	2.0	0.20	45	4.4	8.8	15.8	13.904	0.00	1.140	0.889	1.14	0.78
1e-15	2.0	0.50	15	4.3	8.6	14.1	8.123	0.00	0.485	1.457	1.81	0.81
1e-30	2.0	0.50	30	4.5	9.0	17.2	22.343	0.00	1.045	1.457	1.81	0.81
1e-45	2.0	0.50	45	2.9	5.8	19.1	27.695	0.00	1.810	1.457	1.81	0.81
1f-15	2.0	1.00	15	1.7	3.4	20.4	9.292	0.00	0.723	2.252	2.70	0.83
1f-30	2.0	1.00	30	4.8	9.6	24.1	66.788	0.00	1.559	2.252	2.70	0.83
1f-45	2.0	1.00	45	4.0	8.0	20.2	80.800	0.00	2.700	2.252	2.70	0.83
1g-15	2.0	2.00	15	3.8	7.6	21.2	43.172	0.00	1.155	3.719	4.31	0.86
1g-30	2.0	2.00	30	3.2	6.4	18.5	68.358	0.00	2.488	3.719	4.31	0.86
1g-45	2.0	2.00	45	2.8	5.6	23.0	128.800	0.00	4.310	3.719	4.31	0.86
1h-15	2.0	5.00	15	2.2	4.4	16.0	47.159	0.00	2.390	7.948	8.92	0.89
1h-30	2.0	5.00	30	2.8	5.6	22.1	178.632	0.00	5.150	7.948	8.92	0.89
1h-45	2.0	5.00	45	4.0	8.0	16.0	320.000	0.00	8.920	7.948	8.92	0.89
2a-15	4.0	0.02	15	1.0	4.0	15.1	0.081	0.00	0.123	0.283	0.46	0.59
2a-30	4.0	0.02	30	2.8	11.2	24.3	0.786	0.00	0.266	0.283	0.46	0.59
2a-45	4.0	0.02	45	1.0	4.0	21.2	0.424	0.00	0.460	0.283	0.46	0.59
2b-15	4.0	0.05	15	1.8	7.2	15.8	0.381	0.00	0.171	0.447	0.64	0.75
2b-30	4.0	0.05	30	1.2	4.8	23.4	0.811	0.00	0.370	0.447	0.64	0.75
2b-45	4.0	0.05	45	2.1	8.4	22.8	2.394	0.00	0.640	0.447	0.64	0.75
2c-15	4.0	0.10	15	3.3	13.2	25.9	2.290	0.00	0.222	0.630	0.83	0.76
2c-30	4.0	0.10	30	4.1	16.4	26.0	6.155	0.00	0.479	0.630	0.83	0.76
2c-45	4.0	0.10	45	3.4	13.6	20.9	7.106	0.00	0.830	0.630	0.83	0.76
2d-15	4.0	0.20	15	2.4	9.6	15.4	1.981	0.00	0.303	0.882	1.13	0.78
2d-30	4.0	0.20	30	3.1	12.4	21.3	7.624	0.00	0.652	0.882	1.13	0.78
2d-45	4.0	0.20	45	4.4	17.6	15.8	13.904	0.00	1.130	0.882	1.13	0.78
2e-15	4.0	0.50	15	4.3	17.2	14.1	8.123	0.00	0.466	1.365	1.74	0.79
2e-30	4.0	0.50	30	4.5	18.0	17.2	22.343	0.00	0.970	1.365	1.68	0.81
2e-45	4.0	0.50	45	2.9	11.6	19.1	27.695	0.00	1.680	1.365	1.68	0.81
2f-15	4.0	1.00	15	1.7	6.8	20.4	9.292	0.00	0.648	1.955	2.42	0.81
2f-30	4.0	1.00	30	4.8	19.2	24.1	66.788	0.00	1.397	1.955	2.42	0.81
2f-45	4.0	1.00	45	4.0	16.0	20.2	80.800	0.00	2.420	1.955	2.42	0.81
2g-15	4.0	2.00	15	3.8	15.2	21.2	43.172	0.00	0.954	2.978	3.56	0.84
2g-30	4.0	2.00	30	3.2	12.8	18.5	68.358	0.00	2.055	2.978	3.56	0.84
2g-45	4.0	2.00	45	2.8	11.2	23.0	128.800	0.00	3.560	2.978	3.56	0.84
2h-15	4.0	5.00	15	2.2	8.8	16.0	47.159	0.00	1.779	5.841	6.64	0.88
2h-30	4.0	5.00	30	2.8	11.2	22.1	178.632	0.00	3.834	5.841	6.64	0.88
2h-45	4.0	5.00	45	4.0	16.0	16.0	320.000	0.00	6.640	5.841	6.64	0.88

Results summarized in this table consider a scaled internal pressure at the *crown*, $\tilde{p}_s = p_s/(\gamma a) = 0$ and a scaled ground surcharge load, $\tilde{q}_s = 0$. The columns labelled as FS_A and FS_N correspond to the numerator and denominator of equation (31), respectively.

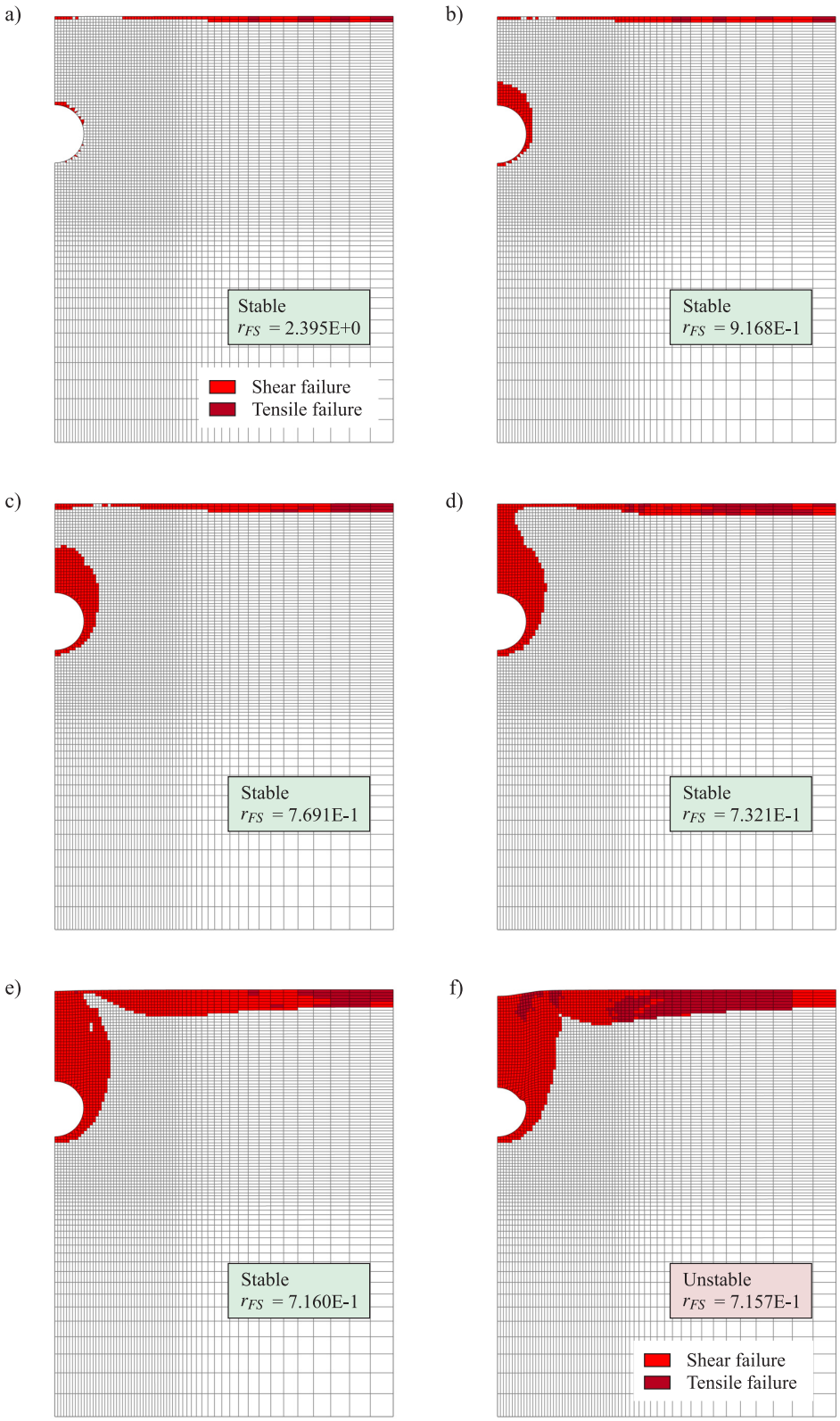

Figure 38. Sample sequence of computation of factor of safety for a cylindrical *contracting* cavity in cohesive-frictional ground, using the *strength reduction technique* in numerical (FLAC) models. The colored areas around the cavity and on the ground surface represent elements in the mesh that undergo plastic failure, in tension or compression. Plots a) through e) correspond to stable cavities, while plot f) corresponds to the first unstable situation (the sequence represented in the figure corresponds to Case 2f-30 in Table 6).

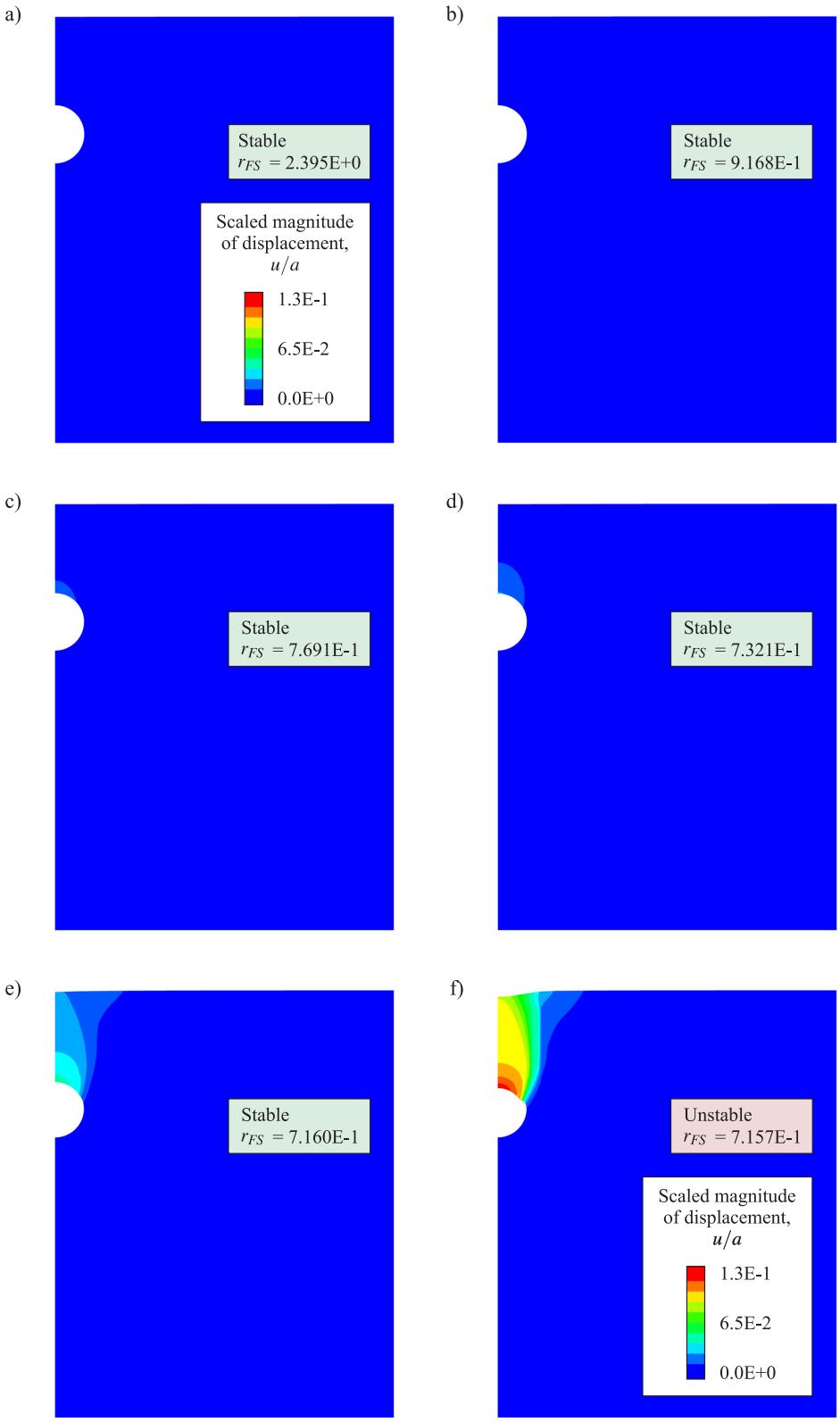

Figure 39. Representation of contours of magnitude of displacements for the same sequence of numerical (FLAC) models shown in Figure 38.

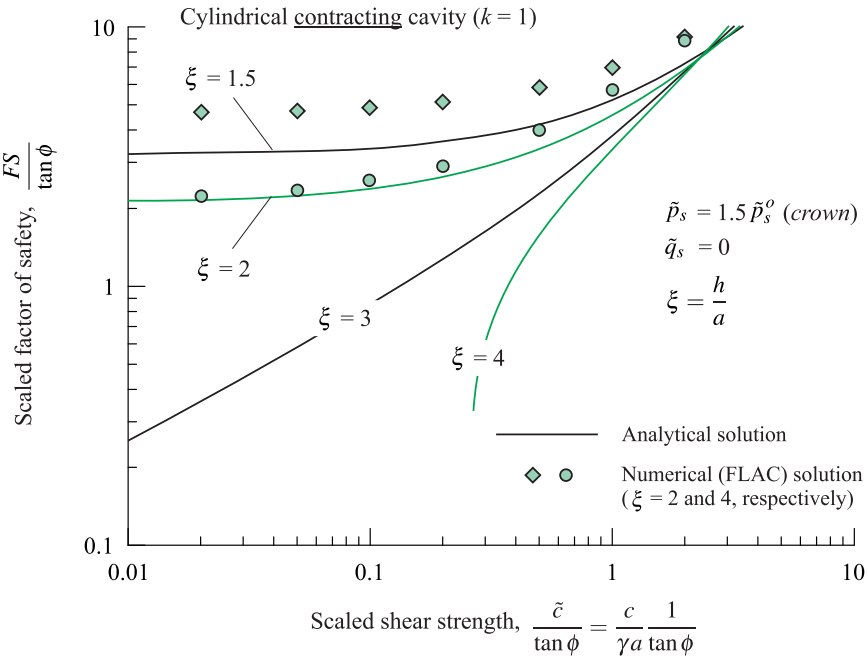

Figure 40. Graphical representation of the relationship between scaled factor of safety and scaled ground cohesion for *expanding* cylindrical cavities at different scaled depths in cohesive-frictional ground. The symbols in the diagram represent the factors of safety obtained with the numerical (FLAC) models.

Table 7. Summary of input data and results for different cases of cylindrical *expanding* cavities in cohesive-frictional ground solved with numerical (FLAC) models, represented in Figure 40.

Case	ξ [-]	$\tilde{c}/\tan\phi$ [-]	ϕ [°]	a [m]	h [m]	γ [kN/m^3]	c [kPa]	p_s [kPa]	FS_N [-]	$FS_A/\tan\phi$ [-]	$FS_N/\tan\phi$ [-]	$f_{FS}^{A\text{-}N}$ [-]
1a-15	2.0	0.02	15	1.0	2.0	15.1	0.081	30.20	0.592	0.359	2.21	0.16
1a-30	2.0	0.02	30	2.8	5.6	24.3	0.786	136.08	1.276	0.359	2.21	0.16
1a-45	2.0	0.02	45	1.0	2.0	21.2	0.424	42.40	2.210	0.359	2.21	0.16
1b-15	2.0	0.05	15	1.8	3.6	15.8	0.381	56.88	0.624	0.579	2.33	0.25
1b-30	2.0	0.05	30	1.2	2.4	23.4	0.811	56.16	1.345	0.579	2.33	0.25
1b-45	2.0	0.05	45	2.1	4.2	22.8	2.394	95.76	2.330	0.579	2.33	0.25
1c-15	2.0	0.10	15	3.3	6.6	25.9	2.290	170.94	0.678	0.844	2.53	0.33
1c-30	2.0	0.10	30	4.1	8.2	26.0	6.155	213.20	1.461	0.844	2.53	0.33
1c-45	2.0	0.10	45	3.4	6.8	20.9	7.106	142.12	2.530	0.844	2.53	0.33
1d-15	2.0	0.20	15	2.4	4.8	15.4	1.981	73.92	0.774	1.262	2.89	0.44
1d-30	2.0	0.20	30	3.1	6.2	21.3	7.624	132.06	1.669	1.262	2.89	0.44
1d-45	2.0	0.20	45	4.4	8.8	15.8	13.904	139.04	2.890	1.262	2.89	0.44
1e-15	2.0	0.50	15	4.3	8.6	14.1	8.123	121.26	1.064	2.278	3.97	0.57
1e-30	2.0	0.50	30	4.5	9.0	17.2	22.343	154.80	2.292	2.278	3.97	0.57
1e-45	2.0	0.50	45	2.9	5.8	19.1	27.695	110.78	3.970	2.278	3.97	0.57
1f-15	2.0	1.00	15	1.7	3.4	20.4	9.292	69.36	1.517	3.784	5.66	0.67
1f-30	2.0	1.00	30	4.8	9.6	24.1	66.788	231.36	3.268	3.784	5.66	0.67
1f-45	2.0	1.00	45	4.0	8.0	20.2	80.800	161.60	5.660	3.784	5.66	0.67
1g-15	2.0	2.00	15	3.8	7.6	21.2	43.172	161.12	2.387	6.647	8.91	0.75
1g-30	2.0	2.00	30	3.2	6.4	18.5	68.358	118.40	5.144	6.647	8.91	0.75
1g-45	2.0	2.00	45	2.8	5.6	23.0	128.800	128.80	8.910	6.647	8.91	0.75
1h-15	2.0	5.00	15	2.2	4.4	16.0	47.159	70.40	4.920	15.038	18.36	0.82
1h-30	2.0	5.00	30	2.8	5.6	22.1	178.632	123.76	10.600	15.038	18.36	0.82
1h-45	2.0	5.00	45	4.0	8.0	16.0	320.000	128.00	18.360	15.038	18.36	0.82
2a-15	4.0	0.02	15	1.0	4.0	15.1	0.081	90.60	1.246	3.235	4.65	0.70
2a-30	4.0	0.02	30	2.8	11.2	24.3	0.786	408.24	2.685	3.235	4.65	0.70
2a-45	4.0	0.02	45	1.0	4.0	21.2	0.424	127.20	4.650	3.235	4.65	0.70
2b-15	4.0	0.05	15	1.8	7.2	15.8	0.381	170.64	1.265	3.300	4.72	0.70
2b-30	4.0	0.05	30	1.2	4.8	23.4	0.811	168.48	2.725	3.300	4.72	0.70
2b-45	4.0	0.05	45	2.1	8.4	22.8	2.394	287.28	4.720	3.300	4.72	0.70
2c-15	4.0	0.10	15	3.3	13.2	25.9	2.290	512.82	1.297	3.406	4.84	0.70
2c-30	4.0	0.10	30	4.1	16.4	26.0	6.155	639.60	2.794	3.406	4.84	0.70
2c-45	4.0	0.10	45	3.4	13.6	20.9	7.106	426.36	4.840	3.406	4.84	0.70
2d-15	4.0	0.20	15	2.4	9.6	15.4	1.981	221.76	1.361	3.616	5.08	0.71
2d-30	4.0	0.20	30	3.1	12.4	21.3	7.624	396.18	2.933	3.616	5.08	0.71
2d-45	4.0	0.20	45	4.4	17.6	15.8	13.904	417.12	5.080	3.616	5.08	0.71
2e-15	4.0	0.50	15	4.3	17.2	14.1	8.123	363.78	1.549	4.235	5.78	0.73
2e-30	4.0	0.50	30	4.5	18.0	17.2	22.343	464.40	3.337	4.235	5.78	0.73
2e-45	4.0	0.50	45	2.9	11.6	19.1	27.695	332.34	5.780	4.235	5.78	0.73
2f-15	4.0	1.00	15	1.7	6.8	20.4	9.292	208.08	1.849	5.235	6.90	0.76
2f-30	4.0	1.00	30	4.8	19.2	24.1	66.788	694.08	3.984	5.235	6.90	0.76
2f-45	4.0	1.00	45	4.0	16.0	20.2	80.800	484.80	6.900	5.235	6.90	0.76
2g-15	4.0	2.00	15	3.8	15.2	21.2	43.172	483.36	2.422	7.178	9.04	0.79
2g-30	4.0	2.00	30	3.2	12.8	18.5	68.358	355.20	5.219	7.178	9.04	0.79
2g-45	4.0	2.00	45	2.8	11.2	23.0	128.800	386.40	9.040	7.178	9.04	0.79
2h-15	4.0	5.00	15	2.2	8.8	16.0	47.159	211.20	4.067	12.847	15.18	0.85
2h-30	4.0	5.00	30	2.8	11.2	22.1	178.632	371.28	8.764	12.847	15.18	0.85
2h-45	4.0	5.00	45	4.0	16.0	16.0	320.000	384.00	15.180	12.847	15.18	0.85

Results summarized in this table consider a scaled internal pressure at the *crown*, $\tilde{p}_s = p_s/(\gamma a) = 1.5\,\tilde{p}_s^o$ and a scaled ground surcharge load, $\tilde{q}_s = 0$. The columns labelled as FS_A and FS_N correspond to the numerator and denominator of equation (31), respectively.

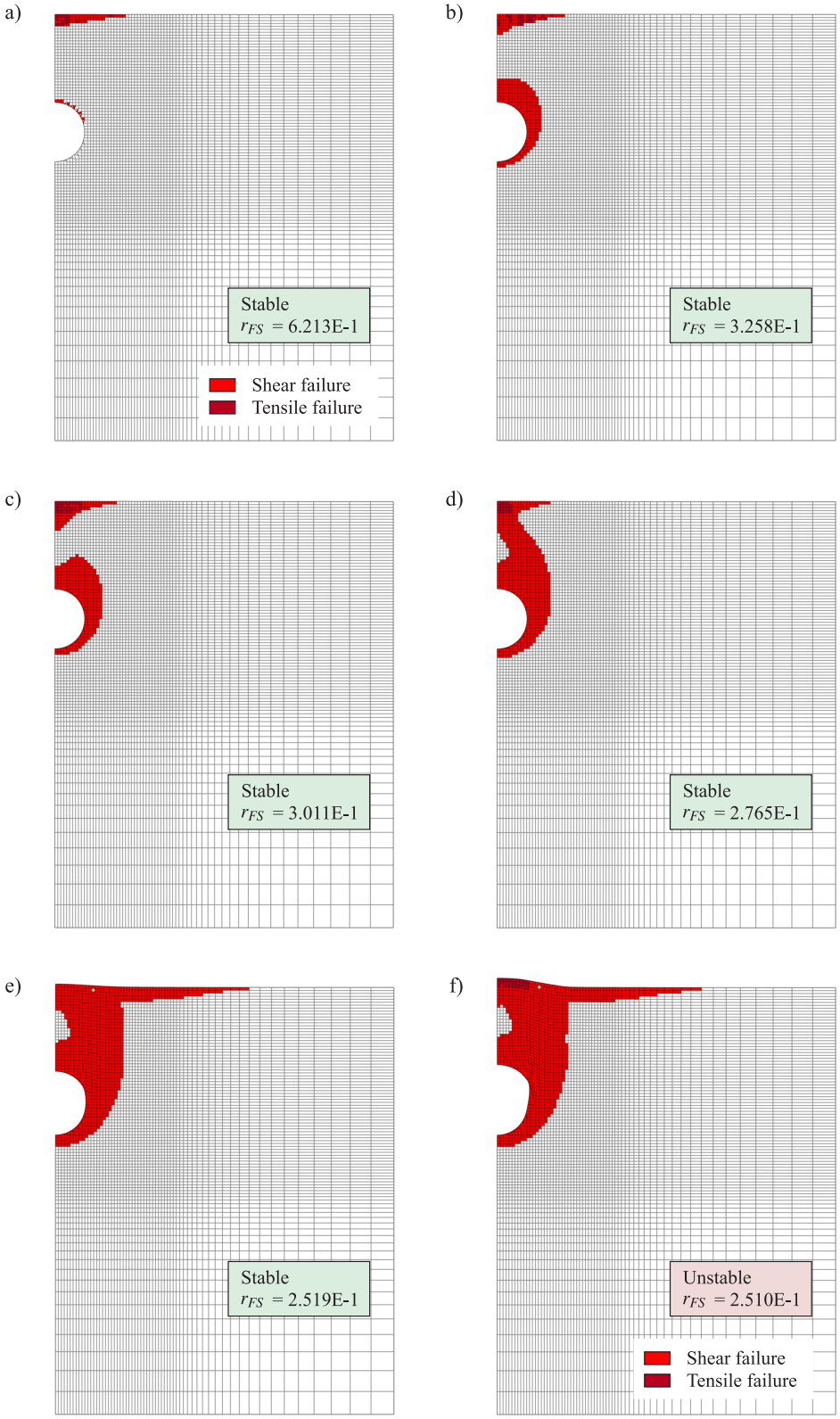

Figure 41. Representation similar to that in Figure 38 for cylindrical *expanding* cavity corresponding to Case 2f-30 in Table 7.

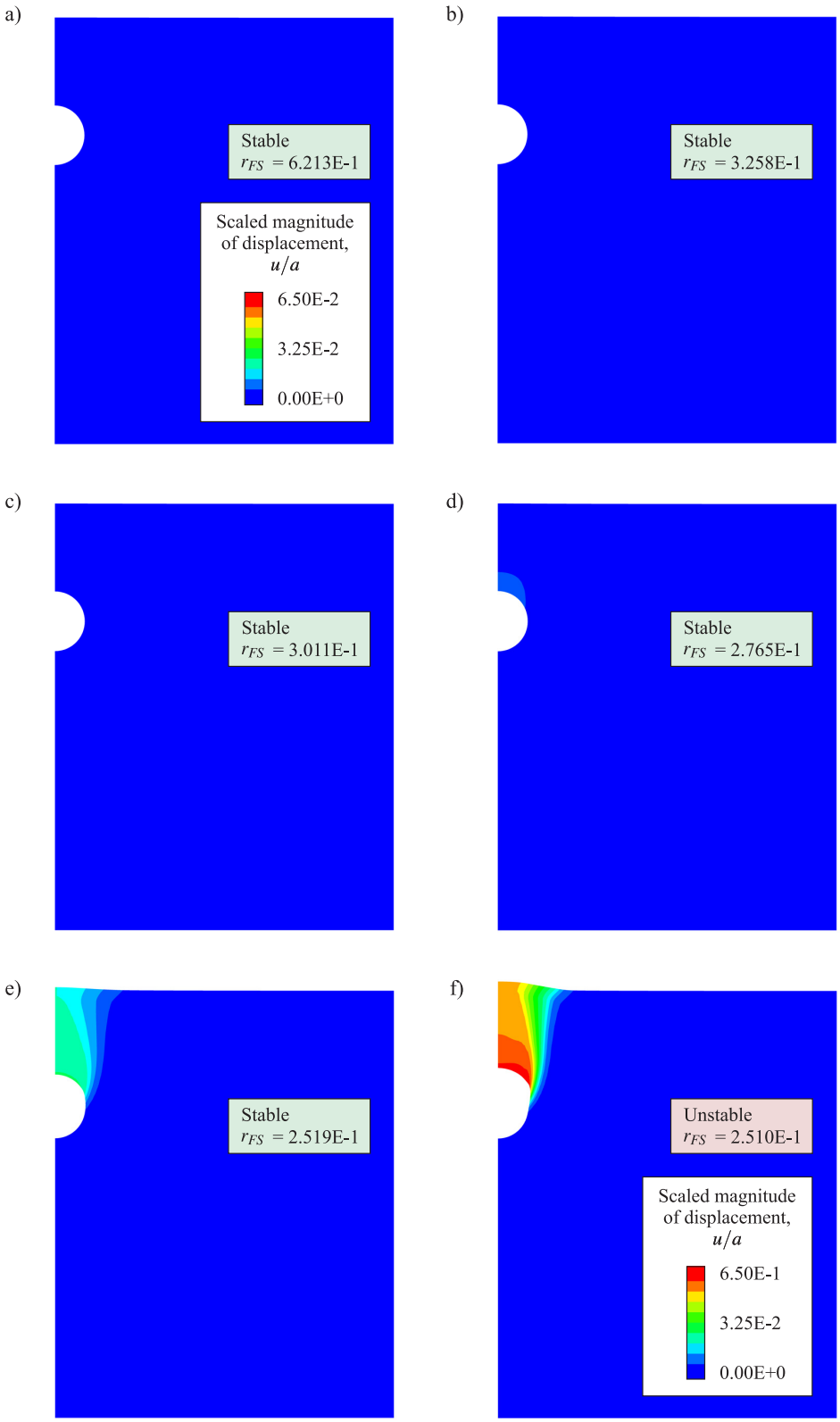

Figure 42. Representation of contours of magnitude of displacements for the same sequence of numerical (FLAC) models shown in Figure 41.

7. Final comments

Introduction of a scalar factor of safety for evaluation of stability conditions of shallow cavities, as done traditionally when evaluating stability of slopes, allows various relevant observations of theoretical-practical nature to be made with regard to stability of shallow cavities. For example, for the case of shallow cavities in cohesive ground, Sections 3.3 and 3.4 show that the factor of safety for a spherical cavity is twice the factor of safety for a section of long cylindrical tunnel of the same radius and depth, when all other (strength and loading) variables are the same. For the case of *contracting* cavities, Section 3.3 shows that the factor of safety decreases as the scaled depth of the cavity increases. This counterintuitive observation is explained by the fact that as the depth of the cavity increases, so do the magnitudes of stresses around the cavity that induce plastic failure, and eventually lead to development of a collapse mechanism. Also for the case of *contracting* cavities, the factor of safety increases when the *crown* internal pressure increases, with the factor of safety approaching infinite as the *crown* internal pressure tends to the *in-situ* reference pressure (the vertical *in-situ* stress at the *crown* level prior to excavation). For the case of *expanding* cavities, Section 3.4 shows that the opposite to the last observation holds: the factor of safety decreases when the *crown* internal pressure increases, with the factor of safety approaching to infinity as the *crown* internal pressure tends to the *in-situ* reference pressure. Also, for the case of *expanding* cavities, Section 3.4 shows that factor of safety corresponding to a *crown* internal pressure that is twice the value of the reference (*in-situ*) internal pressure, is the same as the factor of safety for a cavity with zero internal pressure. The observations above can assist in establishing stability conditions of existing mining works (e.g., drifts and shafts) when doing preliminary analyses of their suitability for air storage in CAES systems, which as discussed in Section 1, was the primary motivation for the developments reported in this paper.

In Section 4, by comparison of analytical results and numerical (FLAC) results obtained by application of the *strength reduction technique*, the proposed statically admissible solution for computing factors of safety for cavities in cohesive ground was shown to provide factors of safety that are reasonably conservative ('reasonably' meaning within 10% or less of the expected true factor of safety).

In Section 5, limit equilibrium (Terzaghi's type) solutions that are still popular for designing shallow cavities (in particular for *expanding* cavities for gas and air storage) have been shown to provide unreliable estimates of factors of safety, being conservative in some cases, and non-conservatives in others.

In Section 6, the analytical solution presented in Section 3 has been extended to consider the case of Mohr-Coulomb cohesive-frictional ground. By comparison of analytical results and numerical (FLAC) results obtained by application of the *strength reduction technique*, the analytical solution for computing factors of safety for cavities in cohesive-frictional ground is shown to give values of factors of safety that are significantly conservative. Despite the limitations of the proposed solution for cohesive-frictional ground, the analytical formulation shows that the factor of safety can be normalized with the tangent of the internal friction angle, and that this normalized factor of safety is a function of the scaled cohesion also normalized with the tangent of the internal friction angle, the scaled depth, scaled *crown* internal pressure and scaled ground surface surcharge load. This is a relevant observation that can be exploited to produce dimensionless representations of factors of safety for openings in ground satisfying the Mohr-Coulomb failure criterion, for example, using numerical models as done by other authors in the past with the case of slopes (Bell 1966; Hoek & Bray 1981; Michalowski 2002; Wyllie & Mah 2004).

The stability analyses for shallow *contracting* and *expanding* openings in cohesive ground presented in previous sections consider dry ground conditions. The analysis can be extended to cases in which the ground is saturated and there is a water surface above or below the ground surface —see, for example, Carranza-Torres et al. (2013) and Reich (2016). For the case of *contracting* cavities in cohesive ground, Reich (2016) quantified the difference in factors of safety for cases of circular and spherical cavities in saturated ground, when the water surface is above and below the ground surface, and when two limiting conditions of water inside the cavity are considered, namely the case of flooded cavity and the case of dry cavity (both cases assuming that hydrostatic water pressure exists in the ground surrounding the cavity). Reich (2016) showed that the ratio of factors of safety of cylindrical or spherical cavities in saturated ground and dry ground is approximately equal to two when the cavity is considered to be flooded (the difference in factors of safety depends on the ratio of shear strength of dry and saturated ground, the ratio of unit weights of dry ground and water, and the ratio of unit weights of saturated and dry ground). When the same cavities are assumed dry, the water pressure in the ground surrounding the cavity is assumed to remain hydrostatic, and the tensile strength of the material is assumed to be infinite (so that no tensile failure of the walls of the cavity occurs), then the ratio of factors of safety of

cavities in saturated ground and dry ground is always less than one, and this ratio decreases as the water level above the ground surface increases.

Additional extensions to the proposed analytical solution for both *contracting* and *expanding* cavities are possible. For example, the Hoek-Brown failure criterion (Hoek & Brown 1980; Hoek & Brown 1997; Hoek et al. 2002) is a popular shear strength failure criterion for both intact rock and rock masses that has gained widespread popularity in the design of tunnels and caverns in rock. Using a scaled form of the Hoek-Brown failure criterion (Londe 1988; Carranza-Torres & Fairhurst 1999), compact expressions defining the relationship between factors of safety for shallow cavities and similar scaled variables introduced in Section 3.1, but expressed in terms of scaled Hoek-Brown properties, can be developed. Such relationships could be used to extend the theoretical-practical observations stated earlier on, for particular cases of underground cavities in rock masses.

The developments presented in this study, together with the extensions mentioned above, could be used as preliminary tools for estimation of stability conditions for existing and to-be-designed cavities, not only for application to underground storage CAES systems, which was the original motivation of this study, but also in civil and mining engineering applications, such analysis and design of shallow subway tunnels, design of *crown* pillars in shallow stopes, and others.

References

Abramson, L.W., Thomas, S. L., Sharma, S. & Boyce, G.M. 2002. *Slope stability and stabilization methods* (Second ed.). John Wiley & Sons.

Addison, W. D., Brumpton, G. R., Vallini, D. A., McNaughton, N. J., Davis, D. W., Kissin, S. A., F. P. W. & Hammond, A. L. 2005. Discovery of distal ejecta from the 1850 Ma Sudbury impact event. *Geology 33-3*, 193–196.

Anagnostou, G. & Kovari, K. 1993. Significant parameters in elastoplastic analysis of underground openings. *ASCE J. Geotech. Eng. Div. 119*(3), 401–419.

Atkinson, J. H. & Potts, D. 1977. Stability of a shallow circular tunnel in cohesionless soil. *Geotechnique 27*(2), 203–215.

Bauer, S. J., Gaither, K. N., Webb, S. W. & Nelson, C. 2012. Compressed air energy storage in hard rock. Feasibility study. Technical Report SAND2012-0540, Sandia National Laboratories.

Bell, J. 1966. Dimensionless parameters for homogeneous earth slopes. *Journal of Soil Mechanics & Foundations Div. ASCE SM 5*(GT9), 51–65.

Blindheim, O. T., Broch, E. & Grøv, E. 2004. Gas storage in unlined caverns. Norwegian experience over 25 years. In *Tunnelling and Underground Space Technology. Underground Space for Sustainable Urban Development. Proceedings of the 30th ITA-AITES World Tunnel Congress, Singapore, 22-27 May 2004*, Volume 19.

Brady, B. H. G. & Brown, E. T. 2004. *Rock mechanics for underground mining*. Dordrecht/Boston/London: Kluwer Academic Publishers.

Caquot, A. 1934. *Équilibre des massifs a frottement interne*. Paris: Gaunthier-Villars.

Carranza-Torres, C. 2003. Dimensionless graphical representation of the elasto-plastic solution of a circular tunnel in a Mohr-Coulomb material. *Rock Mechanics and Rock Engineering 36*(3), 237–253.

Carranza-Torres, C. 2004. Report to Geodata S.p.A., Turin, Italy: Computation of factor of safety for shallow tunnels using Caquot's lower bound solution. Technical report, Itasca Consulting Group, Minneapolis.

Carranza-Torres, C. & Fairhurst, C. 1999. The elasto-plastic response of underground excavations in rock masses that satisfy the Hoek-Brown failure criterion. *International Journal of Rock Mechanics and Mining Sciences 36*(8), 777–809.

Carranza-Torres, C., Reich, T. & Saftner, D. 2013. Stability of shallow circular tunnels in soils using analytical and numerical models. In J. Labuz & J. Bentler (Eds.), *Proceedings of the 61st Anunual Geotechnical Engineering Conference*, Minnesota.

Cavallo, A. 2007. Controllable and affordable utility-scale electricity from intermittent wind resources and compressed air energy storage (CAES). *Energy 32*(2), 120–127.

Civil Engineer International 1995. *Tunnel lining removal prompts Los Angeles Metro cave in*. Institution of Civil Engineers, July Issue, 10.

Coduto, D. P., Yeung, M. C. & Kitch, W. A. 2011. *Geotechnical engineering. Principles and practices. Second Edition.* Pearson.

Construction Today 1994a. *Police probe Munich tunnel breach*. Construction Today, October Issue. 4–5.

Construction Today 1994b. *Unstable ground triggers Munich tunnel collapse*. Construction Today, October Issue. 5.

Cornejo, L. 1989. Instability at the face: its repercussions for tunnelling technology. *Tunnels and Tunnelling*. April Issue. 69–74.

Damjanac, B., Carranza-Torres, C. & Dexter, R. 2002. Technical review of the Lined Rock Cavern (LRC) concept and design methodology. Steel liner response. Technical report, Prepared for U.S. Department of Energy National Energy Technology Laboratory Morgantown,West Virginia Under: Prime Contract No. DE-AM26-99FT40463. Subcontract No. 735937-30001-02. Itasca Consulting Group, Inc., Minneapolis, Minnesota, U.S.

Davis, E. H., Gunn, M. J., Mair, R. J. & Seneviratne, H. N. 1980. The stability of shallow tunnels and underground openings in cohesive material. *Geotechnique 30*(4), 397–416.

Davis, R. O. & Selvadurai, A. P. S. 2002. *Plasticity and geomechanics*. Cambridge University Press.

Dawnson, E., Roth, W. & Drescher, A. 1999. Slope stability analysis by strength reduction. *Geotechnique 49*(6), 835–840.

Denholm, P. & Sioshansi, R. 2009. The value of compressed air energy storage with wind in transmission-constrained electric power systems. *Energy Policy 37-8*, 3149–3158.

d'Escatha, Y. & Mandel, J. 1971. Profondeur critique d'eboulement d'un souterrain. *C.R. Acad. Sc. 273*, 470–473.

d'Escatha, Y. & Mandel, J. 1974. Stabilité d'une galerie peu profunde en trerrain meuble. *Inustrie Minérale 6*, 1–9.

Fairhurst, C. & Carranza-Torres, C. 2002. Closing the circle. In J. Labuz & J. Bentler (Eds.), *Proceedings of the 50th Annual. Geotechnical Engineering Conference. February 22, 2002*. University of Minnesota. (Available for downloading at 'Fairhurst Files', www.itascacg.com).

Fosnacht, D. R. & PHES Study Team 2011. Pumped Hydro Energy Storage (PHES) using abandoned mine pits on the Mesabi Iron Range of Minnesota. Technical Report NRRI/TR-2011/50, Natural Resources Research Institute, University of Minnesota Duluth. 599 p. (Available for downloading at http://www.nrri.umn.edu, see Publications).

Fosnacht, D. R., Wilson, E. J., Marr, J. D., Carranza-Torres, C., Hauck, S. A. & Teasley, R. L. 2015. Compressed air energy storage (CAES) in northern Minnesota using underground mine workings and above ground features. Technical Report NRRI/TR-2015/54, Natural Resources Research Institute, University of Minnesota Duluth. 478 p. (Available for downloading at http://www.nrri.umn.edu, see Publications).

Goodall, D. C., Åberg, B. & Brekke, T. L. 1988. Fundamentals of gas containment in unlined rock caverns. *Rock Mechanics and Rock Engineering 21*(4), 235–258.

Government of Singapore 2005. *Report of the Committee of Inquiry into the Incident at the MRT Circle Line Worksite that led to the Collapse of Nicoll Highway on 20 April 2004*. Government of Singapore, Land Transport Authority.

Guglielmetti, V., Grasso, P., Mahtab, A. & Xu, S. 2008. *Mechanized tunnelling in urban areas. Design methodology and construction control*. London.

Hammah, R. E., Yacoub, T. E., Corkum, B. & Wibowo, F. 2007. Analysis of blocky rock slopes with finite element shear strength reduction analysis. In *Proceedings of the 1st Canada-US Rock Mechanics Symposium. Vancouver Rocks 2007*, Vancouver, British Columbia.

Hammah, R. E., Yacoub, T. E. & Curran, J. H. 2007. Serviceability-based slope factor of safety using the shear strength reduction (SSR) method. In C. O. L. Ribeiro e Sousa & N. Grossmann (Eds.), *Proceedings of the 11th Congress of the International Society for Rock Mechanics*, Lisbon.

Hoek, E. & Bray, J. 1981. *Rock slope engineering*. CRC Press.

Hoek, E. & Brown, E. T. 1980. Empirical strength criterion for rock masses. *J. Geotech. Eng. Div. ASCE 106*(GT9), 1013–1035.

Hoek, E. & Brown, E. T. 1997. Practical estimates of rock mass strength. *International Journal of Rock Mechanics and Mining Sciences 34*(8), 1165–1186.

Hoek, E., Carranza-Torres, C. & Corkum, B. 2002, 10 July 2002. Hoek-Brown failure criterion – 2002 edition. In *Proceedings of NARMS-TAC 2002, Mining Innovation and Technology*, Toronto, Canada, pp. 267–273. University of Toronto.

Horn, M. 1961. *Horizontaler Erddruck auf senkrechte Abschlussflchen von Tunneln (Horizontal earth pressure on vertical tunnel fronts)*. Landeskonferenz der ungarischen Tiefbauindustrie (National Conference of Hungarian Civil Engineering Industry). Translation into German by STUVA, Dsseldorf.

Itasca, I. 2008. *FLAC (Fast Lagrangian Analysis of Continua) Version 8.0*. Minneapolis, Minnesota: Itasca Consulting Group, Inc.

Jaeger, J. C., Cook, N. G. W. & Zimmerman, R. 2007. *Fundamentals of rock mechanics* (Fourth ed.). Blackwell Publishing.

Kim, H. M., Park, D., Ryu, D. W. & Song, W. K. 2012. Parametric sensitivity analysis of ground uplift above pressurized underground rock caverns. *Engineering Geology 135-136*, 60–65.

Kolymbas, D. 2005. *Tunnelling and tunnel mechanics: A rational approach to tunnelling*. Springer Science & Business Media.

Kovári, K. 1993. Basic consideration on storage of compressed natural gas in rock chambers. *Rock mechanics and rock engineering 26*(1), 1–27.

Lamppa, M. 2004. *Iron Country: Rich Ore, Rich Lives*. Lake Superior Port Cities Press.

Leoni, L. 1985. Water-filled abandoned mines as heat source for district heating. *Underground Space 9*(1), 23–27.

Liang, J. & Lindblom, U. 1994. Analyses of gas storage capacity in unlined rock caverns. *Rock mechanics and rock engineering 27*(3), 115–134.

Lodge, R. W. D., Gibson, H. L., Stott, G. M., Hudak, G. J., Jirsa, M. A. & Hamilton, M. A. 2013. New U–Pb geochronology from Timiskaming-type assemblages in the Shebandowan and Vermilion greenstone belts, Wawa subprovince, Superior Craton: Implications for the Neoarchean development of the southwestern Superior Province. *Precambrian Research 235*, 264–277.

Londe, P. 1988. Discussion on the paper 'Determination of the shear stress failure in rock masses', by R. Ucar (Paper 20431), March, 1986, Vol. 112, No.3. *J. Geotech. Eng. Div. ASCE 114-3*(GT9), 374–376.

Lyamin, A. V. & Sloan, S. W. 2002a. Lower bound limit analysis using non-linear programming. *International Journal for Numerical Methods in Engineering 55*(5), 573–611.

Lyamin, A. V. & Sloan, S. W. 2002b. Upper bound limit analysis using linear finite elements and non-linear programming. *International Journal for Numerical and Analytical Methods in Geomechanics 26*(2), 181–216.

Mandel, J., Habib, P., D'Escatha, Y., Halpen, B., Luong, M. P. & Zarka, J. 1974. Etude theorique et experimentale de la stabilité des cavités souterraines. In *Symposium franco-polonais de problémes de rhéologie et de mécanique des sols*, Nice, pp. 255–270.

Marsden, R. 1968. *Geology of the Iron Ores of the Lake Superior Region in the United States. Ridge J. D. (Ed.)*, Volume 1. The American Institute of Mining, Metallurgical, and Petroleum Engineers, Inc. 490-492.

Michalowski, R. L. 2002. Stability charts for uniform slopes. *Journal of Geotechnical and Geoenvironmental Engineering. ASCE 128-4*(GT9), 351–355.

MNDNR-LAM 2011. Underground mine mapping project: A geographic information system of the documented underground mine features on the Mesabi Iron Range. Technical report, Minnesota Department of Natural Resources (MNDNR). Division of Lands and Minerals (LAM). (Available for downloading at http://www.dnr.state.mn.us/lands_minerals/underground/index.html).

Mühlhaus, H. B. 1985. Lower bound solutions for circular tunnels in two and three dimensions. *Rock Mechanics and Rock Engineering 18*, 37–52.

Oliver, A. 1995. Los Angeles metro collapse investigation focuses on tunnel lining replacement. *Ground Engineering 28*(6), 4–5.

Peele, R. 1945. *Mining engineers handbook* (3rd ed.), Volume 1. John Wiley and Sons.

Peterson, D., Gallup, C., Jirsa, M. & Davis, D. W. 2001. Correlation of the Archean assemblages across the US-Canadian border: Phase I geochronology. In *47th Annual Meeting, Institute on Lake Superior Geology, Proceedings*, Volume 47, pp. 77–78.

Pietruszczak, S. 2010. *Fundamentals of plasticity in geomechanics*. CRC Press.

Plaxis b.v. 2012. *PLAXIS Version 2012*. Delft, Netherlands.

Potts, D. M. & Zdravkovic, L. 1999. *Finite element analysis in geotechnical engineering. Theory*. London: Thomas Telford.

Proctor, R. V. & White, T. L. 1977. *Earth tunnelling with steel supports*. Commerical Shearing, Inc., Ohio.

Reich, T. 2016. Application of Caquot's solution to the analysis of stability of shallow circular cavities in Tresca material. Master's thesis, University of Minnesota, Duluth Campus. Minnesota, USA.

Rocscience 2014. *RS2 Version 9*. Toronto, Canada.

Shidahara, T., Oyama, T. & Nakagawa, K. 1993. The hydrogeology of granitic rocks in deep boreholes used for compressed air storage. *Engineering Geology 35*, 207–213.

Sofregaz U.S. Inc. 1999. Commercial potential of natural gas storage in Lined Rock Caverns (LRC). Technical report, Prepared for the U.S. Department of Energy, Morgantown, WV, 101 p.

Succar, S. & Williams, R. H. 2008. Compressed air energy storage: Theory, resources and application for wind power. Technical report, Prepared by the Energy Systems Analysis Group: Princeton Environmental Institute, Princeton University, 81 p.

Tamez, E., Rangel, J. L. & Holgun, E. 1997. *Diseño Geotécnico de Túneles*. Editorial TGC, Mexico.

Tanzini, M. 2001. *Gallerie. Aspetti geotecnici nella progettazione e costruzione*. Dario Flaccovio Editore. Palermo. Italia.

Terzaghi, K. 1943. *Throretical soil mechanics*. New York: John Wiley & Sons, Inc.

Wyllie, D. C. & Mah, C. W. 2004. *Rock slope engineering. Civil and mining*. Taylor & Francis.

Zaugg, P. 1975. Air-storage power generating plants. *Brown Boveri Review 62*, 338–347.

Appendix A. Derivation of the analytical solution for contracting and expanding cavities in dry cohesive ground

This appendix presents the derivation of the analytical solution for *contracting* cavities (equations 12 through 15 and for *expanding* cavities (equations 12 and 13; and equations 17 and 18) in dry cohesive ground, using the scaling rules introduced by equations (5) through (9).

Figure A-1, which is equivalent to Figure 14 discussed in the main text, shows the problem and variables involved in the derivation presented in this appendix.

Considering a polar (or spherical) coordinate system, (ρ, θ), the force equilibrium equations inside the integration circle in Figure A-1 that account for the self weight of the material, are partial differential equations involving the (scaled) radial and tangential (or hoop) stresses, $\tilde{\sigma}_r$ and $\tilde{\sigma}_\theta$, respectively (see, for example, Jaeger et al. 2007). For the radial direction, the equilibrium equation is

$$\frac{\partial \tilde{\sigma}_r}{\partial \rho} + k\,\frac{\tilde{\sigma}_r - \tilde{\sigma}_\theta}{\rho} + \sin\theta = 0 \tag{A-1}$$

and for the tangential direction, it is

$$\frac{1}{\rho}\,\frac{\partial \tilde{\sigma}_\theta}{\partial \theta} + \cos\theta = 0 \tag{A-2}$$

In equation (A-1), the parameter k is such that $k = 1$ implies that the cavity is cylindrical, while $k = 2$ implies that the cavity is spherical.

In the derivation that follows, the cavity in Figure A-1 is assumed to be at the verge of equilibrium; in particular, the cohesion, c, of the ground is assumed to be the critical cohesion that leads to collapse of the cavity. The Tresca shear failure criterion (see equations 3 and 4) is expressed in terms of scaled principal stresses, $\tilde{\sigma}_1$ and $\tilde{\sigma}_3$, as follows

$$\tilde{\sigma}_1 = \tilde{\sigma}_3 + 2\,\tilde{c} \tag{A-3}$$

where $\tilde{c}$ is the scaled cohesion defined by equation (7).

Note that in this appendix, in contrast with the notation used in the equations in Section 3.2, the critical scaled cohesion associated with the cavity in a critical state of equilibrium is denoted simply as $\tilde{c}$, rather than as $\tilde{c}_{cr}$.

The first step to derive the solution of the problem in Figure A-1 is to solve for the stress quantities along the vertical segment defined by points A and B. The superscript 'AB' is used to denote stresses along this segment (see Figure A-1). For the case of *contracting* cavities, the hoop stresses are considered to be major principal stresses, while radial stresses are considered to be minor principal stresses —i.e., $\tilde{\sigma}_\theta^{AB} = \tilde{\sigma}_1$ and $\tilde{\sigma}_r^{AB} = \tilde{\sigma}_3$, respectively. For the case of *expanding* cavities, the opposite assumption is made —i.e., $\tilde{\sigma}_\theta^{AB} = \tilde{\sigma}_3$ and $\tilde{\sigma}_r^{AB} = \tilde{\sigma}_1$, respectively. Therefore, in view of equation (A-3), the relationship between the (scaled) hoop stresses, $\tilde{\sigma}_\theta^{AB}$, and the (scaled) radial stresses, $\tilde{\sigma}_r^{AB}$, is written as [1]

$$\tilde{\sigma}_\theta^{AB} = \tilde{\sigma}_r^{AB} \pm 2\,\tilde{c} \tag{A-4}$$

Along the segment AB in Figure A-1, the equilibrium equation for the radial direction is obtained from equation (A-1), making $\theta = \pi/2$, to yield the following total differential equation of the variable ρ,

$$\frac{\mathrm{d}\tilde{\sigma}_r^{AB}}{\mathrm{d}\rho} + k\,\frac{\tilde{\sigma}_r^{AB} - \tilde{\sigma}_\theta^{AB}}{\rho} + 1 = 0 \tag{A-5}$$

Replacing equation (A-4) in equation (A-5), a total differential equation of the unknown variable $\tilde{\sigma}_r^{AB}$ only is obtained. This equation can be solved considering the following boundary condition

$$\tilde{\sigma}_r^{AB} = \tilde{q}_s \quad \text{at} \quad \rho = \xi \tag{A-6}$$

In this way, the solution for $\tilde{\sigma}_r^{AB}(\rho)$ results (see footnote associated with equation A-4)

$$\tilde{\sigma}_r^{AB}(\rho) = \tilde{q}_s + \xi - \rho \pm 2\,k\,\tilde{c}\,\ln\frac{\rho}{\xi} \tag{A-7}$$

[1] The symbol $\pm$ in equations (A-4), (A-7), (A-8), (A-14), (A-20) and (A-22) is used to indicate that addition $(+)$ applies to *contracting* cavities and subtraction $(-)$ applies to *expanding* cavities.

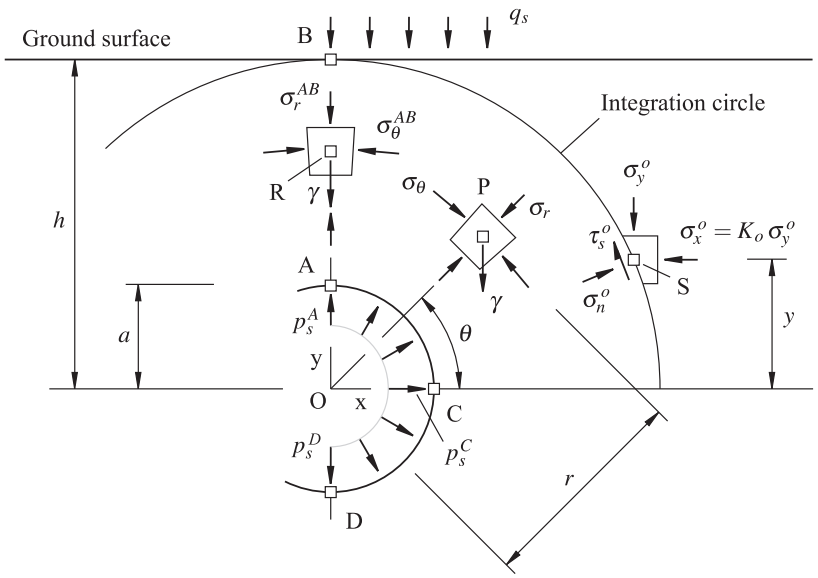

Figure A-1. Problem of stability of a cylindrical or spherical (*contracting* or *expanding*) shallow cavity. Note the representation of the stress states on the segment *AB* and on the integration circle boundary.

Also, in view of equation (A-4), the solution for $\tilde{\sigma}_\theta^{AB}(\rho)$ results (see footnote associated with equation A-4)

$$\tilde{\sigma}_\theta^{AB}(\rho) = \tilde{\sigma}_r^{AB}(\rho) \pm 2\tilde{c} \tag{A-8}$$

Note that equations (A-7) and (A-8), with positive last terms, are the same equations (14) and (15) in the main text for the case of *contracting* cavities, while equations (A-7) and (A-8), with negative last terms, are the same equations (17) and (18) in the main text for the case of *expanding* cavities. As explained earlier on, the cohesion is denoted as $\tilde{c}_{cr}$ in the equations in the main text, while the same cohesion is denoted as $\tilde{c}$ in the equations in this appendix.

The scaled internal pressure at the *crown* of the cavity, $\tilde{p}_s^A$, (see Figure A-1) can be found by applying the following boundary condition to equation (A-7)

$$\tilde{\sigma}_r^{AB} = \tilde{p}_s^A \quad \text{at} \quad \rho = 1 \tag{A-9}$$

This yields [2]

$$\tilde{p}_s^A = \tilde{q}_s + \xi - 1 \mp 2k\tilde{c}\ln\xi \tag{A-10}$$

Note that equation (A-10) with a negative last term is the same equation (16) presented in the main text for the case of *contracting* cavities, while equation (A-10) with a positive last term is the same equation (19) presented in the main text for the case of *expanding* cavities.

The second step to derive the solution of the problem in Figure A-1 is to integrate the equilibrium equation for the tangential direction (equation A-2) throughout the integration circle. Integrating equation (A-2) with respect to the variable θ, the general solution for the scaled hoop stress, $\tilde{\sigma}_\theta(\rho,\theta)$, results

$$\tilde{\sigma}_\theta(\rho,\theta) = -\rho\,\sin\theta + \tilde{C}_1(\rho) \tag{A-11}$$

where $\tilde{C}_1(\rho)$ is an integration function of the variable ρ (i.e., of the variable disregarded in the integration). At $\theta = \pi/2$ (on the segment *AB*) the solution for $\tilde{\sigma}_\theta(\rho,\theta)$ given by equation (A-11) must be equal to the solution for $\tilde{\sigma}_\theta^{AB}(\rho)$ given by equation (A-8). In this way, the integration function, $\tilde{C}_1(\rho)$, is found to be

$$\tilde{C}_1(\rho) = \rho + \tilde{\sigma}_\theta^{AB}(\rho) \tag{A-12}$$

[2]The symbol $\mp$ in equation (A-10) is used to indicate that subtraction $(-)$ applies to *contracting* cavities and addition $(+)$ applies to *expanding* cavities.

Replacing equation (A-12) into equation (A-11), the final solution for the scaled hoop stress, $\tilde{\sigma}_\theta(\rho,\theta)$, becomes

$$\tilde{\sigma}_\theta(\rho,\theta) = \tilde{\sigma}_\theta^{AB}(\rho) + \rho\,(1-\sin\theta) \tag{A-13}$$

Note that equation (A-13) is the same equation (13) in the main text that applies to both *contracting* and *expanding* cavities.

The third step to derive the solution of the problem in Figure A-1 is to integrate the equilibrium equation for the radial direction (equation A-1) throughout the integration circle. Replacing equation (A-13) into equation (A-1) and integrating with respect to the variable ρ, the general solution for the scaled radial stress, $\tilde{\sigma}_r(\rho,\theta)$, results (see footnote associated with equation A-4)

$$\tilde{\sigma}_r(\rho,\theta) = \tilde{q}_s + \xi \pm 2k\tilde{c}\,\ln\frac{\rho}{\xi} - \rho\,\sin\theta + \rho^{-k}\tilde{C}_2(\theta) \tag{A-14}$$

where $\tilde{C}_2(\theta)$ is an integration function of the variable θ (i.e., of the variable disregarded in the integration). At $\theta = \pi/2$ (on the segment AB) the solution for $\tilde{\sigma}_r(\rho,\theta)$ given by equation (A-14) must be equal to the solution for $\tilde{\sigma}_r^{AB}(\rho)$ given by equation (A-7). In this way the integration function, $\tilde{C}_2(\theta)$, is found to be

$$\tilde{C}_2(\theta) = 0 \tag{A-15}$$

Replacing equation (A-15) into equation (A-14), the final solution for the scaled radial stress, $\tilde{\sigma}_r(\rho,\theta)$, becomes

$$\tilde{\sigma}_r(\rho,\theta) = \tilde{\sigma}_r^{AB}(\rho) + \rho\,(1-\sin\theta) \tag{A-16}$$

Note that equation (A-16) is the same equation (12) in the main text that applies to both *contracting* and *expanding* cavities.

In the remainder of this appendix some observations about particular features of the solution derived above are highlighted.

The first observation to be made is about the distribution of internal pressure for the cavity predicted by the proposed solution. The scaled internal pressure function, $\tilde{p}_s(\theta)$, is obtained by making $\rho = 1$ in equation (A-16). This yields

$$\tilde{p}_s(\theta) = \tilde{p}_s^A + 1 - \sin\theta \tag{A-17}$$

As expected, equation (A-17) predicts that at the *crown* of the cavity (i.e., $\theta = \pi/2$, see point A in Figure A-1) the scaled internal pressure becomes equal to $\tilde{p}_s^A$. Also, equation (A-17) predicts that at the *spring line* of the cavity (i.e., at $\theta = 0$, see point C in Figure A-1) and at the *invert* of the cavity (i.e., at $\theta = -\pi/2$, see point D in Figure A-1) the scaled internal pressures $\tilde{p}_s^C$ and $\tilde{p}_s^D$ are, respectively

$$\tilde{p}_s^C = \tilde{p}_s^A + 1; \qquad \tilde{p}_s^D = \tilde{p}_s^A + 2 \tag{A-18}$$

Considering the scaling rule for internal pressure (see left-side equation 8), equation (A-18) predicts the following (unscaled) internal pressures at the *spring line* and *invert* of the cavity, respectively,

$$p_s^C = p_s^A + \gamma a; \qquad p_s^D = p_s^A + 2\gamma a \tag{A-19}$$

Equation (A-19) indicates that the cavity internal pressure increases with depth in a *lithostatic* manner, as if the internal pressure is provided by an imaginary pressurized gas which has the same unit weight as the ground surrounding the cavity.

The second observation to be made is about the stress state of the ground inside the integration circle in Figure A-1. When deriving the solution of the problem stated in this figure, the assumption was made that the radial and hoop stresses on the vertical segment AB were compatible with a plastic state (see equation A-4); nevertheless no assumption was made about the relationship between radial and hoop stresses elsewhere throughout the integration circle (e.g., whether these stresses are compatible with a plastic or with an elastic state). Subtracting the solution for scaled hoop and radial stresses given by equations (A-13) and (A-16), respectively, gives (see footnote associated with equation A-4)

$$\tilde{\sigma}_\theta(\rho,\theta) - \tilde{\sigma}_r(\rho,\theta) = \tilde{\sigma}_\theta^{AB} - \tilde{\sigma}_r^{AB} = \pm 2\tilde{c} \tag{A-20}$$

Equation (A-20) indicates that in the proposed analytical solution the ground is in plastic state throughout the entire integration circle and not just on the segment *AB*.

The third and last observation to be made is about the continuity of the stress field across the integration circle boundary (see Figure A-1). For the proposed analytical solution to be a statically admissible solution, continuity of radial and shear stresses must exist across the integration circle boundary; the hoop stress, though, may be discontinuous (see, for example, Davis & Selvadurai 2002; Pietruszczak 2010).

The scaled radial stress on the integration circle boundary, inside the integration circle, is obtained from equation (A-16) making $\rho = \xi$. This gives

$$\tilde{\sigma}_r(\xi,\theta) = \tilde{q}_s + \xi\,(1-\sin\theta) \tag{A-21}$$

The scaled hoop stress on the integration circle boundary, inside the integration circle, is similarly obtained from equation (A-13) (see also equation A-20) and results (see footnote associated with equation A-4)

$$\tilde{\sigma}_\theta(\xi,\theta) = \tilde{\sigma}_r(\xi,\theta) \pm 2\,\tilde{c} \tag{A-22}$$

The scaled vertical stress on the integration circle boundary, outside the integration circle, is obtained from the left-side equation (9) considering $y/a = \xi \sin\theta$ (see Figure A-1). This gives

$$\tilde{\sigma}_y^o(\xi,\theta) = \tilde{q}_s + \xi\,(1-\sin\theta) \tag{A-23}$$

The scaled horizontal stress on the integration circle boundary, outside the integration circle, is similarly obtained from the right-side equation (9) and from equation (A-23) and results

$$\tilde{\sigma}_x^o(\xi,\theta) = K_o\,\tilde{q}_s + K_o\,\xi\,(1-\sin\theta) \tag{A-24}$$

The scaled radial and shear stresses, $\tilde{\sigma}_n^o$ and $\tilde{\tau}_s^o$ respectively, on the integration circle boundary, outside the integration circle, can be obtained with the following classical stress transformation formulae (see, for example, Jaeger et al. 2007)

$$\tilde{\sigma}_n^o = \tilde{\sigma}_x^o \cos^2\theta + \tilde{\sigma}_y^o \sin^2\theta \tag{A-25}$$

and

$$\tilde{\tau}_s^o = \frac{\tilde{\sigma}_y^o - \tilde{\sigma}_x^o}{2} \sin 2\theta \tag{A-26}$$

Replacing equations (A-23) and (A-24) into equations (A-25) and (A-26), the scaled radial stress results

$$\tilde{\sigma}_n^o = \left(\sin^2\theta + K_o\cos^2\theta\right)\left[\tilde{q}_s + \xi\,(1-\sin\theta)\right] \tag{A-27}$$

and the scaled shear stress results

$$\tilde{\tau}_s^o = -\frac{K_o - 1}{2} \sin 2\theta\,\left[\tilde{q}_s + \xi\,(1-\sin\theta)\right] \tag{A-28}$$

Considering the case $K_o = 1$ (i.e., the horizontal and vertical *in-situ* stresses are the same) in equations (A-27) and (A-28), the stresses $\tilde{\sigma}_n^o$ and $\tilde{\tau}_s^o$ result to be, respectively

$$\tilde{\sigma}_n^o = \tilde{q}_s + \xi\,(1-\sin\theta) \tag{A-29}$$

and

$$\tilde{\tau}_s^o = 0 \tag{A-30}$$

Equation (A-29) is the same as equation (A-21), implying continuity of radial stresses across the integration circle boundary (for the assumed case $K_o = 1$). Also, equation (A-30) and the fact that the shear stresses are assumed null inside the integration circle (see Figure A-1), imply that there is also continuity of shear stresses across the integration circle boundary (again for the assumed case $K_o = 1$). With regard to the hoop stresses on the integration circle boundary, equation (A-22) indicates these stresses are discontinuous across the boundary; the difference in hoop stresses when passing from the external to the internal sides of the integration circle boundary are equal to $2\,\tilde{c}$ for *contracting* cavities and equal to $-2\,\tilde{c}$ for *expanding* cavities. The observations

regarding the continuity of radial and shear stresses across the integration boundary show that the proposed solution is a statically admissible solution when the coefficient of earth pressure at rest is considered to be equal to one.

Appendix B. Effect of internal pressure distribution and in-situ stresses on stability of shallow cavities

This appendix discusses the effect of considering two types of distributions of internal pressure for the cavity as well as considering different values of coefficient of earth pressure at rest for the ground, on the factor of safety.

The effect of the distribution of internal pressure on the factor of safety is discussed first.

Appendix A shows that the analytical solution for cohesionless ground proposed in this paper considers a *lithostatic* distribution of internal pressure in the cavity, as if provided by an imaginary pressurized gas which has the same unit weight as the ground surrounding the cavity. All the numerical finite-element (FLAC) models discussed in the main text (Sections 4 and 6) consider such *lithostatic* distribution of internal pressure. Since other authors have proposed lower bound solutions for which the distribution of internal pressure in *contracting* cavities is *uniform* (see, for example, Davis et al. 1980; Mühlhaus 1985), numerical finite-difference (FLAC) models have been set up and computed considering *uniform* distribution of internal pressure, to observe the differences in resulting factors of safety with respect to the *lithostatic* distribution.

Figure B-1a represents the *lithostatic* distribution of internal pressure. The figure indicates the values of internal pressure at four distinct points on the periphery of the cavity, namely the *crown* point A, the *spring line* point C, the *invert* point D, and a point E located above point C, at a height equal to one half the radius of the opening. Figure B-1b represents the *uniform* distribution of internal pressure. The figure indicates the three values of *uniform* internal pressure to be investigated, corresponding to the values of *lithostatic* pressure at points a) A, b) C and c) E.

Figures B-2 and B-3 show similar diagrams as in Figure 28, representing values of factor of safety as a function of scaled cohesion for cylindrical *contracting* cavities at scaled depths, $\xi = 2$ and 4, respectively. In these figures, the continuous lines correspond to the analytical solution given by equation (21), while the symbols correspond to the different cases of internal pressure distribution shown in Figure B-1b. Note that in Figures B-2 and B-3, the square symbols represent the *lithostatic* distribution of internal pressure (i.e., these symbols are the same ones represented in Figure 28) while the circle symbols represent the *uniform* distribution for case c) in Figure B-1b (i.e., the case of *uniform* distribution with a magnitude equal to the *lithostatic* pressure value at point E in Figure B-1a). Table B-1 summarizes the input parameters and results for the different cases represented by symbols in Figures B-2 and B-3. Inspection of the relative position of the symbols and lines in Figures B-2 and B-3, together with values of factors of safety reported in Table B-1, suggests that considering the *uniform* distribution for case a) in Figure B-1b gives the closest (conservative) equivalence with the *lithostatic* distribution considered by the analytical solution. This means that if the analytical solution for factor of safety presented in the main text is to be applied to cases in which the internal pressure is *uniform*, then the reference scaled pressure at the *crown*, $\tilde{p}_s = \tilde{p}_s^A$ (see Figure 14), will lead to a conservative estimate of factor of safety. For completeness, Figure B-4 shows the shape of plastic zones in the numerical finite-difference (FLAC) models for the first unstable situation for Case 2c in Table B-1, considering the various distributions of internal pressure shown in Figure B-1. Without considering the extent of plastic failure region, the shapes of the plastic failure region for *uniform* internal pressure distributions seem to be equivalent to those obtained for the *lithostatic* internal pressure distribution.

A similar analysis of the effect of internal pressure distributions on the factor of safety was carried out for cylindrical *expanding* cavities. Figures B-5, B-6 and B-7 and Table B-2 are equivalent to Figures B-2, B-3 and B-4 and Table B-1, respectively, this time for the case of *expanding* cavities with scaled internal pressure (at the *crown*) equal to two times the reference internal pressure given by equation (10) (i.e., $\tilde{p}_s = 2\,\tilde{p}_s^o$). Similar observations as for the case of *contracting* cavities are made for the case of *expanding* cavities: if the analytical solution for factor of safety presented in the main text is to be applied to cases in which the internal pressure is *uniform*, then the reference scaled pressure at the *crown*, $\tilde{p}_s = \tilde{p}_s^A$ (see Figure 14), has to be corrected by adding the quantity $1/2$ (or adding the quantity $\gamma a/2$ to the unscaled *crown* pressure, $p_s = p_s^A$) to get a conservative estimate for the factor of safety.

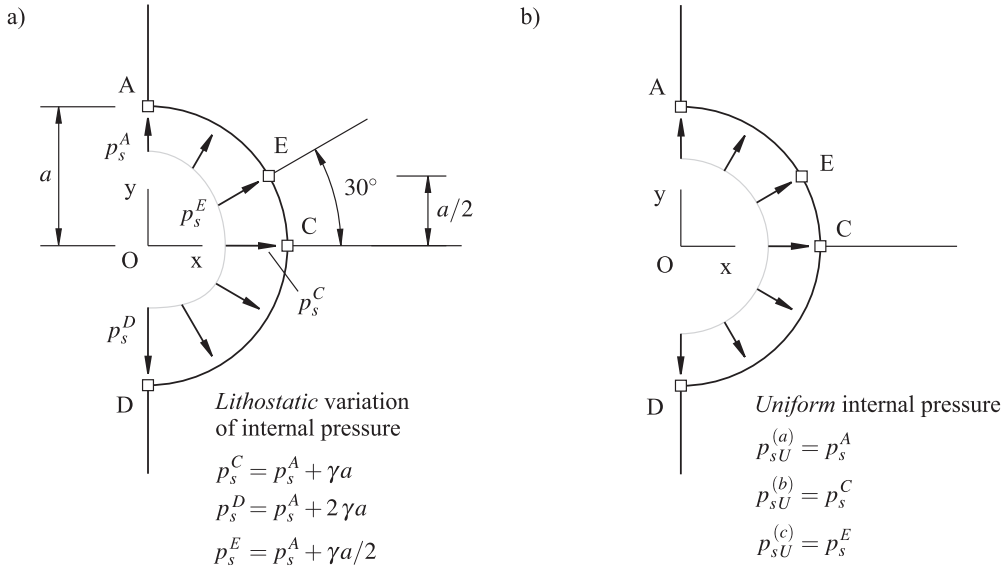

Figure B-1. a) *Lithostatic* distribution of internal pressure for the cavity considered in the analytical model in this study. Points *A* and *C* are located at the *crown* and *spring line* levels on the periphery of the cavity, respectively, while point *E* is located at a vertical distance $a/2$ from the axis of the cavity. b) *Uniform* internal pressure distribution considered for the cavity. The cases indicated as $p_{sU}^{(a)}$, $p_{sU}^{(b)}$ and $p_{sU}^{(c)}$ correspond to *uniform* pressure distributions with magnitudes equal to the pressure at points *A*, *C* and *E*, respectively.

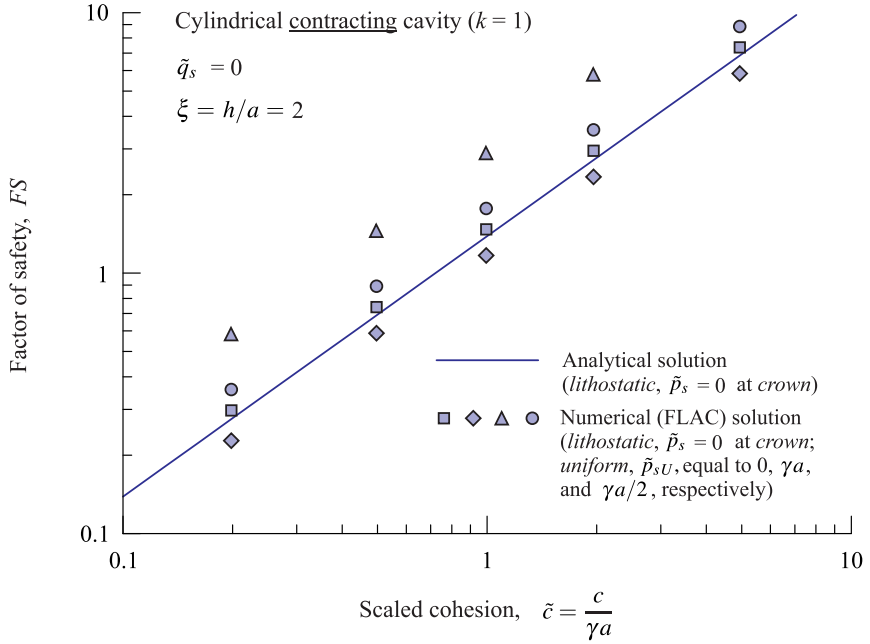

Figure B-2. Graphical representation similar to that in Figure 28, showing the relationship between factor of safety and scaled ground cohesion for cylindrical *contracting* cavities at the scaled depth, $\xi = 2$. The symbols in the diagram represent the factors of safety obtained with the numerical (FLAC) models for the *lithostatic* distribution of internal pressure and for the three cases of *uniform* pressure distributions represented in Figure B-1b.

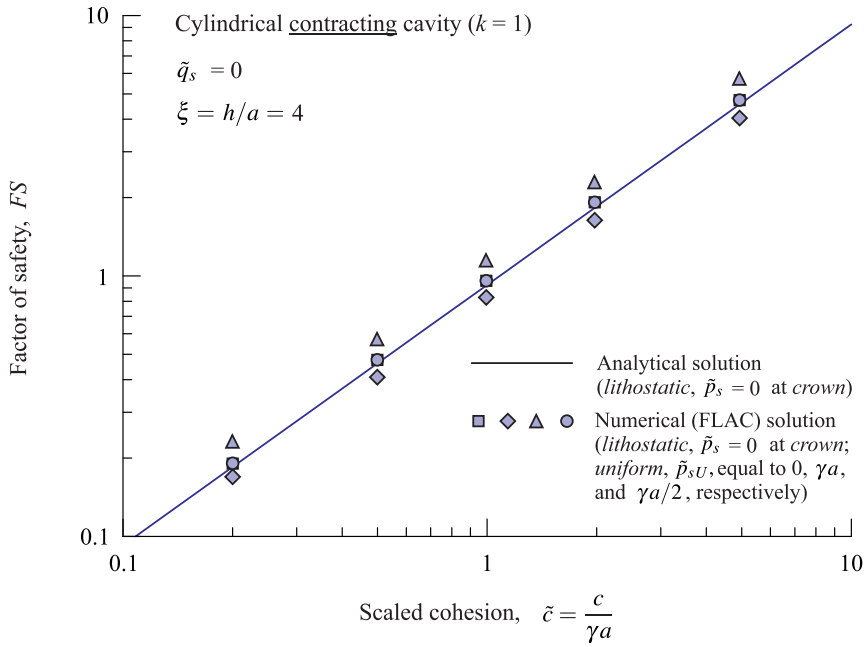

Figure B-3. Graphical representation similar to that in Figure B-2 for cylindrical *contracting* cavities at the scaled depth, $\xi = 4$.

Table B-1. Summary of input data and results for different cases of cylindrical *contracting* cavities and internal pressure distributions solved with numerical (FLAC) models, represented in Figures B-2 and B-3.

Case	ξ [-]	$\tilde{c}$ [-]	p_s [kPa]	$p_{sU}^{(a)}$ [kPa]	$p_{sU}^{(b)}$ [kPa]	$p_{sU}^{(c)}$ [kPa]	FS [-]	$FS_{psU}^{(a)}$ [-]	$FS_{psU}^{(b)}$ [-]	$FS_{psU}^{(c)}$ [-]
2a	2.0	0.2	0.00	0.00	97.52	48.760	0.30	0.23	0.58	0.36
2b	2.0	0.5	0.00	0.00	46.17	23.085	0.75	0.59	1.44	0.90
2c	2.0	1.0	0.00	0.00	55.90	27.950	1.50	1.17	2.88	1.80
2d	2.0	2.0	0.00	0.00	72.80	36.400	3.00	2.35	5.77	3.59
2e	2.0	5.0	0.00	0.00	45.36	22.680	7.50	5.87	14.41	8.98
4a	4.0	0.2	0.00	0.00	28.60	14.300	0.19	0.17	0.23	0.19
4b	4.0	0.5	0.00	0.00	71.64	35.820	0.48	0.41	0.57	0.48
4c	4.0	1.0	0.00	0.00	28.00	14.000	0.97	0.83	1.14	0.96
4d	4.0	2.0	0.00	0.00	38.19	19.095	1.94	1.65	2.28	1.92
4e	4.0	5.0	0.00	0.00	104.81	52.405	4.84	4.13	5.71	4.80

The column labelled as *FS* lists the values of factor of safety for the case of *lithostatic* internal pressure with scaled *crown* internal pressure, $\tilde{p}_s = 0$ (this column is the same as the column labelled FS_N in Table 2). The columns labelled as $FS_{psU(a)}$, $FS_{psU(b)}$ and $FS_{psU(c)}$ list the values of factor of safety for *uniform* internal pressure corresponding to scaled values, $\tilde{p}_{sU}$, equal to a) 0; b) γa; and c) $\gamma a/2$, respectively (see Figure B-1).

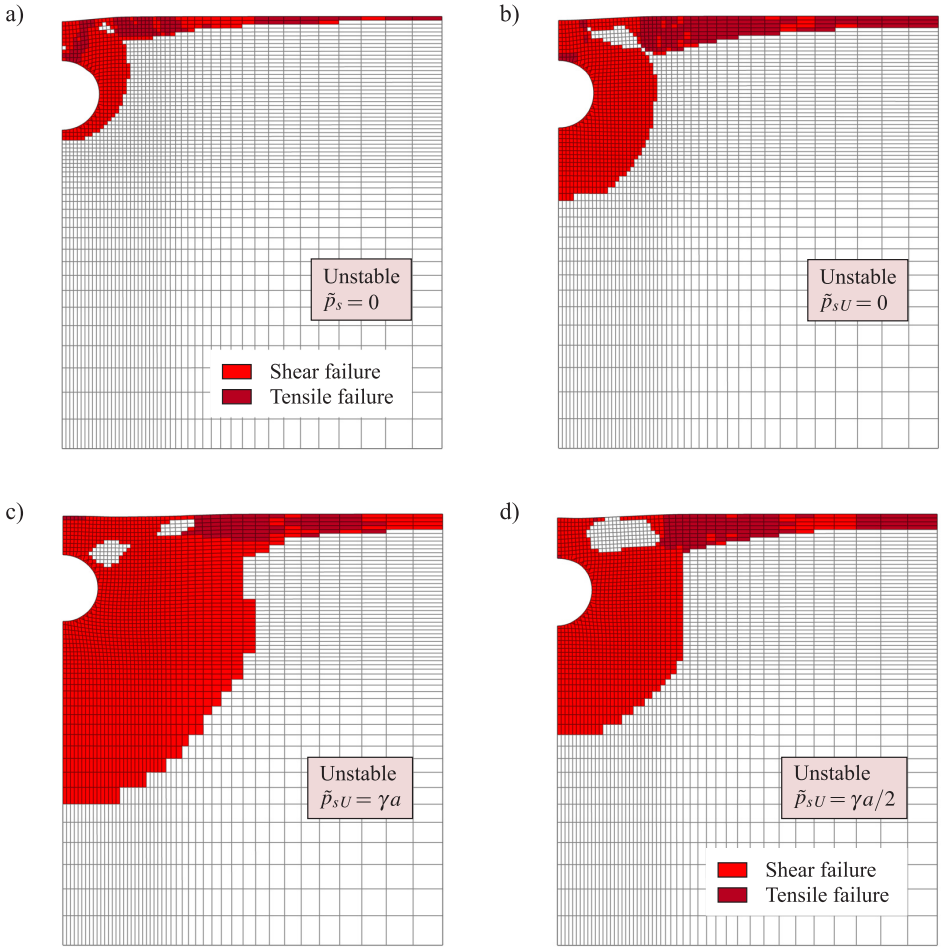

Figure B-4. First unstable situation in the computation of factor of safety with numerical (FLAC) models for cases of cylindrical *contracting* cavities with various distributions of internal pressure, corresponding to Case 2c in Table B-1. The cases correspond to the following internal pressure distributions: a) *lithostatic*, with zero *crown* pressure; *uniform* pressure equal to b) zero; c) γa and d) $\gamma a/2$.

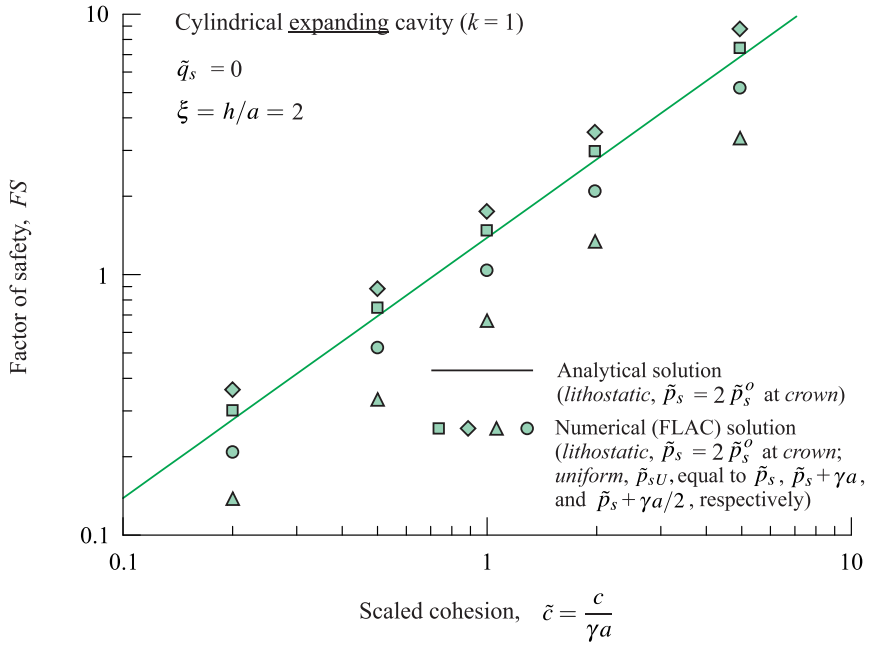

Figure B-5. Graphical representation similar to that in Figure B-2 for cylindrical *expanding* cavities at the scaled depth, $\xi = 2$.

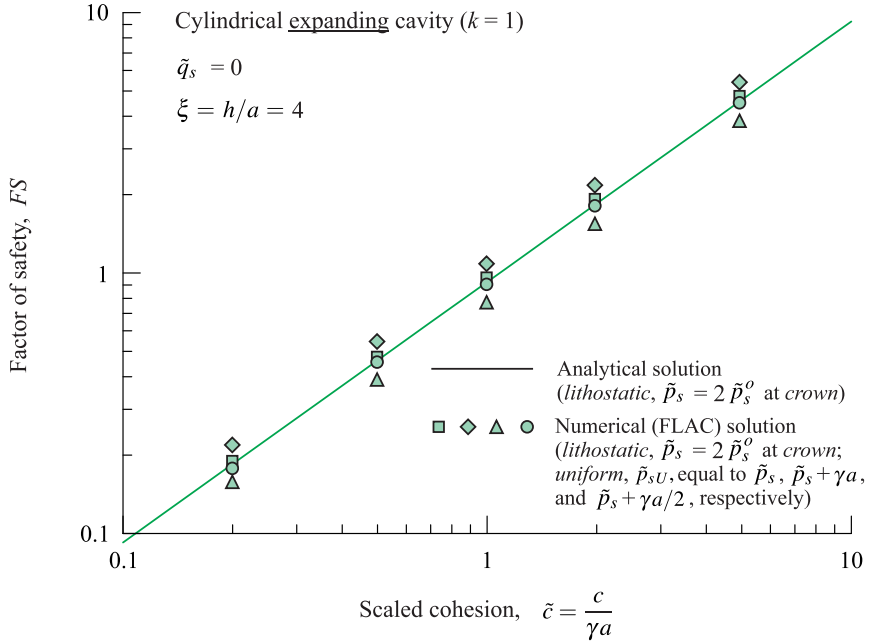

Figure B-6. Graphical representation similar to that in Figure B-5 for cylindrical *expanding* cavities at the scaled depth, $\xi = 4$.

Table B-2. Summary of input data and results for different cases of cylindrical *expanding* cavities and internal pressure distributions solved with numerical (FLAC) models, represented in Figures B-5 and B-6.

Case	ξ [-]	$\tilde{c}$ [-]	p_s [kPa]	$p_{sU}^{(a)}$ [kPa]	$p_{sU}^{(b)}$ [kPa]	$p_{sU}^{(c)}$ [kPa]	FS [-]	$FS_{psU}^{(a)}$ [-]	$FS_{psU}^{(b)}$ [-]	$FS_{psU}^{(c)}$ [-]
2a	2.0	0.2	195.04	195.04	292.56	243.800	0.30	0.36	0.14	0.21
2b	2.0	0.5	92.34	92.34	138.51	115.425	0.75	0.89	0.34	0.53
2c	2.0	1.0	111.80	111.80	167.70	139.750	1.50	1.78	0.68	1.06
2d	2.0	2.0	145.60	145.60	218.40	182.000	3.01	3.56	1.37	2.12
2e	2.0	5.0	90.72	90.72	136.08	113.400	7.52	8.89	3.43	5.30
4a	4.0	0.2	171.60	171.60	200.20	185.900	0.19	0.22	0.16	0.18
4b	4.0	0.5	429.84	429.84	501.48	465.660	0.49	0.55	0.40	0.46
4c	4.0	1.0	168.00	168.00	196.00	182.000	0.97	1.10	0.79	0.92
4d	4.0	2.0	229.14	229.14	267.33	248.235	1.94	2.20	1.59	1.85
4e	4.0	5.0	628.86	628.86	733.67	681.265	4.85	5.49	3.97	4.61

The column labelled as *FS* lists the values of factor of safety for the case of *lithostatic* internal pressure with scaled *crown* internal pressure, $\tilde{p}_s = 2\,\tilde{p}_s^o$ (this column is the same as the column labelled FS_N in Table 2). The columns labelled as $FS_{psU(a)}$, $FS_{psU(b)}$ and $FS_{psU(c)}$ list the values of factor of safety for *uniform* internal pressure corresponding to scaled values, $\tilde{p}_{sU}$, equal to a) $2\,\tilde{p}_s^o$; b) $2\,\tilde{p}_s^o + \gamma a$; and c) $2\,\tilde{p}_s^o + \gamma a/2$, respectively (see Figure B-1).

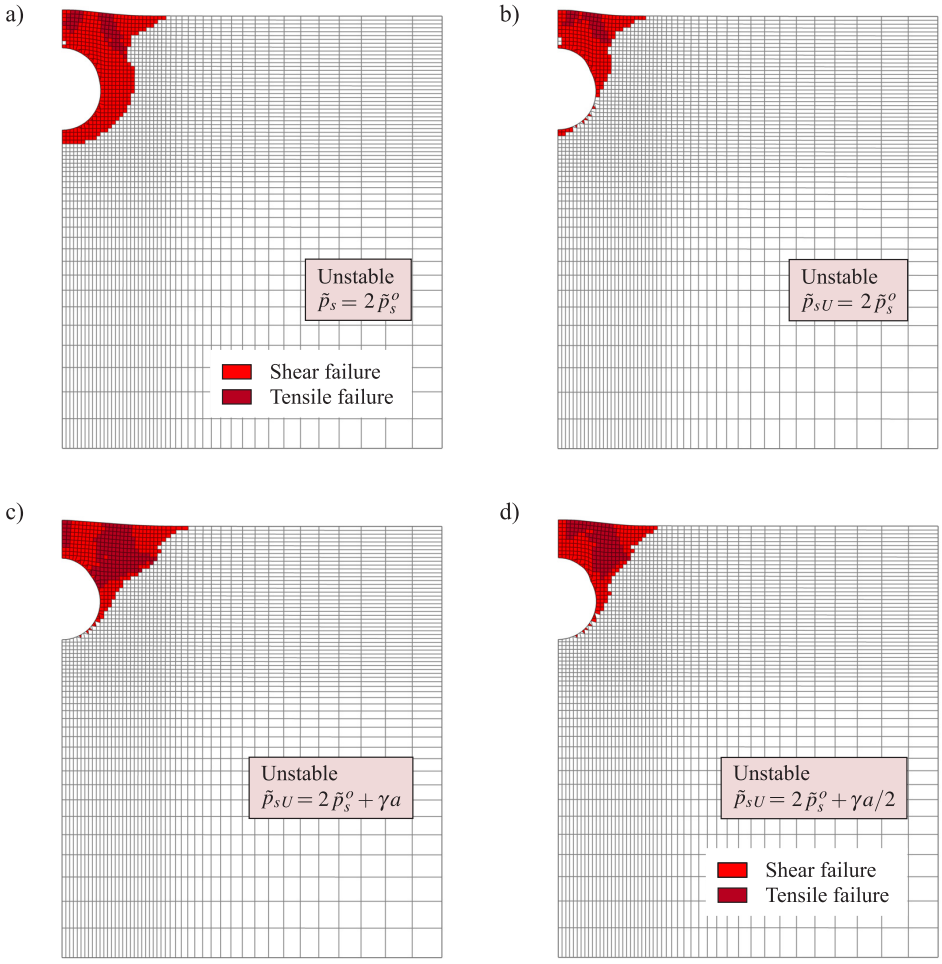

Figure B-7. First unstable situation in the computation of factor of safety with numerical (FLAC) models for cases of cylindrical *expanding* cavities with various distributions of internal pressure, corresponding to Case 2c in Table B-2. The cases correspond to the following internal pressure distributions: a) *lithostatic*, with pressure equal to $2\,\tilde{p}_s^o$; *uniform* pressure equal to b) $2\,\tilde{p}_s^o$; c) $2\,\tilde{p}_s^o + \gamma a$ and d) $2\,\tilde{p}_s^o + \gamma a/2$.

The effect of the coefficient of earth pressure at rest, K_o, on the factor of safety is discussed next.

The analytical solution presented in Section 3 and Appendix A was shown to be a statically admissible solution satisfying continuity of radial and shear stresses across the integration circle boundary when the coefficient K_o associated with the *in-situ* stresses is equal to one (see Figure A-1). Numerical finite-difference (FLAC) models considering coefficients K_o different from one have been set up and computed to inspect the differences in (factor of safety) results with respect to the base case, $K_o = 1$.

With regard to equations (1) and (2) (see also equation 9) and in view that the ground is assumed to satisfy a Tresca shear failure criterion, considering an arbitrary point below the ground surface before the opening is made (e.g., point *S* in Figure B-8a), the scaled *in-situ* horizontal stress, σ_x^o, must lie in between the values $\tilde{\sigma}_{x\,\min}^o$ and $\tilde{\sigma}_{x\,\max}^o$ to avoid the ground being in plastic state prior to excavation.

In the analysis that follows, the ground is assumed not to reach the plastic state (i.e., to be in elastic state) prior to excavation above the level of the *invert* of the cavity (i.e., above the level of point *D*, at the ordinate $y = -a$, in Figure B-8a).

Considering that the scaled *in-situ* vertical stress, σ_y^o, is *lithostatic*, the minimum scaled *in-situ* horizontal stress, $\tilde{\sigma}_{x\,\min}^o$, is said to be associated with a minimum coefficient of earth pressure at rest, $K_o^{\min}$, i.e.,

$$\tilde{\sigma}_{x\,\min}^o = K_o^{\min}\,\tilde{\sigma}_y^o \tag{B-1}$$

In view of equations (3) and (4), and the fact that horizontal and vertical *in-situ* stresses are assumed to be principal stresses, the scaled stress $\tilde{\sigma}_{x\,\min}^o$ is also related to the scaled cohesion, $\tilde{c}$, as follows (see point F_A in Figure B-8b)

$$\tilde{\sigma}_{x\,\min}^o = \tilde{\sigma}_y^o - 2\,\tilde{c} \tag{B-2}$$

Equating the right-sides of equations (B-1) and (B-2), and replacing $\tilde{\sigma}_y^o$ by the left-side equation (9), considering also $y/a = -1$ (i.e., the ground above the elevation of point *D* in Figure B-8a being in elastic state), the minimum coefficient of earth pressure at rest, $K_o^{\min}$, results to be

$$K_o^{\min} = 1 - \frac{2\,\tilde{c}}{\tilde{q}_s + \xi + 1} \tag{B-3}$$

A similar analysis as above can be done with regard to the maximum coefficient of earth pressure at rest, $K_o^{\max}$. The maximum scaled *in-situ* horizontal stress, $\tilde{\sigma}_{x\,\max}^o$, is said to be associated with the coefficient $K_o^{\max}$ as follows

$$\tilde{\sigma}_{x\,\max}^o = K_o^{\max}\,\tilde{\sigma}_y^o \tag{B-4}$$

In view of equations (3) and (4), the scaled stress $\tilde{\sigma}_{x\,\max}^o$ is related to $\tilde{c}$ as follows (see point F_P in Figure B-8b)

$$\tilde{\sigma}_{x\,\max}^o = \tilde{\sigma}_y^o + 2\,\tilde{c} \tag{B-5}$$

Equating the right-sides of equations (B-4) and (B-5), and again replacing $\tilde{\sigma}_y^o$ by the left-side of equation (9) (considering $y/a = -1$), the maximum coefficient of earth pressure at rest, $K_o^{\max}$, results to be

$$K_o^{\max} = 1 + \frac{2\,\tilde{c}}{\tilde{q}_s + \xi + 1} \tag{B-6}$$

Figure B-9 shows the graphical representation of equations (B-3) and (B-6). In Figure B-9, the vertical axis represents the minimum or maximum values of coefficients of earth pressure at rest, $K_o^{\min}$ or $K_o^{\max}$, respectively, while the horizontal axis represents the scaled cohesion, $\tilde{c}$. In Figure B-9, the different sets of curves below and above the ordinate 1.0 correspond to limiting values of coefficents $K_o^{\min}$ and $K_o^{\max}$, respectively, computed with equations (B-3) and (B-6), respectively, to avoid the ground reaching the plastic state above the level of the *invert* before excavation. The symbols in the diagram in Figure B-9 represent the values of coefficients of earth pressure at rest, K_o, considered in the finite-difference (FLAC) models. The selected values of coefficients K_o cover the range 0 to 2 in increments of 0.5 and consider only cases for which the ground is initially in elastic state above the level of the *invert* of the opening.

Figure B-10 shows a similar diagram as in Figure 28, representing values of factor of safety as a function of scaled cohesion for cylindrical *contracting* cavities at scaled depths, $\xi = 2$ and 4, respectively. In Figure B-10, the continuous lines correspond to the analytical solution given by equation (21), while the symbols correspond

to the different cases of coefficients of earth pressure at rest, K_o, (i.e., represented as symbols in Figure B-9). Table B-3 summarizes the input parameters and results for the various numerical models. In Table B-3, the column labelled as *FS* lists the values of factor of safety obtained with the numerical models that consider a coefficient, $K_o = 1$, while the columns labelled as $FS_{Ko}^{(a)}$, $FS_{Ko}^{(b)}$, $FS_{Ko}^{(c)}$ and $FS_{Ko}^{(d)}$, correspond to factors of safety obtained with the numerical models that consider coefficients equal to 1.5, 0.5, 2, and 0, respectively. Inspection of the position (and superposition) of the various symbols in Figure B-10, and comparison of the values of factors of safety in the columns of Table B-3, reveal that the values of factor of safety obtained with the numerical models are the same for all considered values coefficients, K_o. This suggests that the proposed analytical solution that corresponds to a coefficient $K_o = 1$ may also be applicable to situations in which the coefficient K_o is different from one. For completeness, Figure B-11 shows the shape of plastic zones in the numerical finite-difference (FLAC) models for the first unstable situation for Case 2d in Table B-3, for values of coefficients K_o equal to 1, 0.5 and 1.5. Without considering the development of plastic failure for the ground below the *invert* of the cavities, the development of the plastic failure region at the sides and above the cavity for the case $K_o = 1$ results equivalent to that obtained for the cases $K_o = 0.5$ and 1.5.

A similar analysis of the effect of the coefficient K_o on the factor of safety was carried out for cylindrical *expanding* cavities. Figures B-12 and B-13 and Table B-4 are equivalent to Figures B-10 and B-11 and Table B-3, respectively, this time for the case *expanding* cavities. Similar observations about the resulting factors of safety in numerical models that consider values of coefficients K_o equal to one and different from one can be made from Figures B-12 and B-13 and Table B-4.

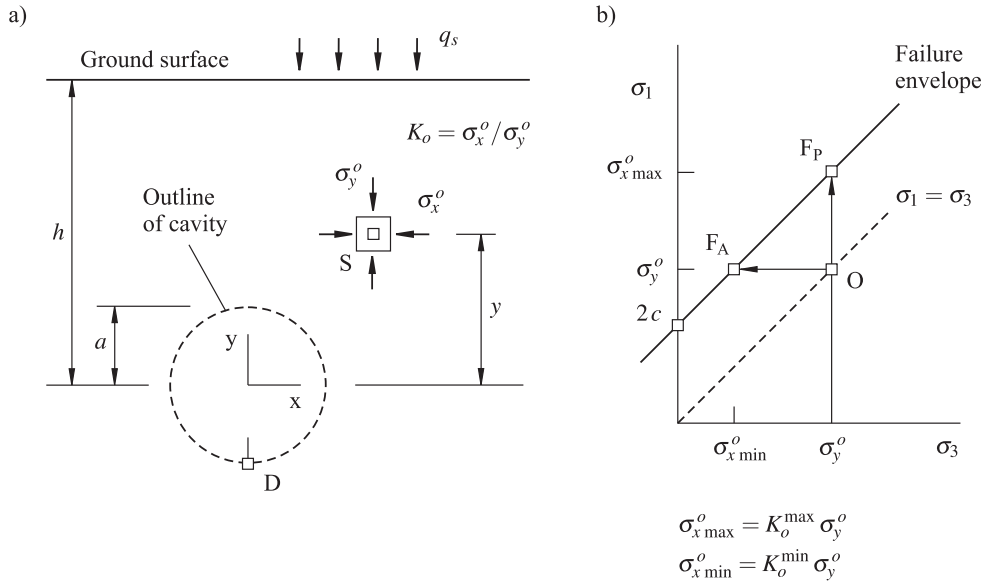

Figure B-8. Determination of the minimum and maximum values of coefficients of earth pressure at rest, K_o^{min} and K_o^{max}, respectively, compatible with an elastic *in-situ* stress field above an arbitrary depth, prior to excavation.

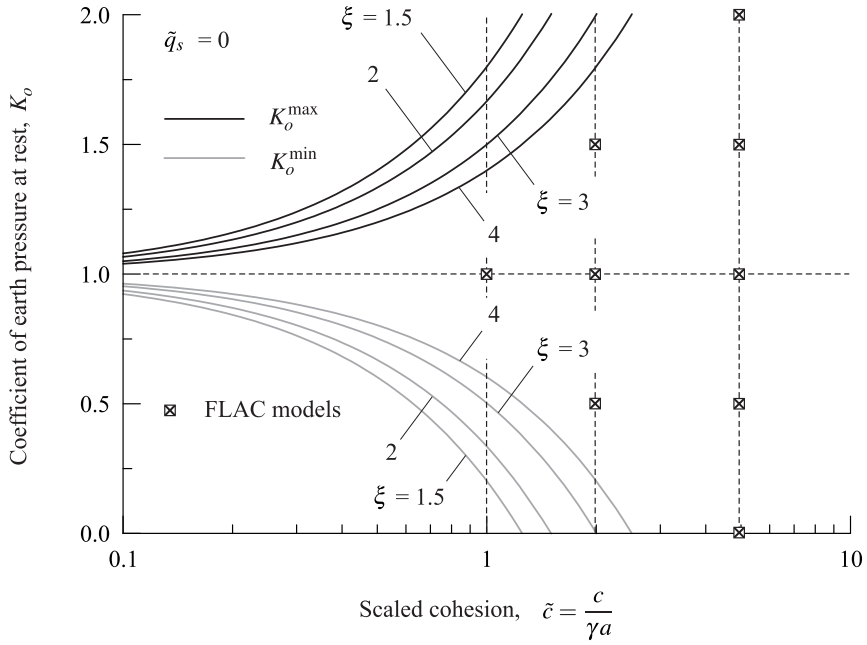

Figure B-9. Graphical representation of the relationship between the minimum and maximum values of coefficients of earth pressure at rest, K_o^{min} and K_o^{max}, respectively, as a function of scaled cohesion for zero scaled surcharge load on the ground surface. The symbols in the diagram represent the cases solved with the numerical (FLAC) models.

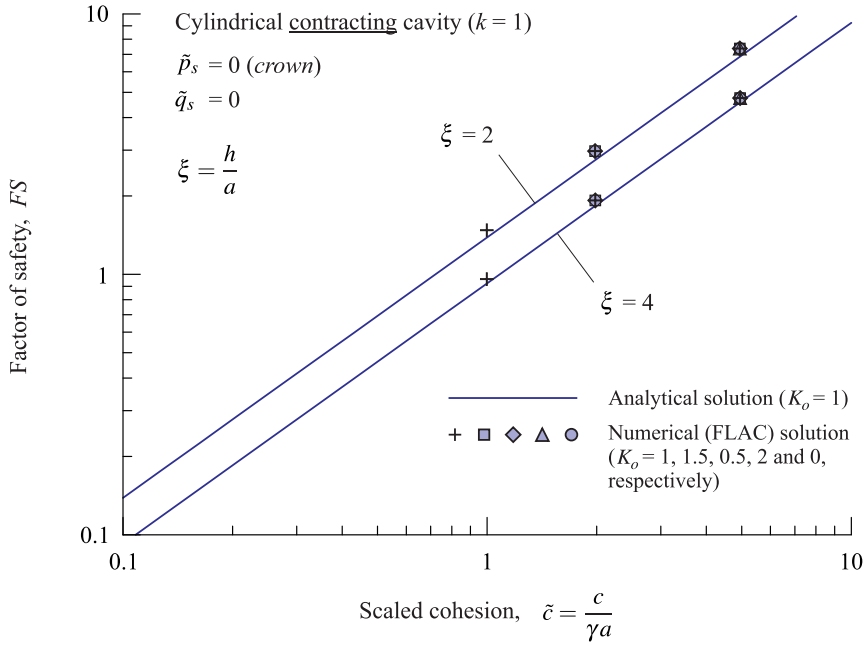

Figure B-10. Graphical representation similar to that in Figure 28, showing the relationship between factor of safety and scaled ground cohesion for cylindrical *contracting* cavities at the scaled depths, $\xi = 2$ and 4. The symbols in the diagram represent the factors of safety obtained with the numerical (FLAC) models for different values of coefficients of earth pressure at rest indicated in the vertical axis of Figure B-9.

Table B-3. Summary of input data and results for different cases of cylindrical *contracting* cavities and coefficients of earth pressure at rest solved with numerical (FLAC) models, represented in Figure B-10.

Case	ξ [-]	$\tilde{c}$ [-]	p_s [kPa]	FS [-]	$FS_{Ko}^{(a)}$ [-]	$FS_{Ko}^{(b)}$ [-]	$FS_{Ko}^{(c)}$ [-]	$FS_{Ko}^{(d)}$ [-]
2c	2.0	1.0	0.00	1.50	NA	NA	NA	NA
2d	2.0	2.0	0.00	3.00	3.00	3.00	NA	NA
2e	2.0	5.0	0.00	7.50	7.50	7.51	7.50	7.50
4c	4.0	1.0	0.00	0.97	NA	NA	NA	NA
4d	4.0	2.0	0.00	1.94	1.94	1.94	NA	NA
4e	4.0	5.0	0.00	4.84	4.84	4.84	4.84	4.84

The column labelled as *FS* lists the values of factor of safety for the case of hydrostatic in-situ stresses, $K_o = 1$ (this column is the same as the column labelled FS_N in Table 2). The columns labelled as $FS_{Ko(a)}$, $FS_{Ko(b)}$, $FS_{Ko(c)}$ and $FS_{Ko(d)}$ list the values of factor of safety for coefficients of earth pressure at rest, K_o, equal to a) 1.5; b) 0.5; c) 2; and d) 0, respectively.

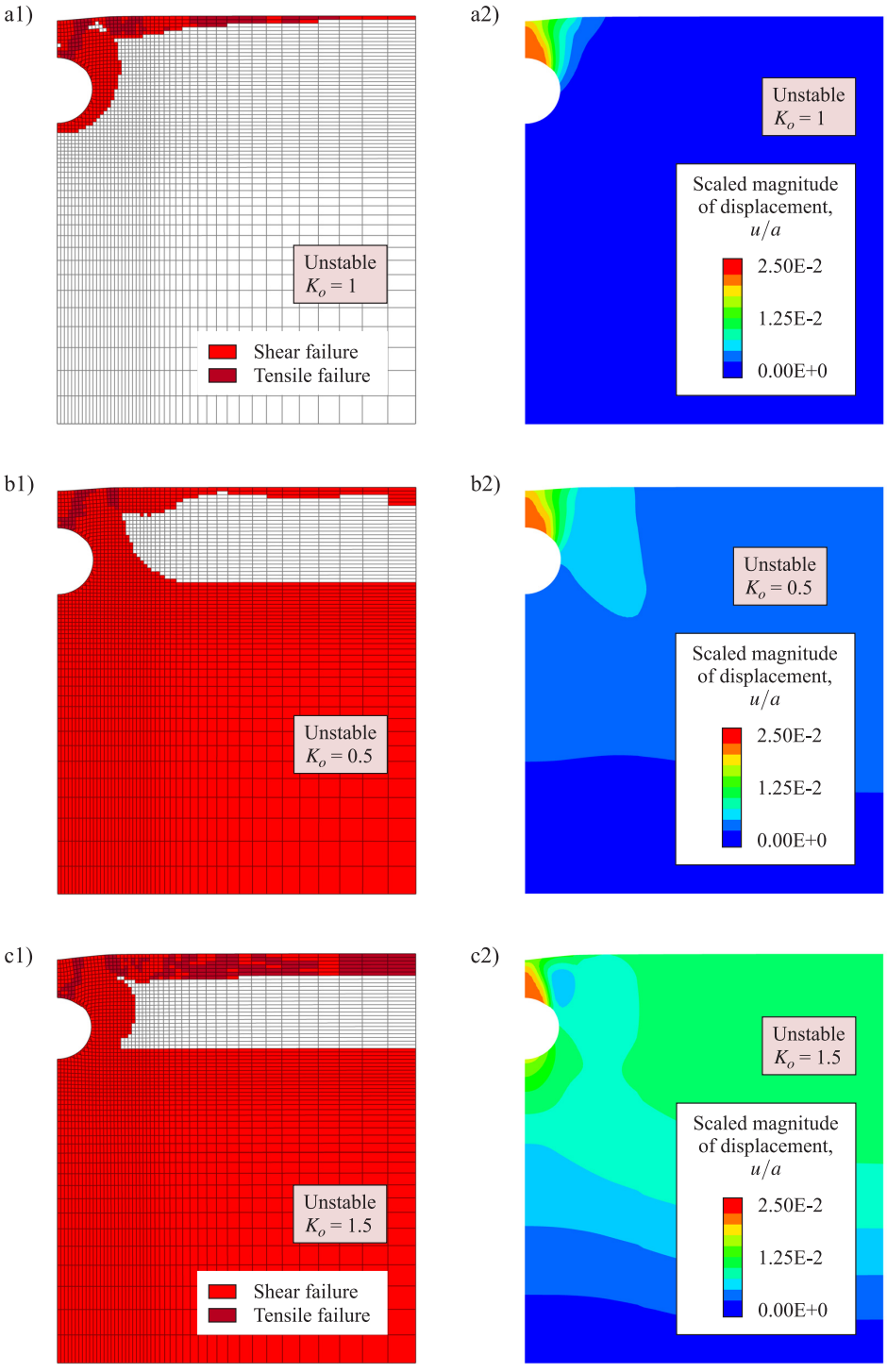

Figure B-11. First unstable situation in the computation of factor of safety with numerical (FLAC) models for cases of cylindrical *contracting* cavities with different values of coefficients of earth pressure at rest corresponding to Case 2d in Table B-3. The plots on the left side represent the elements that undergo plastic failure in tension or compression, while the plots on the right side represent the corresponding contours of magnitude of displacements. The three pairs of plots correspond to coefficients of earth pressure at rest, K_o, equal to a) 1.0; b) 0.5; and c) 1.5, respectively.

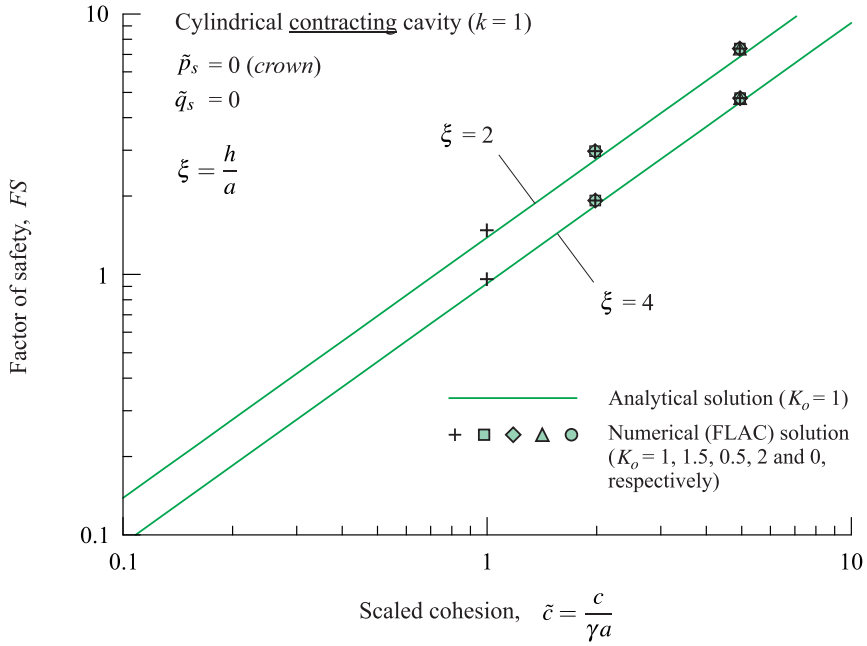

Figure B-12. Graphical representation similar to that in Figure B-10 for cylindrical *expanding* cavities.

Table B-4. Summary of input data and results for different cases of cylindrical *expanding* cavities and coefficients of earth pressure at rest solved with numerical (FLAC) models, represented in Figure B-12.

Case	ξ [-]	$\tilde{c}$ [-]	p_s [kPa]	FS [-]	$FS_{Ko}^{(a)}$ [-]	$FS_{Ko}^{(b)}$ [-]	$FS_{Ko}^{(c)}$ [-]	$FS_{Ko}^{(d)}$ [-]
2c	2.0	1.0	111.80	1.50	NA	NA	NA	NA
2d	2.0	2.0	145.60	3.01	3.01	3.01	NA	NA
2e	2.0	5.0	90.72	7.52	7.52	7.51	7.52	7.52
4c	4.0	1.0	168.00	0.97	NA	NA	NA	NA
4d	4.0	2.0	229.14	1.94	1.94	1.94	NA	NA
4e	4.0	5.0	628.86	4.85	4.85	4.85	4.85	4.85

The column labelled as FS lists the values of factor of safety for the case of hydrostatic in-situ stresses, $K_o = 1$ (this column is the same as the column labelled FS_N in Table 2). The columns labelled as $FS_{Ko(a)}$, $FS_{Ko(b)}$, $FS_{Ko(c)}$ and $FS_{Ko(d)}$ list the values of factor of safety for coefficients of earth pressure at rest, K_o, equal to a) 1.5; b) 0.5; c) 2; and d) 0, respectively.

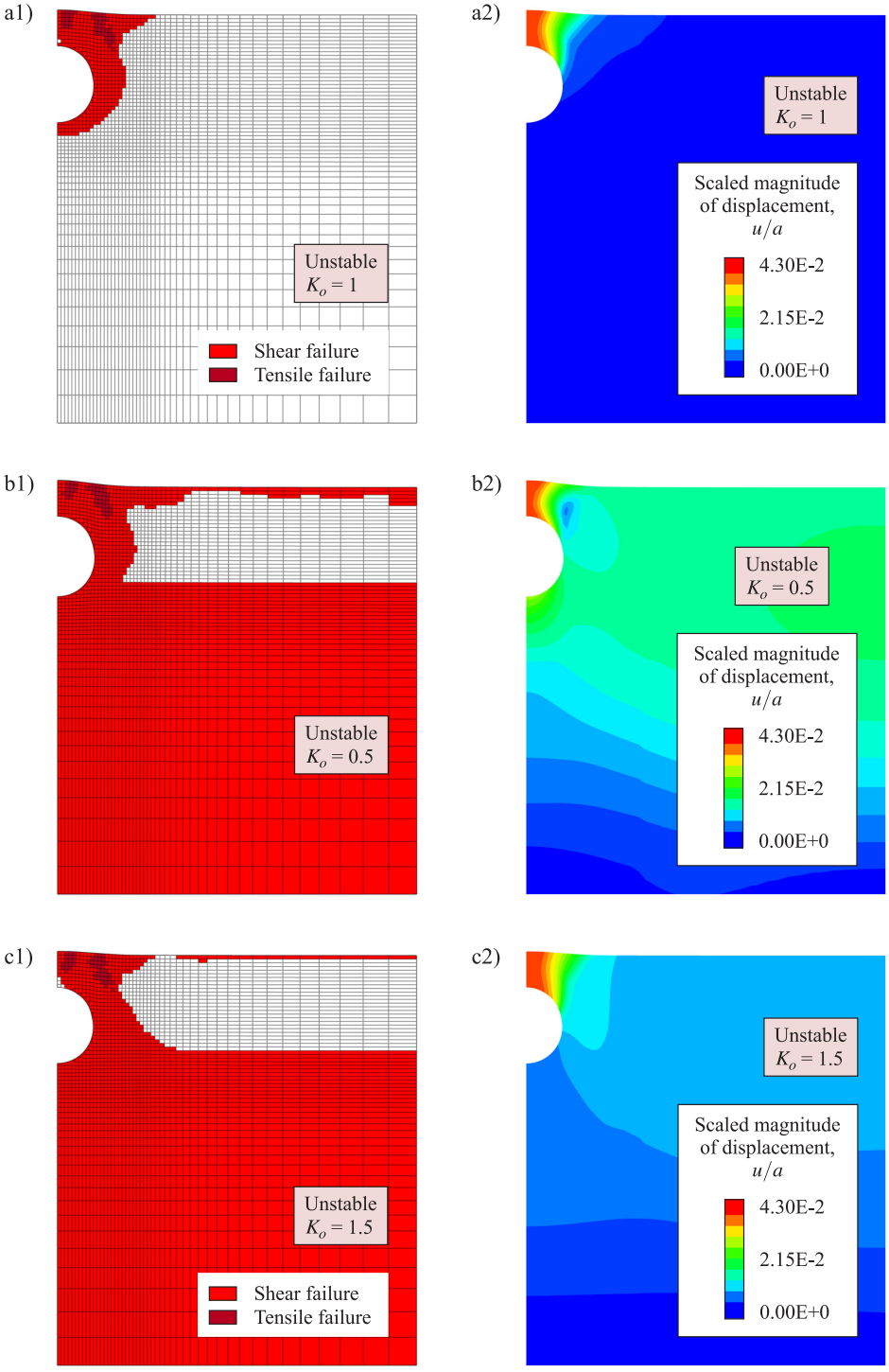

Figure B-13. Graphical representation similar to that in Figure B-11 for cylindrical *expanding* cavities, corresponding to Case 2d in Table B-4.

Appendix C. Derivation of Limit Equilibrium (Terzaghi) solution for contracting and expanding cavities in dry cohesive ground

This appendix presents the derivation of equations (32) and (38) in the main text. The derivation follows a similar analysis (including the use of the same notation) as in Terzaghi (1943) when describing arching effect in soils.

Figure C-1 shows the problem to be analyzed. A block (representing the ground above the opening) of height, D, and unit weight, γ, rests above the (assumed flat) roof of an opening of (in-plane) width $2B$. The flat roof of the opening in question is either the flat roof of long tunnel (of in-plane width $2B$ and unit length along the out-of-plane direction) or the flat roof of a square cavern (of width $2B$ in both in-plane and out-of-plane directions). The cases of long tunnel and square cavern are distinguished by introduction of the same parameter k used in the formulation in Appendix A.

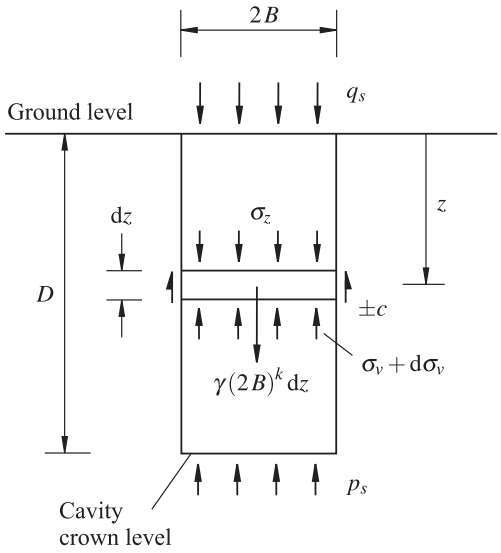

Figure C-1. Limit equilibrium analysis of a rectangular prismatic block representing the ground above the flat roof of a tunnel or square cavern —adapted from Terzaghi (1943).

A support pressure, p_s, is assumed to act at the base of the rectangular prismatic block in Figure C-1 (i.e., on the roof of the tunnel/cavern). A surcharge load, q_s, is assumed to act at the top of the block (i.e., on the ground surface). The rectangular prismatic block in Figure C-1 is assumed to be at the limit state of equilibrium. Therefore, full shear resistance is assumed to develop on the sides of the prismatic block. Considering the case of purely cohesive ground, the shear resistance is provided by the cohesion, c, of the ground. For the case of *contracting* openings, the shear resistance per unit area of prism side is represented by vectors, c, pointing upward, as indicated in Figure C-1. For the case of *expanding* openings, the shear resistance (per unit area of prism side) is represented by the same vectors, c, but pointing downward (note that in Figure C-1, the symbol $\pm$ is used as a prefix label of the cohesion vector to indicate either of the cases mentioned above).

Note that in this appendix, in contrast with the notation used in the equations in Section 5, the critical cohesion associated with the cavity in a critical state of equilibrium is denoted simply as c, rather than as c_{cr}.

Figure C-1 shows the free body diagram of a horizontal *slice* of block of differential height, dz, at a depth, z, below the ground surface. On the top surface of this (differential) slice, the acting force is the vertical stress, σ_v, multiplied by the slice area, $(2B)^k$, where $k = 1$ for the tunnel case, and $k = 2$ for the square cavern case. On the bottom surface of the (differential) slice, the acting force is the vertical stress, $\sigma_v + d\sigma_v$, multiplied by the same area. On the sides of the (differential) slice, the acting forces are $2c\,dz$ for the tunnel case, and $4(2B)c\,dz$ for the square cavern case. The weight of the (differential) slice is the unit weight, γ, of the slice multiplied by the volume of the slice, $(2B)^k\,dz$, again, with $k = 1$ for the tunnel case and $k = 2$ for the square cavern case.

Considering equilibrium of the acting forces for the horizontal slice in Figure C-1, the following total differen-

tial equation of the unknown function, σ_v, is obtained [3]

$$\frac{\mathrm{d}\sigma_v}{\mathrm{d}z} \pm k\frac{c}{B} - \gamma = 0 \tag{C-1}$$

Equation (C-1) can be integrated to obtain the solution for the function, σ_v, using the following boundary condition

$$\sigma_v = q_s \quad \text{at} \quad z = 0 \tag{C-2}$$

The integration and application of the boundary condition gives [4]

$$\sigma_v(z) = q_s + z\left(\gamma \mp k\frac{c}{B}\right) \tag{C-3}$$

The cavity roof pressure, p_s, required to maintain equilibrium of the prismatic block in Figure C-1 is found using the following condition

$$\sigma_v = p_s \quad \text{at} \quad z = D \tag{C-4}$$

Application of equation (C-4) in equation (C-3) gives (see footnote associated with equation C-3)

$$p_s = q_s + D\left(\gamma \mp k\frac{c}{B}\right) \tag{C-5}$$

Equation (C-5) allows definition of the equations for the required support pressure presented in the main text for the cases of *contracting* and *expanding* openings as follows.

For the case of *contracting* cavity, the limit equilibrium model by Terzaghi specifies that the required pressure on the flat roof of the opening is to be computed considering a prismatic block of width $2B_1$ (see Figure 5). This width is obtained by adding the width of the cavity, $2B_0$, and the top width of two *active* wedges developing on the sides of the opening (see Figure 5). For the case of purely cohesive ground, the top width of the two *active* wedges is two times the height of the opening, H (see Figure 5). Based on Terzaghi's specifications, Figure 33 shows how the limit equilibrium model by Terzaghi (Figure 5) applies to the case of *contracting* circular or spherical openings of radius, a, and depth, h, as considered in Section 3. In such case, the width, B, of the prismatic block in Figure C-1 becomes (see Figure 33)

$$B = B_1 = 3a \tag{C-6}$$

while the height, D, of the prismatic block in Figure C-1 becomes

$$D = h - a \tag{C-7}$$

Equation (32) in the main text is obtained by replacing equations (C-6) and (C-7) into equation (C-5) and applying the scaling rules introduced by equations (6) through (8); also, as explained earlier on, the critical cohesion in equation (C-5) is simply referred to as c rather than as c_{cr}.

Figure 35 shows how the limit equilibrium model proposed by Terzaghi (1943) (see Figure 5) applies to the case of circular or spherical *expanding* openings of radius, a, and depth, h, as considered in Section 3. For *expanding* cavities, the most conservative estimation of the maximum pressure, p_s, is obtained considering the smallest possible width of the prismatic block above the opening in Figure 7; this is in view that the self weight of the block contributes favorably to the stability, as it opposes the internal pressure. In such case, the width, B, of the prismatic block in Figure C-1 becomes

$$B = a \tag{C-8}$$

Equation (38) in the main text is obtained by replacing equations (C-7) and (C-8) into equation (C-5) and applying the scaling rules introduced by equations (6) through (8); also, as explained earlier on, the critical cohesion in equation (C-5) is simply referred to as c rather than as c_{cr}.

[3] The symbol $\pm$ in equation (C-1) is used to indicate that addition $(+)$ applies to *contracting* cavities and subtraction $(-)$ applies to *expanding* cavities.

[4] The symbol $\mp$ in equations (C-3) and (C-5) is used to indicate that subtraction $(-)$ applies to *contracting* openings and addition $(+)$ applies to *expanding* openings.

Appendix D. Derivation of analytical solution for contracting and expanding openings in cohesive-frictional ground

This appendix presents the derivation of the analytical solution for *contracting* and *expanding* cavities (equations 49 and 50, respectively), for the case of cohesive-frictional ground. The derivation of the solution is similar to the derivation provided for the case of purely cohesive ground in Appendix A.

To simplify the formulation, the derivation considers a transformation rule for stresses that applies to the Mohr-Coulomb shear failure criterion and which was used by several authors in the past (see, for example, Anagnostou & Kovari 1993; Carranza-Torres 2003). For a material that obeys the Mohr-Coulomb failure criterion given by equation (42), together with equations (43) and (44), the transformation rule consists in adding the term $c/\tan\phi$ to all stress variables. Denoting the transformed stresses with capital letters, the transformed major principal stress, S_1, and the transformed minor principal stress, S_3, are, respectively,

$$S_1 = \sigma_1 + \frac{c}{\tan\phi}; \qquad S_3 = \sigma_3 + \frac{c}{\tan\phi} \tag{D-1}$$

Considering the transformed principal stresses S_1 and S_3 given by equation (D-1), the Mohr-Coulomb failure criterion given by equation (42) becomes, after some algebra manipulation

$$S_1 = N_\phi S_3 \tag{D-2}$$

where N_ϕ is the passive reaction coefficient that is computed based on the internal friction angle, ϕ, using equation (43).

The same transformation rule is then applied to all stress quantities in Figure A-1. The transformed radial and hoop stresses, S_r and S_θ, respectively, at an arbitrary point P (see Figure A-1) are,

$$S_r = \sigma_r + \frac{c}{\tan\phi}; \qquad S_\theta = \sigma_\theta + \frac{c}{\tan\phi} \tag{D-3}$$

The transformed (*crown*) cavity pressure and the transformed ground surcharge load (see Figure A-1), P_s and Q_s, respectively, are,

$$P_s = p_s + \frac{c}{\tan\phi}; \qquad Q_s = q_s + \frac{c}{\tan\phi} \tag{D-4}$$

When expressed in terms of the transformed stresses, S_r and S_θ, the same equilibrium equations discussed in Appendix A (equations A-1 and A-2) are as follows.

For the radial direction

$$\frac{\partial S_r}{\partial \rho} + k\frac{S_r - S_\theta}{\rho} + \gamma a \sin\theta = 0 \tag{D-5}$$

and for the tangential direction

$$\frac{1}{\rho}\frac{\partial S_\theta}{\partial \theta} + \gamma a \cos\theta = 0 \tag{D-6}$$

As explained in Appendix A, the first step to derive the solution of the problem in Figure A-1 is to solve for the transformed stress quantities along the vertical segment defined by points A and B. The transformed stresses on this segment are denoted with the superscript 'AB'.

For the case of *contracting* cavities, as done in Appendix A, the assumption $S_\theta^{AB} = S_1$ and $S_r^{AB} = S_3$ is made (i.e., the material along segment AB is assumed to be in plastic state), so equation (D-2) is written as

$$S_\theta^{AB} = N_\phi S_r^{AB} \tag{D-7}$$

From equation (D-7), it also follows that

$$S_\theta^{AB} - N_\phi S_r^{AB} = 0 \tag{D-8}$$

Similarly, for the case of *expanding* cavities, the assumption $S_r^{AB} = S_1$ and $S_\theta^{AB} = S_3$ is made (i.e., again the material along segment AB is assumed to be in plastic state), so equation (D-2) is written as

$$S_\theta^{AB} = S_r^{AB}/N_\phi \tag{D-9}$$

From equation (D-9), it also follows that

$$S_\theta^{AB} - S_r^{AB}/N_\phi = 0 \tag{D-10}$$

Along the segment AB, the equilibrium equation for the radial direction is obtained from equation (D-5), making $\theta = \pi/2$, to yield the following total differential equation of the variable ρ,

$$\frac{\mathrm{d}S_r^{AB}}{\mathrm{d}\rho} + k\,\frac{S_r^{AB} - S_\theta^{AB}}{\rho} + \gamma a = 0 \tag{D-11}$$

Considering the relationships between transformed hoop and radial stresses given by equations (D-7) and (D-9) (for the case of *contracting* and *expanding* cavities, respectively), equation (D-11) can be integrated to obtain the unknown transformed radial stress function, $S_r^{AB}(\rho)$, using the following boundary condition

$$S_r^{AB} = Q_s \quad \text{at} \quad \rho = \xi \tag{D-12}$$

For the case of a *contracting* cavity, integration and application of the mentioned boundary condition give

$$S_r^{AB}(\rho) = Q_s \left(\frac{\xi}{\rho}\right)^{-k(N_\phi - 1)} + \frac{\gamma a \rho}{1 - k(N_\phi - 1)} \left[\left(\frac{\xi}{\rho}\right)^{1-k(N_\phi-1)} - 1\right] \tag{D-13}$$

and for the case of an *expanding* cavity

$$S_r^{AB}(\rho) = Q_s \left(\frac{\xi}{\rho}\right)^{k(N_\phi-1)/N_\phi} + \frac{\gamma a \rho}{1 + k(N_\phi - 1)/N_\phi} \left[\left(\frac{\xi}{\rho}\right)^{1+k(N_\phi-1)/N_\phi} - 1\right] \tag{D-14}$$

The transformed internal pressure at the *crown* of the cavity, P_s (see Figure A-1), can be found applying the following boundary condition to equations (D-13) and (D-14)

$$S_r^{AB} = P_s^A \quad \text{at} \quad \rho = 1 \tag{D-15}$$

for the case of a *contracting* cavity, this yields

$$P_s^A = Q_s\,\xi^{-k(N_\phi-1)} + \frac{\gamma a}{1 - k(N_\phi - 1)} \left[\xi^{1-k(N_\phi-1)} - 1\right] \tag{D-16}$$

and for the case of an *expanding* cavity,

$$P_s^A = Q_s\,\xi^{k(N_\phi-1)/N_\phi} + \frac{\gamma a}{1 + k(N_\phi - 1)/N_\phi} \left[\xi^{1+k(N_\phi-1)/N_\phi} - 1\right] \tag{D-17}$$

Note that equation (D-16) is the same equation (49) presented in the main text for the case of *contracting* cavities, while equation (D-17) is the same equation (50) presented in the main text for the case of *expanding* cavities.

As explained in Appendix A, the second and third steps to derive the solution of the problem in Figure A-1 involve integration of the equilibrium equations (in this case, equations D-5 and D-6) for the radial and tangential directions, respectively. The process of integration is identical to the one presented in Appendix A. To avoid repetition, only the final resulting expressions are presented below.

For both, *contracting* and *expanding* cavities, the solution of the transformed hoop stress, $S_\theta(\rho, \theta)$, in the integration circle is

$$S_\theta(\rho, \theta) = S_\theta^{AB}(\rho) + \gamma a \rho\,(1 - \sin\theta) \tag{D-18}$$

while the solution of the transformed radial stress, $S_r(\rho, \theta)$, is

$$S_r(\rho, \theta) = S_r^{AB}(\rho) + \gamma a \rho\,(1 - \sin\theta) \tag{D-19}$$

As done already in Appendix A, some observations about particular features of the solution presented above are highlighted next.

The first observation is about the distribution of internal pressure. The transformed internal pressure function,

$P_s(\theta)$, is obtained making $\rho = 1$ in equation (D-19). This gives

$$P_s(\theta) = P_s^A + \gamma a\,(1 - \sin\theta) \tag{D-20}$$

As with the case of cavities in purely cohesive ground, the cavity internal pressure increases with depth in a *lithostatic* manner, as if the internal pressure is provided by an imaginary pressurized gas which has the same unit weight as the ground surrounding the cavity. In particular, the transformed internal pressure at the *spring line* and *invert* levels of the cavity, are, respectively,

$$P_s^C = P_s^A + \gamma a; \qquad P_s^D = P_s^A + 2\,\gamma a \tag{D-21}$$

The second observation is about the stress state inside the integration circle in Figure A-1. To derive the solution of transformed stresses above, the assumption that stresses on the segment *AB* are compatible with a plastic state was made for both, cases of *contracting* and *expanding* cavities (see equations D-7 and D-9, respectively).
For the case of *contracting* cavities, using the solution for $S_\theta(\rho,\theta)$ given by equation (D-18) and the solution for $S_r(\rho,\theta)$ given by equation (D-19), the operation, $S_\theta - N_\phi S_r$ (as in equation D-8) results to be

$$S_\theta - N_\phi S_r = -\gamma a \rho\,(1 - \sin\theta)\left(N_\phi - 1\right) < 0 \quad \text{when} \quad \theta \neq \pi/2 \tag{D-22}$$

Equation (D-22) indicates that with the exception of the case $\theta = \pi/2$, the operation $S_\theta - N_\phi S_r$ is different from zero. In view of equation (D-8), the stresses throughout the full integration circle (with the exemption of the segment *AB*) are compatible with an elastic state (i.e., the ground is failing plastically only on the segment *AB*).
A similar analysis as above can be made for the case of *expanding* cavities. Using the solution for $S_\theta(\rho,\theta)$ given by equation (D-18) and the solution for $S_r(\rho,\theta)$ given by equation (D-19), the operation, $S_\theta - S_r/N_\phi$ (as in equation D-10) results to be

$$S_\theta - S_r/N_\phi = \gamma a \rho\,(1 - \sin\theta)\,\frac{N_\phi - 1}{N_\phi} > 0 \quad \text{when} \quad \theta \neq \pi/2 \tag{D-23}$$

Again, equation (D-23) indicates that with the exception of the case $\theta = \pi/2$, the operation $S_\theta - S_r/N_\phi$ is different from zero. In view of equation (D-10), the stresses throughout the full integration circle (with the exemption of the segment *AB*) are compatible with an elastic state (i.e., the ground is failing plastically only on the segment *AB*).
The third and last observation is about continuity of the stress field across the integration circle boundary (see Figure A-1). As discussed already in Appendix A, for the proposed analytical solution to be a statically admissible solution, continuity of radial and shear stresses must exist across the integration circle boundary. It was shown already that on the integration circle boundary, outside the integration circle, the initial stresses are compatible with stresses inside the integration circle only when the coefficient of earth pressure at rest, K_o, is considered to be equal to one. Only in this case the *insitu* shear stress, τ_s^o, becomes null. Also, when $K_o = 1$ the normal stress, σ_n^o, on the integration circle boundary, outside the integration circle, takes the following form (see equation A-29)

$$\sigma_n^o = q_s + \gamma a\,\xi\,(1 - \sin\theta) \tag{D-24}$$

On the integration circle boundary, inside the integration circle, the transformed radial stress can be computed by making $\rho = \xi$ in equation (D-19). This gives

$$S_r(\xi,\theta) = Q_s + \gamma a\,\xi\,(1 - \sin\theta) \tag{D-25}$$

Applying the inverse of the transformation in equation (D-3) to equation (D-25), the radial stress results,

$$\sigma_r(\xi,\theta) = q_s + \gamma a\,\xi\,(1 - \sin\theta) \tag{D-26}$$

Equation (D-26) being equal to equation (D-24) implies continuity of radial stresses across the integration circle boundary (when $K_o = 1$) and implies that the proposed solution for cohesive-frictional material is also a statically admissible solution when $K_o = 1$.